



HAL
open science

Brownian motion of colloidal particles located near different types of interfaces

Juan Carlos Benavides Parra

► **To cite this version:**

Juan Carlos Benavides Parra. Brownian motion of colloidal particles located near different types of interfaces. Physics [physics]. Le Mans Université; El Centro de Investigacion y de Estudios Avanzados del Insituto Politécnico National. Cinvestav (Méxique), 2017. English. NNT : 2017LEMA1011 . tel-03117554

HAL Id: tel-03117554

<https://theses.hal.science/tel-03117554>

Submitted on 21 Jan 2021

HAL is a multi-disciplinary open access archive for the deposit and dissemination of scientific research documents, whether they are published or not. The documents may come from teaching and research institutions in France or abroad, or from public or private research centers.

L'archive ouverte pluridisciplinaire **HAL**, est destinée au dépôt et à la diffusion de documents scientifiques de niveau recherche, publiés ou non, émanant des établissements d'enseignement et de recherche français ou étrangers, des laboratoires publics ou privés.

Thèse de Doctorat



*Cinvestav – IPN
Mexico D.F.*

Juan Carlos BENAVIDES PARRA

*Mémoire présenté en vue de l'obtention du
grade de Docteur de l'Université du Maine
sous le sceau de l'Université Bretagne Loire*

École doctorale: 3MPL

Discipline: Physique

Unité de recherche: IMMM-CNRS-UMR 6283, Le Mans, France

Soutenu le 17 mars 2017

Brownian motion of colloidal particles located near different types of interfaces

Directeurs de Thèse : **Guillaume BROTONS**, Maître de Conférences HDR, Institut des Matériaux et des Molécules du Mans, Le Mans
Mauricio Demetrio CARBAJAL TINOCO, Professeur, Cinvestav - IPN, Mexique

JURY

Rapporteurs: **Jean-Christophe GIMEL**, Charge de Recherche CNRS, Université d'Angers, Angers
Norma SÁNCHEZ SALAS, Professeur, Instituto Politécnico Nacional (IPN), Mexique

Examineurs : **Abdelhadi KASSIBA**, Professeur, Institut des Matériaux et des Molécules du Mans, Le Mans
Martín HERNÁNDEZ CONTRERAS, Professeur, Cinvestav - IPN, Mexique
Alfredo CRUZ OREA, Professeur, Cinvestav - IPN, Mexique

*This work is dedicated to my family,
your unconditional and permanent support always
gave me the necessary motivation to continue.
In memoriam of Ma. Inés and Isabel.*

Acknowledgments

I would like to express my special gratitude to Consejo Nacional de Ciencia y Tecnología (CONACyT) for the financial support. This not only includes the doctoral fellowship, but also the project grant, which facilitated provision of complete support for the performance of all experimental procedures. I am highly obliged towards Centre National de la Recherche Scientifique (CNRS) for the financial support provided to the Institut des Molécules et des Matériaux du Mans (IMMM). My special thanks to Cinvestav and Université du Maine, who under cotutelle agreement, imparted me the opportunity of completing my postgraduate studies. I would also like to thank my advisors Dr. Mauricio Carbajal (Cinvestav) and Dr. Guillaume Brotons (UM). They are just not teachers, they are also friends. Their intangible spirit and vision has inspired me to constantly work for a better purpose in my academic life.

Dr. Jose Méndez Alcaraz needs a special acknowledgement who instigated me to comprehend the subject through his fruitful discussions. I am highly indebted to Dr. Abdel Hadi Kassiba who motivated me to apply for the Cotutelle agreement. I would also express my appreciation to the members of my jury, Dr. Martín Hernández Contreras, Dr. Alfredo Cruz Orea, Dra. Norma Sánchez Salas, and Jean-Christophe Gimel for their precious time in evaluating my work.

My colleagues in the lab ensured that I was constantly engaged and entertained throughout my Phd tenure. In particular, I would give my whole-hearted thanks to my laboratory colleagues Dr. Brisa Arenas, Dr. Liliana Toscano, and MSc. Damian J. Méndez for their friendship. I can not conclude unless and until I thank all my close friends with whom, I enjoyed both academic as well as my personal life. I could learn from them the art of enjoying and living happily, even if you are stressed from all sides. It was really an unforgettable journey and a dream come true, with all those hard days and endless nights of work.

Abstract

We explore the Brownian motion of colloids near different types of interfaces (water-air, water-glass,...) using three dimensional digital video microscopy and reconstruction of single colloids trajectories in 3D over time. Satisfying agreements between data and published theoretical models were found for the simplest cases. In addition, we propose a theoretical approach able to transit from the free interface configuration (water-air) to the bound condition (water-glass). We also considered within this frame the situation where a solid interface was functionalized with a grafted short alkyl chain (flat and hydrophobic fixed wall) to compare with the same solid interface made hydrophilic from a UV-ozone plasma treatment that creates hydroxyl groups (Si-OH). From the stabilization of a phospholipid bilayer, we also studied the colloidal and hydrodynamic interactions with a soft (DOPC in L_α phase) or freezed (DMPC at L_β) biomimetic membrane covering the solid interface (SiO₂ glass).

Resumé

Le mouvement Brownien dans l'eau de colloïdes proches d'interfaces de différente nature (eau/air, eau/verre, ...) est étudié en utilisant une technique de microscopie numérique permettant de reconstruire les trajectoires individuelles en trois dimensions. Des accords satisfaisants entre les trajectoires et les modèles théoriques publiés ont été trouvés pour les cas les plus simples. En outre, nous proposons une approche théorique capable de passer de la configuration d'interface libre (type eau-air) à l'état lié (type liquide-solide). Nous avons également considéré dans ce cadre la situation dans laquelle une interface solide a été fonctionnalisée et rendue hydrophobe pour comparer le mouvement Brownien près de l'interface avec la même interface solide rendue très hydrophile par un traitement au plasma UV-ozone qui crée des groupes hydroxyle (Si-OH). Nous avons également étudié l'interaction colloïdale et hydrodynamique avec des interfaces recouvertes d'une membrane bio-mimétique phospholipidique molle (DOPC en phase fluide) ou gelée (DMPC en phase gel), toutes deux recouvrant le verre (SiO_2).

Resumen

Exploramos el movimiento browniano de partículas coloides cercanas a diferentes tipos de interfaz (agua-aire, agua-vidrio,...) usando la video microscopía digital tridimensional y la reconstrucción de sus trayectorias en tres dimensiones a lo largo del tiempo. Encontrando para los casos simples un buen acuerdo entre los datos experimentales y algunos modelos teóricos publicados. Además, proponemos una aproximación teórica que puede ser tabulada desde el caso de interfaz libre (agua-aire) al caso de un líquido en contacto con una frontera rígida (agua-vidrio). También, consideramos el caso de una frontera rígida funcionalizada con cadenas alquílicas cortas enganchadas a un sustrato (superficie plana hidrofóbica rígida) para ser comparada con el mismo tipo de interfaz hidrofílica obtenida por tratamiento de radiación UV de plasma de ozono el cual crea grupos hidroxilos sobre la superficie (Si-OH). De la estabilización de una bicapa de fosfolípidos, también estudiamos la interacción hidrodinámica de un coloide con una membrana biomimética suave (DOPC en fase L_α) o congelada (DMPC en fase L_β), en donde la membrana recubre una interfaz sólida (vidrio SiO_2).

Contents

Contents	ix
List of Figures	xi
1 Introduction	1
1.1 Scope of the thesis	1
1.1.1 Extending the study of solid supported membranes by using 3D-DVM	3
1.2 Brownian motion and soft matter	4
1.3 State of the art: study of colloids by using digital video microscopy	5
1.4 Methods to characterize a colloidal dispersion	6
1.4.1 Single particle tracking with microscopy	6
1.4.2 Use of optical tweezers	6
1.4.3 Low-coherence dynamic light scattering	7
1.4.4 Evanescent wave fluorescence microscopy	7
1.5 Different experimental approaches to our problem	8
1.5.1 Discussion of presented results from these authors	9
1.6 Outline of this work	11
2 Theoretical Considerations	13
2.1 Hydrodynamics	13
2.1.1 Navier-Stokes equations (NSE)	14
2.2 Colloidal Suspensions	16
2.2.1 Brownian motion	16
2.2.2 Einstein's argument	16
2.2.3 Langevin's equation	18
2.2.4 Particles sedimentation	19

2.2.5	The electric double layer	19
2.2.6	Colloidal dispersions used	21
2.3	Movement of a sphere approaching to a planar rigid wall or a planar free interface	22
2.3.1	Brenner solutions	23
2.3.2	Solutions for planar interfaces by Perkins and Jones	24
2.3.3	Solutions for a planar fluid-fluid interface	26
2.3.4	Proposed model	27
2.4	Optics in three-dimensional digital video microscopy (DVM-3D)	28
2.4.1	The point spread function	28
2.4.2	Analytical point spread function model for defocusing in oil-immersion microscopy	30
2.5	Description of phospholipid bilayer membranes	32
2.5.1	Hydrodynamics near a fluid membrane	33
2.5.2	Damping response of a bilayer stack	35
3	Experimental Procedures	39
3.1	Samples	39
3.1.1	Experiments on soft interfaces	39
3.1.2	Experiments on solid supported Membranes	43
3.2	Three Dimensional Digital Video Microscopy (3D-DVM)	45
3.3	Measurements at Cinvestav (Mexico)	48
3.3.1	Microscope	48
3.3.2	Calibration measurements	49
3.4	Measurements at the Université du Maine (France)	53
3.4.1	Microscope	53
3.4.2	Calibration set up	54
3.5	Particle detection method	56
3.5.1	Brief Matlab Graphical User Interface (GUI) Description	56
3.5.2	Image processing	60
4	Data Analysis	65
4.1	Brownian motion near a water-air interface	65
4.2	Brownian motion near a hydrophobic hard wall	70
4.3	Particle movement near solid supported membranes	70
	Conclusions	77

List of Figures

1.1	Difussion near a hard wall by 3D-DVM	3
1.2	Optical trapping	7
1.3	Total internal reflection fluorescence microscopy	8
1.4	Diffusiion near a water-air interface measured with different techniques	10
2.1	Velocity field near solid and free interface	14
2.2	Depicted Brownian motion	17
2.3	Electric double layer	20
2.4	Sphere close to a planar frontier	23
2.5	Sphere close to a fluid-fluid interface	26
2.6	Fraunhofer diffraction for a circular aperture	29
2.7	Optical path difference (design/out-of-design)	30
2.8	DOPC phospholipid and lamellar bilayer phases	32
2.9	Membrane fluctuations on a flat substrate	35
2.10	Damped fluctuations of a bilayer stack	36
2.11	Damping response for an embedded membrane	36
3.1	Water purification system	40
3.2	Sketch of cell and sample preparation (water-air)	42
3.3	Side view of the water-air sample cell	42
3.4	Spin-coating deposition method	43
3.5	Usual sample cell design	45
3.6	Side view of the sample cell for the solid supported membrane	45
3.7	Diffraction pattern for bright spots out of focus	47
3.8	Olympus BX60 microscope sketch	47
3.9	Calibration set up (Cinvestav)	49

3.10 Calibration process (Cinvestav)	50
3.11 Calibration results (Cinvestav)	52
3.12 Calibration test (Cinvestav)	53
3.13 Calibration results (UM)	54
3.14 Calibration test (UM)	55
3.15 Image processing main window	57
3.16 Window of the fitted diffraction pattern	58
3.17 Pattern tools window	59
3.18 Advanced settings window	59
3.19 Extracted images and weights partition	61
3.20 Individual image processing execution	62
4.1 Two particles near the free interface	65
4.2 MSD in parallel direction water-air interface	66
4.3 MSD in perpendicular direction water-air interface	66
4.4 Diffusion of colloids in perpendicular direction (water-air interface)	68
4.5 Diffusion of colloids in parallel direction (water-air interface)	69
4.6 Diffusion for spherical colloids close to a hydrophobic wall	71
4.7 MSD of a colloidal dispersion in water+PEG 3.6%	72
4.8 Trajectory of a sphere close to a DMPC membrane	73
4.9 Diffusion close to a DMPC membrane	74
4.10 Diffusion close to a DOPC membrane	74

1 Introduction

1.1 Scope of the thesis

Going through different products of our day to day we find inks, shampoos, lubricants, detergents, aerosols or instantaneous products for drinks. They have in common to be dispersion of composite materials, in which particles of one phase are embedded in another one. These composite materials could fit to different classifications depending on the aggregation state and the size of particles, or depending on their aggregation state and they could fall into another classification. Some usual examples of composite substances are smokes, gels, emulsions or suspensions. One of the goals to study such complex systems is to improve their industrial production that depends on the efficiency of some characterization as soft matter to enhance life quality throughout the improvement of emulsions that we consume every day. Fundamental understanding of the behavior of colloidal dispersions and how the minor components interact with each other, with the media or its boundaries are topics which are subjects of intense research. This is particularly important in the field of drug delivery carriers and understanding of the interaction between particles and biological boundaries under such as cell membranes made of a phospholipid bilayer.

In soft-matter research field, rheology is an interdisciplinary science that focus on the study of flows often with microstructures and dispersions, and there are many experimental ways to tackle such systems: using dynamical or static light scattering, using optical tweezers (to move particles in their medium), using evanescence wave particle tracking or using digital video microscopy to mention some.

In this work, we study the hydrodynamics of a quite rigid spherical particle immersed in a Newtonian fluid under low Reynolds number, where such particle

is subjected to creeping flows. Thereby, for these particles are sufficiently small to be classified as colloidal dispersions i.e, they are in a range size of around 10 nm up to about 10 μm , to be taken into account as colloidal dispersion. These peculiar systems experience Brownian motion for diffusive times in confined spaces.

Hereby, the hydrodynamic interactions (HI) are measured by means of three dimensional digital video microscopy (3D-DVM). We observe of a few Brownian spherical particles which go towards planar boundaries where these particles modify their Brownian motion due to the presence of the boundaries such as; a free interface, a hydrophobic wall or a deposited bio-membrane. For all these specific experiments, systems try to minimize the effect of electrostatic interactions or HI between colloids. We focus our attention to the study of a Brownian particle located nearby to a free planar interface. Therefore, under laboratory conditions the observations were conducted by tracking enough colloidal particles to properly sample the boundaries of interest.

Along the years spent to conclude this work one of the main pillars was to refine the 3D-DVM technique which support its functionality on a clear determination of light diffraction patterns recorded in digital images. Such patterns can provide information, about the three dimensional location of a fluorescent colloid. The position of a colloid on each time is obtained by means of appropriate algorithms that were refined along the work. Moreover, these algorithms were implemented in different experimental setups.

In 2007, Carbajal *et al.* [1] introduced this method to track, in three dimensions, a particle near a rigid wall using the glass slide bottom as reference, giving consistence measures of the diffusion coefficient as a function of the particle location over the rigid wall. These results are presented in Figure 1.1 showing an acceptable resolution along 15 μm of observation over the bottom. Moreover, they found an asymmetric behavior in the particle displacements for heights lower than a particle's diameter, whereby this asymmetry was reported by first time enhanced the observation capabilities of the 3D-DVM. The histogram plotted in Figure 1.1 clearly shows the asymmetry for the particle movement in the z direction representing that a particle can not find enough space to transit as it goes toward the wall, otherwise there is plenty space over that position.

An identical situation was experimentally studied in first place by MacKay *et al.* in 1962 [2], later some other authors found equivalent conclusions by following different ways [3–5]. This work is intended to extend the study of inhomogeneous systems by means of 3D-DVM.

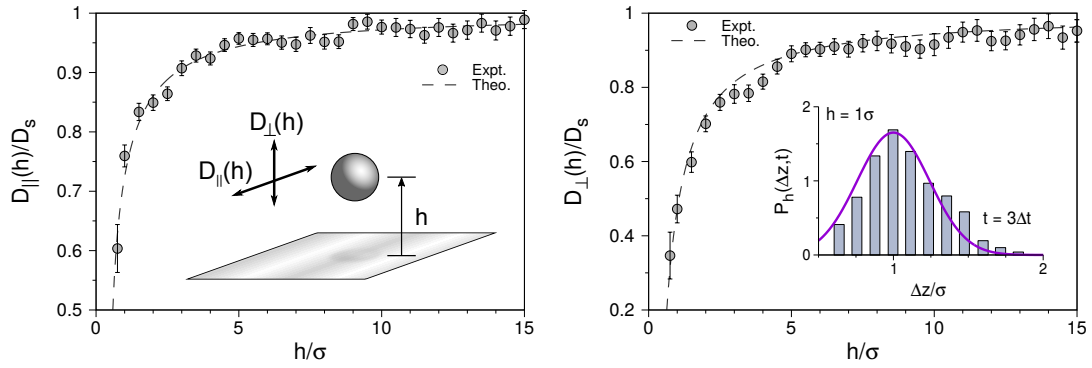


Figure 1.1. Colloidal dispersion of 1 μm spheres used to determine the diffusion coefficient upon the height over a flat rigid wall; its movement was split in the directions parallel and perpendicular with respect to the wall. The symbols represent the values obtained from the particle tracking by using 3D-DVM and the dashed line is the theoretical plot given in the perpendicular direction by the model of Brenner and the parallel direction through the model of Perkins and Jones. These plots are taken from Carbajal *et al.* [1].

1.1.1 Extending the study of solid supported membranes by using 3D-DVM

The study of membranes is a large research field in biophysics and soft matter. The understanding of the scale dependence of the effective surface tension, and, in particular, its value at short lengths scales, is an important topic for a large number of phenomena, like membrane adhesion, cell fusion, and other microscopic biological mechanism, such as endocytosis. Also, the interpretation of experiments on composite membranes, which is intended to determine the value of the bending rigidity κ , which is an important property to characterize a membrane. On the other hand, particles covered with a membrane are used in providing sterical stabilization for liposome drug carriers [6].

Such interactions between nano-sized particles and fluid membranes are ubiquitous in phenomena as antibiotic delivery, nano-particle toxicity or virus entry in cells. Brownian motion of small particles close to membranes is a new field to investigate, not just from the biophysical or biological point of view, beyond there are the pharmaceutical applications, or the cosmetic industry. Products intended to interact with any type of membrane required a good understanding of their reactions to a stimulation. For example a hydrodynamic perturbation produced from a particle movement, condition of particular interest for immunology science [7], membranes bending reaction for living cells [8], where it is crucial to quantify the cell reaction. In this sense, our method to observe Brownian mo-

tion close to a self-assembled membrane deposited on a substrate can give informations about particle interactions through the fluid disturbance over a organic system.

1.2 Brownian motion and soft matter

Around 30 years ago, the term *soft matter* was proposed by Pierre-Gilles de Gennes and Philip Pincus looking to gather in one definition the behavior of colloidal suspensions, surfactant solutions, polymeric systems, and liquid crystals. The main characteristic for this apparently broad amount of components whose the elements are larger than atoms and smaller than the bodies described by the classical physics. This kind of macromolecules can be subjected to move by thermal fluctuations rendering Brownian motion. In addition, they could exhibit a collective behavior and are subject to quite soft interactions that can be triggered with small changes in temperature.

Brownian motion was discovered by the botanist Robert Brown in 1827 from observations with a microscope of the movement of pollen grains on a liquid surface. Brown noticed that such particles followed random paths, without any clue of what could produce the movement. Much later Albert Einstein provided an explanation of the phenomenon by making use of the atomic hypothesis. Einstein assumed that the liquid is made of molecules that randomly move at high speed. He explained that the pollen grain receives unpredictable collisions throwing it in a random direction. Thus, the trajectory would depend on the collision frequency; and the molecules mean velocity and mass. Einstein predictions were confirmed by the physicist Jean-Baptiste Perrin in 1913, he was awarded with the Nobel prize in 1926.

Colloidal substances were initially named in 1861 by the British chemist Thomas Graham, from the word “kolla” which means glue in Greek. He used this term to identify a substance that got stuck on a stiff thin paper after the material was forced to cross the paper, the other tested substances like salty solutions had less resistance to cross the parchment. Graham label this two compounds as “colloids” and “crystalloids” respectively. Calling crystalloids the substance that are obtained from crystal minerals like salt [9]. Larger particles of range size between few nanometers to few microns subjected to thermal fluctuations were called *colloids*.

A polymeric material is composed of macromolecules. Where these elements are formed by chains of hundreds or thousands of sequentially connected identi-

cal monomer molecules. They are commonly present in synthetic materials such as plastics, rubbers films, and textiles. The essential bio-compounds of life, like proteins, are natural polymers, build from amino acids monomers (the genetic information is carried by a bio-polymer, the DNA [10]). It is important to mention that dynamics strongly depend on the time scale and temperature under consideration. Surfactants macromolecules are amphiphilic, with a hydrophilic part and a hydrophobic part, and they self-assemble when dissolved in water making micelles, with the hydrophobic part hidden from the water contact. They can organize in different shapes and phases like cylinders, spheres, or lamellae. Their size and shape depend on the structure and shape of surfactant molecules and on a subtle force balance between . We turn now our attention to colloidal systems diluted enough to have Brownian motion without particle-particle interaction.

1.3 State of the art: study of colloids by using digital video microscopy

Among the proposed stages in the study of soft condensed matter, one of them is the microfluidics along channels and particle diffusion through them. In such way, they give the option to explore applications for synthetic or living systems broadening knowledge at molecular scale, where the escape time is a crucial condition in biological pores or even in industrial applications. This kind of studies could be achieved in first approximation by using colloidal particles under digital microscopy observations. Whereby the boundaries play an important role along the process [11]. By using particle tracking it is also possible to measure microrheological properties in viscoelastic systems following the deviation of the particles motion from Brownian diffusion. This was exposed in the case of food polymers [12] for instance.

Recent studies of colloidal systems at short times and in confined space try to understand the HI of complex fluids [13]. Colloidal suspensions confined in microchannels are typical anisotropic diffusive systems with confining walls around the fluid [14]. Also, the research groups of soft matter are extending the application of the traditional techniques which can measure more properties of the colloidal suspensions [15]. Biophysical applications including lipid self-assembly of proteins and membranes, where the collective motion of micrometric particles adhered to a lipid vesicle is reported from particle tracking of the trajectories describing long range interactions [16]. In this sense, particle tracking of confined colloids with bio-compounds are an active field of research.

1.4 Methods to characterize a colloidal dispersion

This section introduces some classical techniques used to study colloidal suspensions. Such methods measure suspension properties to retrieve characteristics of the macroscopic system, like Brownian diffusion, interaction potentials and interparticle forces or system correlations...

1.4.1 Single particle tracking with microscopy

One way to perform a direct measurement of a particle diffusion is to track the movement of individual colloids. Here, a CCD camera coupled to a microscope records image sequences at fixed time intervals capturing the Brownian motion of the particles. Later, image sequences are processed by locating the particles' center to measure the distances traveled by them over each time interval. From the individual distances the mean square displacement would be plotted depending on the time, to directly obtain the diffusion coefficient. By using this principle there are some works worth to mention: by using digital video microscopy combined with optical tweezers Crocker and Grier [17, 18], studied hydrodynamic corrections the Brownian motion for two spheres in close proximity, or even the direct interactions for charged colloids, settling an experimental diffusion measured accuracy of $\pm 1\%$. Note that, from the particles' Brownian motion the Boltzmann's constant and the Avogadro's number are estimable [19, 20]. Another variation of the digital video microscopy to mention was presented by Park *et al.* The authors applied optical serial-sectioning microscopy (OSSM) to measure Brownian particle displacements in all three dimensions, deducing temperature information with uncertainty differentials of 5.54%, 4.26%, and 3.19% for the 1D, 2D, and 3D cases [21]. Inspired by the image processing method presented by Grier and Crocker, and the three dimensional tracking proposed by Park *et al.*, we have proposed the 3D-DVM [1, 22, 23].

1.4.2 Use of optical tweezers

Particles of size ranging from a few nanometers to tens of micrometers can be trapped and manipulated by a focused laser beam and combined with a microscope observation. This particular method of particles manipulation is called *optical tweezers*. Commonly the tracking is carried out capturing images to be further processed, nowadays as digitized data [24]. This technique was initially developed by Arthur Ashkin after he realized that a focused laser beam can pull

a micrometer body, as long as its refractive index would be higher than the surrounding media, confining the particle at the beam's center (Figure 1.2). He demonstrated that the particle is subjected to a balance between the radiation pressure and the external forces acting on the body [25].

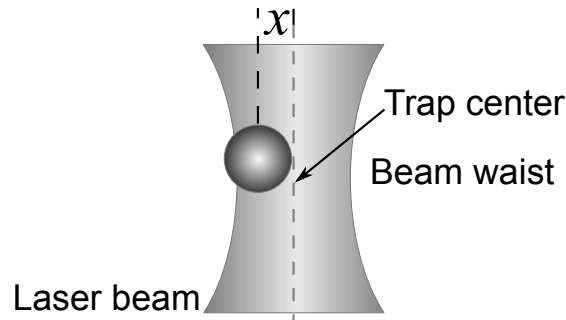


Figure 1.2. Optical trapping for dielectric objects at the light beam center, slightly above the beam waist.

In regard of the manipulation, it is mainly used to handle assembled molecular motors, to manipulate large proteins or lipid vesicles. Giving the chance to exert torques, stretching or bending on the material from movement of a colloid. This technique is also able to measure forces in systems with nanometric scales up to several micrometers, exerting forces of the order of hundreds of pN with a sub-pN resolution. One of the benefits given by the optical tweezers is that it is possible to trap living cells while keeping them alive, allowing a noninvasive technique for manipulation in cell biology.

1.4.3 Low-coherence dynamic light scattering

The main idea of this technique is to measure the echo and time delay of backscattered light in the sample through the characterization of the interference intensity obtained when the light coming from the sample and the light reflected in a reference surface overlap. When a low coherence source is used, the interference signal is temporally and spatially localized, so it is possible to use this phenomena to obtain distance values or parameters related to the time of flight of the light, reflected in different sections of a sample [26, 27].

1.4.4 Evanescent wave fluorescence microscopy

Also, known as Total Internal Reflection Fluorescence Microscopy (TIRM, TIRFM), it is defined when a light wave in a dielectric medium of index n_1 reaches an interface of a different dielectric material of a lower optical density, n_2 at angle θ_1

greater than the critical angle, $\theta_c = \sin^{-1}(n_1/n_2)$, so that total internal reflection (TIR) occurs. Although, all of the incident energy is reflected, an electromagnetic field with exponentially decreasing intensity propagates in the less dense medium. This field is known as an evanescent wave and has a decay length (penetration depth), d , on the order of the wavelength of the incident light, λ_0 .

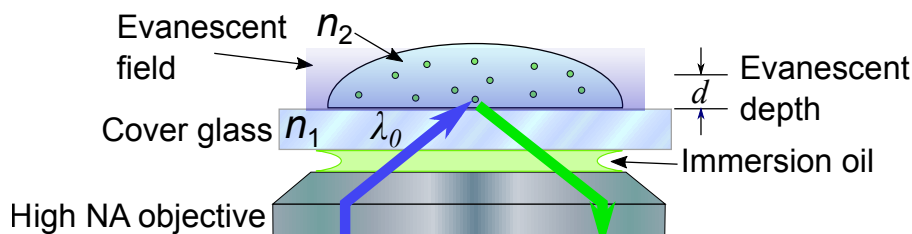


Figure 1.3. A laser beam of wavelength λ_0 is aimed to the sample crossing a cover slip with greater refractive index than the specimen media. The fluorescent response is imaged by a CCD camera.

The confined nature of the evanescent wave close to the interface is ideal for studying by fluorescence microscopy surfaces and near-surfaces phenomena pertaining to fluid mechanics and mass transport typically. Usually fluorescent markers used can be excited at the evanescent field zone giving a fluorescence response. Due to the limited evanescent field it is difficult to overcome the background noise, a common problem for fluorescent microscopy [28–31]. The TIRFM technique allows three dimensional tracking of nanoparticles in the sub-micrometer region from a solid surface so that experimental determination of the normal and lateral component of the Brownian diffusivity can be measured near a wall [5].

1.5 Different experimental approaches to our problem

This section presents experimental approaches using different ways to measure Brownian motion. The methods concerned are the optical tweezers and low-coherence dynamic light scattering used to describe a spherical colloid diffusing near a water-air interface, both cases present consistent results with the theoretical analysis. In first place the main experimental details will be presented and then interpretation of results.

The first set of experiments were performed by Wang *et al.* in 2009 [32]. They used optical tweezers to confine spherical particles of silica at a trapping spot,

later these spheres of $5.4 \mu\text{m}$ in diameter were moved to distinct interfaces. The free interface was obtained in a container of purified water leaving the upper side open to air, and that surface was covered with a very thin layer of oil, in order to prevent evaporation, then the sample was sealed. They accurately controlled the distance from the trapping spot to the interface using a piezo control attached to the objective thread, moving the particles confined in the beam spot towards the interface. Simultaneously, image sequences were recorded at each step collecting the parallel particle positions. Parallel diffusion was determined close to the interface as a function of the distance from the particle's center to the interface, and then compared with an approximate theoretical model. Nevertheless, another recent approach to the parallel diffusion was made by Boatwright *et al.* in 2014 [33].

The second set of experiments were made by Watari and Iwai [27, 34] were performed using the method of the spectral-domain low-coherence dynamic light scattering (LC-DLS) at the proximity of a liquid-air interface following the hydrodynamic changes in the z direction in regard of the hydrodynamic resistance. The set up was calibrated for identifying the interface location by using as reference a reflection peak produced by the mentioned interface. Samples were prepared with polystyrene spheres of radii 0.23 and $0.40 \mu\text{m}$ for separated observations. In order to retrieve the diffusion coefficients of this diluted system at different distances d moving the reference mirror in a stepwise manner to change the reference optical path. Thus, the normalized amplitude autocorrelation function was measured to further determinate the particles diffusion. The authors did not give many details about the sample container which is assumed to be opened to air.

1.5.1 Discussion of presented results from these authors

Top data in Figure 1.4 correspond to parallel diffusion of a spherical particle near a flat liquid-gas interface, scattered diamonds correspond to the diffusion values obtained by Wang *et al.* (its scale is at the top in the dimensionless distance h/a). They argued that the trapped particle was moved to reach around $1/5$ of deformation at the interface which explains why they report information for values $h/a < 1$ where it is not expected in the theoretical assumptions. Furthermore, the theoretical comparison is taken with the first order model of H. Faxén [35]. The long dashed line corresponds to the left part of Eq. (1.1) where h is the distance from the interface to the particle's center and a the sphere's radius. At the right side of Eq. (1.1) we find the first order formulation gave by Lee *et al.* [36] where

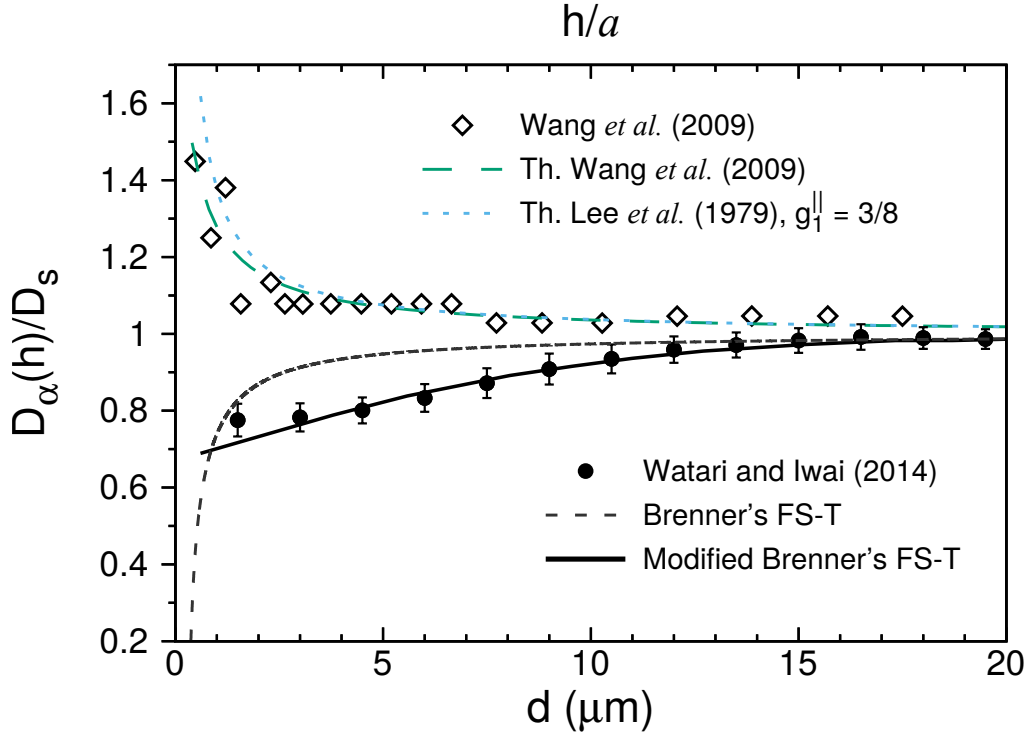


Figure 1.4. Diffusion near a gas-liquid interface upon the distance over the interface. Top data using optical tweezers. Down plot using LC-DLS.

in addition to the geometrical values, it takes into account dynamical properties of the immiscible fluids in contact namely,

$$\frac{D_{\parallel}(h)}{D_0} \approx 1 + \frac{3}{8} \left(\frac{a}{h} \right), \quad \frac{D_{\parallel}(h)}{D_0} = \left(1 - \frac{3}{16} \left(\frac{2\eta_1 - 3\eta_2}{\eta_1 + \eta_2} \right) \left(\frac{a}{h} \right) \right)^{-1}, \quad (1.1)$$

where $\eta_1 = 1$ cP corresponds to the water viscosity and $\eta_2 = 0.02$ cP is the air viscosity. Finally, the authors assumed that the Faxén approximation for a free interface is quite close to the first order fluid-fluid formulation from Lee *et al.* where the so called g_1^{\parallel} first coefficient of the formulation in Lee's is $g_1^{\parallel} = 0.36 \approx 3/8$.

On the other hand, at the down part in Figure 1.4, we plotted the experimental results obtained by Watari and Iwai depending on the distance d from the air-water interface to the particle's center. The data of the normalized autocorrelation function in the spectral domain was fitted using the formulation:

$$g^{(1)} = \exp(-D_{air} q^2 \tau), \quad (1.2)$$

where τ is the delay time, D_{air} the diffusion coefficient (keeping their notation), and is q the magnitude of the scattering vector. For diluted suspensions this

experiment is based on single scattering. Finally, the experimental data (black circles) are presented, so the theoretical expression gave by Brenner [37] (short dashed line), should be convoluted using the low-coherence function $\Gamma(z) = \exp[-4\ln(2)(z/l_c)^2]$, and l_c being the coherence length of the light source. Thus, the convolution is presented with the solid line, [38, 39]:

$$\left\langle \frac{D_{air}(d)}{D_0} \right\rangle = \frac{\int_0^\infty \left(\frac{D_{air}(d)}{D_0} \right) \Gamma(d-z) dz}{\int_0^\infty \Gamma(d-z) dz}. \quad (1.3)$$

The measured diffusion coefficient is in good agreement with the theoretical predictions from Brenner in the perpendicular direction for the free interface considering the spatial resolution of the experiment.

1.6 Outline of this work

In Chapter 2, we present an overview of the main theoretical aspects. In Chapter 3, we discuss the experimental protocols followed to prepare the samples used for the free interface and the solid supported membrane experiments, as well as the detailed explanation of the three dimensional digital video microscopy technique. Chapter 3 explores the physics that covers our experimental systems, like the hydrodynamics, the Brownian motion and the phospholipid membranes. In Chapter 4 we present the results obtained from each system.

2 Theoretical Considerations

In this chapter we present the main theoretical aspects of this work. In first place we introduce hydrodynamics and the Navier-Stokes equations for the Brownian motion of microspheres. Then, hydrodynamics for spherical bodies close to different types of planar boundaries and optics involved in the observation method are introduced. Finally, the last section discusses general aspects of the phospholipid membranes used.

2.1 Hydrodynamics

Colloidal particles studied in this work reside in a viscous fluid and their behavior is strongly influenced by hydrodynamic forces generated by the relative particle-fluid motion. The disturbance caused by a microsphere decays so slowly with distance and interparticle effects are seldom negligible in colloidal suspensions except if it is extremely diluted. For this presentation will not go deep into the full formulation relative to hydrodynamics, but rather mention some assumptions made to deal with the phenomena studied. Basic concepts related to colloidal hydrodynamics and known effects of geometric confinement will be introduced depending on the boundary conditions that an interface imposes to a complex fluid [40, 41].

The equations governing the behavior of the fluid take into account the relative importance of viscous and inertial effects. However, since for the system flows with low disturbances the inertial effects can be neglected and a particle is in viscous domain, considering the fluid motion as a Stokes flow. Fluids have particular forces that acts on surfaces, like the force experienced for the fluid in contact to an interface called *drag force*, this force acts in an opposite direction of the relative flow velocity, and depends on the surface area and smoothness. The

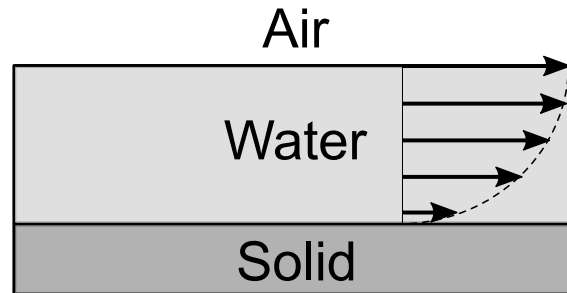


Figure 2.1. The velocity flow fields are different in the neighborhood of a fluid-fluid interface and a hard wall.

lift is the force component perpendicular to the flow direction, the pressure and the stress [42].

Confined fluids experience boundaries around, such as a solid wall or the interface with another fluid. The boundaries can be either of *stick* or *slip* nature, each situation described by the relative motion of the fluid in respect to the boundary. If the relative velocity at contact is zero, the condition is “stick”, otherwise is “slip”. For example, a Newtonian liquid which undergoes laminar flow nearby a solid planar surface is commonly assumed to have a sticky boundary condition, requiring the velocity of the liquid to match that of the solid surface (which increases the drag force). Thus, a simple velocity profile in a cross-section of a fluid flow on a plain solid wall shows velocity variations from a minimum value at the contact (solid-liquid) to a maximum flow away from the wall (Figure 2.1). On the other hand, for fluid-fluid interfaces as water-air, the maximum velocity profile reaches the free interface (Figure 2.1) [43]. Another fundamental boundary condition to consider between two fluids is the continuity of the shear stress at the interface.

2.1.1 Navier-Stokes equations (NSE)

The motion of a continuous media is studied through the Navier-Stokes equation solution. Knowledge of the velocity vector field is nearly equivalent to solving a fluid-flow problem. In the frame of continuous media, the NSE are linear partial derivate equations that describe the movement of particles of a Newtonian fluid perfectly incompressible but viscous. In first place, the statement of mass conservation, and the condition which dictates the incompressible fluid concerned at the constant density ρ in the *continuity equation*, Eq. (2.1) also called the in-

compressibility equation:

$$\frac{\partial \rho}{\partial t} + \nabla \cdot (\rho \mathbf{v}) = 0 \longrightarrow \nabla \cdot \mathbf{v} = 0. \quad (2.1)$$

Then, the momentum rate creation for a constant density ρ , which comes from the fluid flux $D(\rho \mathbf{v})/Dt$ that must be balanced with the sum of the forces exerted on a fluid volume (the external forces are divided in gravitational and contact forces) where \mathbf{v} is the local velocity vector of the fluid flow field. The contact forces over a volume depends on the stress tensor with components along the surfaces, the *strain rate* (involving the *shear viscosity*) and normal to the surface, the *pressure*. Introducing the Navier-Stokes equation

$$\rho \left(\frac{\partial \mathbf{v}}{\partial t} + (\mathbf{v} \cdot \nabla) \mathbf{v} \right) = -\nabla p + \eta \nabla^2 \mathbf{v} + \mathbf{F}(\mathbf{r}), \quad (2.2)$$

absorbing the gravity effect into a single dynamic pressure, p , and the constant shear viscosity of the fluid, η , that outcomes from the stress tensor for a Newtonian fluid. The equation of motion Eq. (2.2) contains on the right hand side the pressure force plus the viscous force and the density force applied by the particle on the fluid $\mathbf{F}(\mathbf{r})$. Which equals to the inertia force at the left hand side, these forces together are in equilibrium.

In the study of the hydrodynamics there are some conditions that simplifies NSE, these conditions can be tested by the Reynolds number giving an idea of the complexity of the flows providing an estimation of the importance of non-viscous and viscous forces acting in the fluid. As this number is close to zero the disturbance in the flow is very small and the Eq. (2.2) could be simplified.

Let consider an incompressible fluid with characteristic values: the velocity U (*e.g.* the velocity of a body in the fluid), a length L like the distance to a boundary, the Reynolds number (RN) is defined as $Re \equiv \rho UL/\eta$. Then the Eq. (2.2) can be written in an adimensional from using $\bar{p} \equiv pL/\eta U$

$$Re \left(\frac{\partial \bar{\mathbf{v}}}{\partial \bar{t}} + \bar{\mathbf{v}} \cdot \bar{\nabla} \bar{\mathbf{v}} \right) = -\bar{\nabla} \bar{p} + \bar{\nabla}^2 \bar{\mathbf{v}} + \bar{\mathbf{F}}(\bar{\mathbf{r}}), \quad (2.3)$$

the dimensionless NSE with the RN in front of the equation, can be simplified as the $Re \rightarrow 0$ (for example: a particle of $1 \mu\text{m}$ at $v = 1 \text{ mm/s}$ gives $Re \sim 10^{-6}$), yielding to the simplified NSE only keeping the terms of the right side:

$$-\bar{\nabla} \bar{p} + \bar{\nabla}^2 \bar{\mathbf{v}} = -\bar{\mathbf{F}}(\bar{\mathbf{r}}), \quad \text{and} \quad \nabla \cdot \mathbf{v} = 0, \quad (2.4)$$

the Eq. (2.4) is so-called momentum conservation. In this equation the viscous

forces predominate over the inertial forces [40, 43–45].

Nevertheless, as in many fluids the viscosity η depends on the temperature and when appreciable temperature difference exist in the flow, viscosity would be function of the position, but in systems with controlled temperature the viscosity is taken as constant. The momentum and mass conservation provide equations for the determination of p and v as function of x , y , z and t . Thus, for an incompressible fluid the set of equations are sufficient providing the adequate boundary conditions and we obtained above the NSE in their linear form (quasi-static) with conditions.

2.2 Colloidal Suspensions

Normally it is difficult to give at a strict definition of a colloid and the term is sufficiently broad to cover all uses. Although, a colloidal suspension could be described as a microscopically heterogeneous system where one component has dimensions in between those of molecules (the solvent here, i.e. fluid) and those of macroscopic particles like sand grains [46].

2.2.1 Brownian motion

Small enough colloids in a fluid are subjected to random forces from the thermal motion of the surrounding fluid molecules undergo *Brownian motion* (Figure 2.2). Therefore, since such fluctuations make the particle successively changes its direction, then as a result, the moves of the particle are not correlated. In consequence for such a random walk, the average of the total displacement is always zero. Hereby, as the Brownian particles diffuse in the fluid, the expressions that can describe such diffusivity were set by the Langevin equation and Einstein's argument as describe below. The important quantity reached measures the Brownian motion in the form of the second moment of the position distribution and writes in the form of the diffusion coefficient D_0 [46].

2.2.2 Einstein's argument

Einstein in its celebrated communication of 1905 [47] drove his attention to explain Brownian motion diffusivity for microscopically bodies in liquid from the molecular-kinetic theory of heat. Assuming a diluted spherical particle suspension of radii a , the velocity imparts by a force over the particle could be written as $v = F(\mathbf{r})/6\pi\eta a$, where that force is balanced with the drag force from

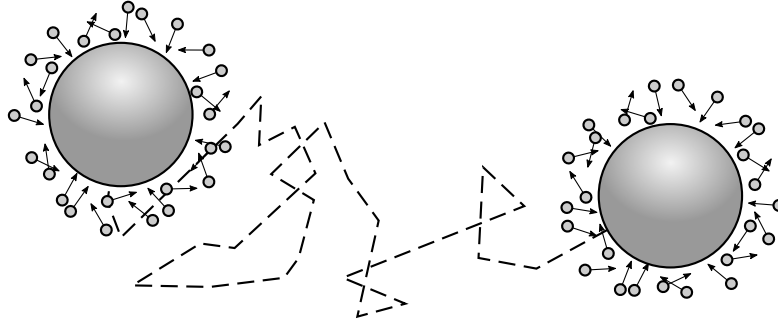


Figure 2.2. Sphere exhibiting Brownian motion due to collisions with the molecules surround it.

the contact with the liquid of dynamic viscosity η . The particle flux becomes: $J = c(\mathbf{r})\mathbf{F}(\mathbf{r})/6\pi\eta a$, for a particle concentration $c(\mathbf{r})$ [48].

Since the force comes from a potential energy $V(\mathbf{r})$, and the particle concentration follows the Maxwell-Boltzmann distribution for non-interacting particles in an environment at thermal energy kT ,

$$c(\mathbf{r}) = c_0 \exp\left(\frac{-E}{kT}\right) = c_0 \exp\left(\frac{-V(\mathbf{r})}{kT}\right) \quad \longrightarrow \quad \nabla c(\mathbf{r}) = -\frac{c(\mathbf{r})}{kT} \nabla V(\mathbf{r}) \quad (2.5)$$

then the diffusive flux $-D_0 \nabla c$ balances the particle concentration flux, and replacing the right part of Eq. (2.5) we obtain:

$$D_0 \nabla c(\mathbf{r}) = -\frac{c(\mathbf{r}) \nabla V(\mathbf{r})}{6\pi\eta a} = \frac{kT}{6\pi\eta a} \nabla c(\mathbf{r}). \quad (2.6)$$

From this simplified interpretation of the Einstein's description we obtain the Stokes-Einstein equation. The delivered energy from thermal molecular fluctuations equals the dissipated energy from the friction force. For a sphere the Stokes-Einstein equation is:

$$D_0 = \frac{kT}{\xi_0} = \frac{kT}{6\pi\eta a}, \quad (2.7)$$

with the particles difusivity D_0 in the liquid. Here ξ_0 (in kg/s) the particle drag coefficient, the inverse of the mobility μ_0 .

Besides, the Gaussian distribution of displacements from the initial position $x_{\alpha 0}$, it is possible to obtain through the diffusion equation postulated by Einstein, the displacements of Brownian particles in the diffusion process:

$$P(x_\alpha, t) = \frac{1}{\sqrt{4\pi D_0 t}} \exp\left(-\frac{(x_\alpha - x_{\alpha 0})^2}{4D_0 t}\right), \quad \text{for } t \gg \tau_v, \quad (2.8)$$

along of the directions x_α ($\alpha = 1, 2, 3$). These expressions have time scales of validity ranges. The pseudo-steady form for the viscous drag requires that the vorticity of the fluid diffuses faster than the particle loses inertia. Such time scale comes from the inertia relaxation time $\tau_v \approx \rho a^2 / \eta$ (presented in next section) [45].

2.2.3 Langevin's equation

Following the Newton's law of motion, the particle inertia and the viscous drag must balance the fluctuating Brownian force $F(t)$ which varies extremely rapidly compared to the variation in the particle velocity so-called Gaussian white noise. Let $x(t)$ the x -coordinate position of a microscopic sphere at any time t , or equivalent the velocity $\dot{x} = v(t)$,

$$m \frac{dv}{dt} = -\xi_0 v(t) + F(t), \quad (2.9)$$

where the drag force constant and positive coefficient is $\xi_0 = 6\pi\eta a$ (for a sphere). To understand the equation we consider the case of a free particle, the velocity will be obtained by simple integration leading to $v(t) = v_0 \exp(-t/\tau_v)$, which says that the particle will be at rest at long times. However, the quantity which tells us the time scale over which friction reduces to zero from the inertia effects [10] is *inertia-relaxation time* and the distance traveled in that time is:

$$\tau_v = \frac{m}{6\pi\eta a} = \frac{2a^2\rho}{9\eta}, \quad \Delta x = \tau_v \sqrt{\frac{kT}{m}} \quad (2.10)$$

where the mass was replaced in terms of the body density ρ .

The Langevin's equation, Eq. (2.9) is completely defined by the stochastic force $F(r)$. The mean value of random force is zero ($\langle F(t) \rangle = 0$). Since the random force arises from the molecular collisions over the particle, it is reasonable to consider that the correlation of the random forces decay extremely fast in consequence the time correlation order is about the molecular collision time, and the time correlation function could be taken as

$$\langle F(t_1)F(t_2) \rangle = 2\xi_0 kT \delta(t_2 - t_1), \quad (2.11)$$

this equation suggests that the fluctuations of the forces exerted on the particle by the fluid are related by ξ_0 , whereas such quantity overcomes directly from the dissipative nature of the drag force on the particle. The existence of this relation is generally called the fluctuation-dissipation relation. However, it is necessary to make further assumptions, the random force is the sum of the forces exerted

by many molecules over the body and its distribution is expected to be Gaussian. Therefore, $F(t)$ is a Gaussian random variable with mean value zero, and the variance through Eq. (2.11) defines the Langevin's equation [10].

It is also possible to deduce the one-dimensional mean square displacement (MSD) at time t :

$$\text{MSD} \equiv W(t) = \frac{\langle x^2(t) \rangle}{2} = D_0 t, \quad \text{for} \quad t \gg \tau_v, \quad (2.12)$$

the time assumption $t \gg \tau_v$ is usually satisfied in soft matter, where the velocity correlation time is very short in comparison with the time scale of other soft matter events [49]. The extension of the MSD depending on the dimension number ($n = 1, 2, 3$) would have the shape, $\langle r^2(t) \rangle = 2nD_0t$.

2.2.4 Particles sedimentation

Particle sedimentation comes from the density mismatch $\Delta\rho$ between the particles and the solvent. The ratio of gravity to the diffusive forces of a freely suspended sphere gives the effective sedimentation measured as a dimensionless Péclet number Pe

$$Pe = \frac{Lv_T}{D_s} = \frac{2\pi a^2 \Delta\rho g L}{9\eta D_s}, \quad (2.13)$$

where the system length L could be identified to a one characteristic dimension in a particular observation. The correction coefficient for the terminal velocity v_T for a sphere of radii a in a fluid of viscosity η and the self diffusion coefficient D_s , are also considered. A low Péclet number implies negligibly small gravitational sedimentation effects [31, 50].

2.2.5 The electric double layer

The stronger force for colloidal suspension interaction is from electrostatic origin. Despite the in common-origin, their manifestation differs. Among them are the *Van der Waals* force which is a global attractive force between a pair of molecules, or between surfaces. Here we restrict our attention to the *electric double layer* forces

Colloidal particles and particularly charged ones dispersed in a ionic solvent will attract counterions forming an ionic layer over their surface. This first layer of tightly bounded ions is called the *Stern layer* (Figure 2.3). Around the Stern

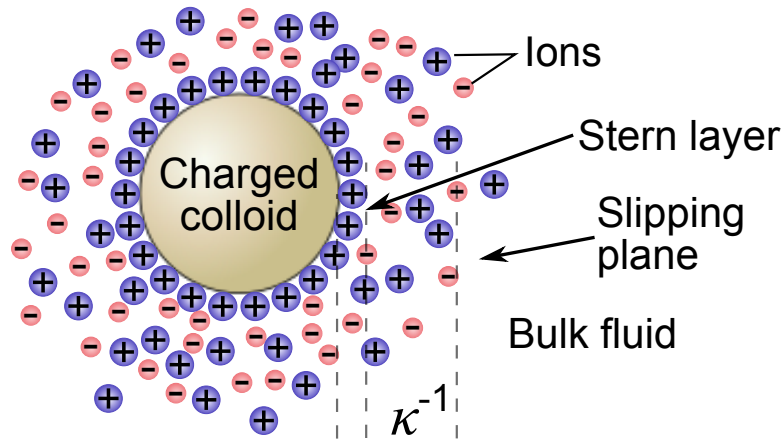


Figure 2.3. Electric double layer and the Debye length.

layer, ions tend to create a second layer called the *diffuse layer* limited by the so-called *slipping plane*.

By using the *Stern–Gouy–Chapman* theory in which the surface potential decreases within the double layer, then, electrostatic potential produced by the surface charged decay exponentially resulting in electrostatic screening effects that can reduce the interparticle Coulomb interaction. For diluted systems the screening effect reduces long range Coulomb interactions and a pair of colloids “can not see” each other far from few Debye length. On the other hand, when two macroions approach each other, overlap of their double layers causes a repulsive force which can stabilize the particles against aggregation [51].

The Debye length depends on the co-ions and counterions concentration in the solution understanding that they are distributed in the solvent at equilibrium, hence they obey the Boltzmann equilibrium distribution. Therefore, by using the electrostatic *Poisson* equation and the *Debye–Hückel* approximation, we obtained the Debye length:

$$r_0 \equiv \kappa^{-1} = \left(\frac{2e^2 n_0 z^2}{\epsilon \epsilon_0 k T} \right)^{-1/2}, \quad (2.14)$$

in conclusion for an electrolyte solution consisting of monovalent ions having charges ze and $-ze$, for a number density of ions in the solution n_0 , in a solvent of dielectric constant ϵ , at a temperature T , Eq. (2.14) gives the Debye length κ^{-1} .

The Coulombic potential of interaction between 2 pair charges (i and j) is in the Debye–Hückel theory (for spherical symmetry):

$$V_{ij}(r) = q_j \psi_i(r), \quad (2.15)$$

where the potential $\psi_i(r)$ (in V) induced by the charge $q_i = z_i e$ at distance r produces a potential energy $V_{ij}(r)$ (in J) on the charge $q_j = z_j e$. Where each charge is expressed depending on the elemental charge e , and considering the screened potential:

$$V_{ij}(r) = \frac{z_i z_j e^2}{4\pi\epsilon} \frac{\exp\left(-\frac{r}{r_0}\right)}{r}, \quad (2.16)$$

the Debye length r_0 is taken into account at the screening argument, and as a function of the ionic force $I = \frac{1}{2} \sum_m C_m^0 z_m^2$ and the density ρ , the Debye length (Eq. (2.14)):

$$r_0 = \sqrt{\frac{\epsilon RT}{2N_A^2 e^2 \rho I}}. \quad (2.17)$$

We see straightforward that for $r \ll r_0$: $r/r_0 \rightarrow 0$ and $\exp(r/r_0) \rightarrow 1$ so that the potential is unscreened. Otherwise, for $r \gg r_0$: the interaction potential decreases as $\exp(r/r_0) \rightarrow 0$.

Taking into account the radius of the i -particle, we obtain a correction and

$$\varphi_{i,R_i}^{r \gg R_i} = \frac{e}{kT} \psi_{i,R_i} = \left(z_i L_B \frac{1}{r} \exp\left(\frac{r}{r_0}\right) \right) \left(\frac{\exp\left(\frac{R_i}{r_0}\right)}{1 + \frac{R_i}{r_0}} \right), \quad (2.18)$$

her the first term is the potential with screening for a punctual charge, and the second factor is the correction term > 1 . Here the Bjerrum length corresponding to the distance where temperature forces (kT) are equal to 2 charge electrostatic interaction:

$$L_B = \frac{1}{kT} \frac{e^2}{4\pi\epsilon}. \quad (2.19)$$

We see that the screening potential reduces if one includes the particle radius R_i for a given amount of charges z_i .

2.2.6 Colloidal dispersions used

In our case we used a typical colloidal dispersion: spherical polystyrene particles of $1.0 \mu\text{m}$ of diameter with relative density $\rho_c/\rho_w = 1.05$, immersed in water of viscosity $\eta = 1.0 \text{ mPa}\cdot\text{s}$, at $20 \text{ }^\circ\text{C}$, with 10 mM of NaCl. Then the inertia relaxation time Eq. (2.10) is $\tau_v = 5.81 \times 10^{-8} \text{ s}$, which is a very short time so that the inertia dominates over the viscous forces. At longer times the velocities are not correlated and we consider a random walk (domain of the Brownian times). During the time τ_v the particle had a mean displacement of $\Delta\bar{x} = 1.58 \times 10^{-4} \mu\text{m}$ which is a small percentage of the particle diameter. The Péclet number gives

2.3. Movement of a sphere approaching to a planar rigid wall or a planar free interface

an estimation of the relevance of the gravitational effects over the colloids, if this number $Pe \ll 1$ the effects are negligible. By using the Eq. (2.13) $Pe = 0.063$ ensuring that for this system the gravitational force does not affect the suspension stability. Now considering the terminal velocity $v_T = 2\pi a^2 \Delta\rho g / 9\eta$, giving for this example $v_T = 2.71 \times 10^{-8}$ m/s.

The Reynolds number ($Re = \rho UL/\eta$) for the terminal velocity and the distance equivalent to the particle diameter gives $Re = 2.71 \times 10^{-8}$. This low number confirms small disturbances generated by the particle movement.

The last scale to mention is the Debye length, using in Eq. (2.14), the length for an ionic concentration of 10 mM is $\kappa^{-1} = 3.04$ nm, giving an appropriated electrostatic screening so that particles do not interact via electrostatic field when separated by distances larger than several diameters.

It is worth to notice two points: the force correlation time is even smaller than the inertia relaxation time, which is the time between molecular collision of the order $\sim 10^{-12}$ s, four orders less than τ_v . Our measurements are carried out with at maximum camera speed of 30 fps, or shoots in time lapses of $\Delta t = 33.33$ ms, then our technique clearly captures beyond the minimum time scale.

2.3 Movement of a sphere approaching to a planar rigid wall or a planar free interface

The solution to the Navier-Stokes equation for a creeping flow of an incompressible fluid when a particle goes in perpendicular direction to a planar rigid wall or free interface was developed by Brenner in 1961 [37]. The parallel displacement solution to this problem was obtained by Perkins and Jones 1991 [52] & 1992 [53] in two complementary letters. This approximation will be employed to compare the experimental data of the present work. Nevertheless, in the literature there are other publications concerning this case. First approximations for considering motion toward the perpendicular direction was made by Lorentz in 1907 [54], then Faxén presented its work for perpendicular direction to a hard wall and a free interface [35, 35]. In 1967 Goldman *et al.* presented a letter extending the study for the parallel component flow produced for a spherical body near a flat wall [55]. There are some other works of interest by O’Neil [56] and Bart [57] that, considered analytical solutions to the hard wall and fluid-fluid interface, respectively.

Next sections treat the case of spherical body of radii a at the distance h over the surface with stick boundary condition and without normal velocity at the sur-

2.3. Movement of a sphere approaching to a planar rigid wall or a planar free interface

face. The fluid is considered as incompressible with creeping flow and boundary conditions at the planar interface according to case (fluid-fluid, solid-fluid interface).

2.3.1 Brenner solutions

In its development, which is one of the most cited, a particle going to the planar interface is represented in bipolar coordinates, using axisymmetrical flows [58, 59]. Brenner considered a sphere falling with constant velocity U as it goes to the planar surface. The coordinate transformation is detailed by Happel and Brenner in [40]. Navier-Stokes equations are treated by means of stream functions, the main difference between both cases lay on the correct boundary conditions for each interface.

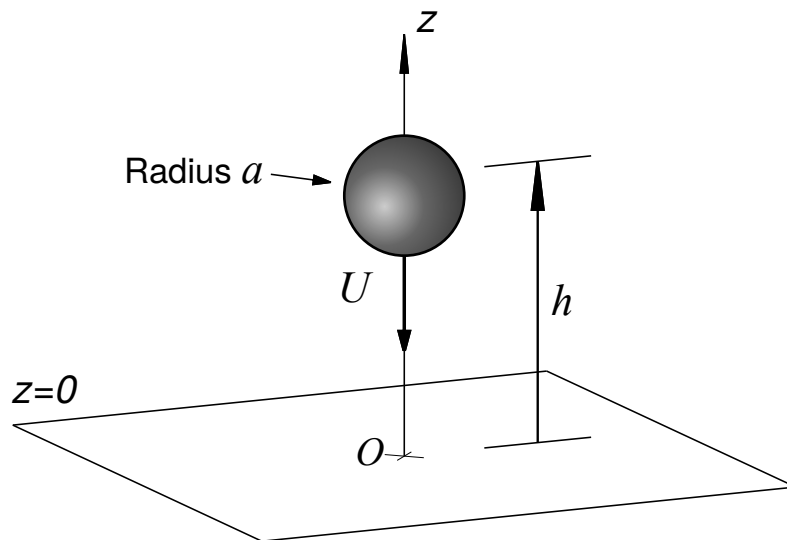


Figure 2.4. Spherical particle close to a planar frontier.

Rigid wall

The treatment of the Navier-Stokes was given by the coordinate change to bipolar coordinates, and considering the flow as axisymmetrical, in conjunction with the appropriate boundary conditions: no relative motion of the wall with the fluid in contact, for the rigid wall case, stick and zero velocity in normal direction conditions respect the sphere surface (Figure 2.4). By using the Stokes' stream

functions the translational friction component for the z directions is giving as

$$\frac{\xi_{\perp}^{BH}(h)}{\xi_0} = \frac{D_0}{D_{\perp}^{BH}(h)} = \frac{4}{3} \sinh \alpha \sum_{n=1}^{\infty} \frac{n(n+1)}{(2n-1)(2n+3)} \times \left[\frac{2 \sinh(2n+1)\alpha + (2n+1) \sinh 2\alpha}{4 \sinh^2(n+\frac{1}{2})\alpha - (2n+1)^2 \sinh^2 \alpha} - 1 \right], \quad (2.20)$$

where $\alpha = \cosh(h/a)$. This expression which is an analytical way to determine the normalized diffusion depending only on the geometric parameters a and h , so far the drag force increases as the particle tends to $z = 0$.

Free surface

While, for a free interface the stress parallel is gone due to the inexistent viscosity in the second media which is a free media [60]. Then the translational correction to the Stokes' law for perpendicular direction is giving by

$$\frac{\xi_{\perp}^{BF}(h)}{\xi_0} = \frac{D_0}{D_{\perp}^{BF}(h)} = \frac{4}{3} \sinh \alpha \sum_{n=1}^{\infty} \frac{n(n+1)}{(2n-1)(2n+3)} \times \left[\frac{4 \cosh^2(n+\frac{1}{2})\alpha + (2n+1)^2 \sinh^2 \alpha}{2 \sinh(2n+1)\alpha - (2n+1) \sinh 2\alpha} - 1 \right]. \quad (2.21)$$

Here also $\alpha = \cosh(h/a)$. In contrast, with the Eq. (2.20) for the free surface case the friction ratio decreases slower.

2.3.2 Solutions for planar interfaces by Perkins and Jones

Perkins and Jones presented two publications with the solutions for a solid sphere going in an arbitrary direction and spinning also around an arbitrary axis nearby either a planar free surface or a hard surface [52,53]. Their approach were mainly supported on the reflection method which offers a systematic way to achieve the mobility matrix (method detailed in [61,62]) For a hard sphere with stick boundary conditions under an induced force density $F(\mathbf{r})$, the fluid motion around is described by the NSE, [63–66],

$$\eta \nabla^2 \mathbf{v} - \nabla p = -F(\mathbf{r}), \quad \nabla \cdot \mathbf{v} = 0, \quad (2.22)$$

solving the Navier-Stokes equations by using a complete set of incident and outgoing waves terms of vector spherical harmonics for the velocity field $\mathbf{v}(\mathbf{r})$ and

2.3. Movement of a sphere approaching to a planar rigid wall or a planar free interface

the pressure p , and the shear viscosity η . By the complete definition of the force and using the Oseen's tensor [66, 67] they showed how to arrive at the friction matrix [68–70]. Such resistance matrix modifies the rigid motion of the sphere, written as

$$\begin{pmatrix} \mathcal{F} \\ \mathcal{T} \\ \mathcal{F}^{(2S)} \\ \vdots \end{pmatrix} = \begin{pmatrix} \xi^{tt} & \xi^{tr} & \xi^{td} & \dots \\ \xi^{rt} & \xi^{rr} & \xi^{rd} & \dots \\ \xi^{dt} & \xi^{dr} & \xi^{dd} & \dots \\ \vdots & \vdots & \vdots & \ddots \end{pmatrix} \begin{pmatrix} \mathbf{v}_0(\mathbf{R}_1) - \mathbf{U} \\ \boldsymbol{\omega}_0(\mathbf{R}_1) - \boldsymbol{\Omega} \\ \mathbf{g}_0(\mathbf{R}_1) \\ \vdots \end{pmatrix}, \quad (2.23)$$

where \mathcal{F} is the net force on the sphere, \mathcal{T} the torque on the rigid body, and $\mathcal{F}^{(2S)}$ the force dipole moment, here they are related to the incident flow \mathbf{v}_0 and its first derivatives evaluated at the sphere center.

Free surface

The authors presented the normalized friction coefficients in both parallel and perpendicular direction [52], comparing their results in the parallel direction with the publication of Goldman *et al.* [55], finding good agreement. These expressions depend on the geometrical properties of the system, the particle radius and the distance from the interface:

$$\frac{\xi_{\parallel}^{PF}(h)}{\xi_0} = 1 - 0.375\gamma + 0.140625\gamma^2 - 0.1152344\gamma^3 + 0.1135254\gamma^4 - 0.06893921\gamma^5 \dots, \quad (2.24)$$

where $\gamma = a/h$. The parallel friction component decreases as the sphere goes to the planar boundary. This because the viscosity of the free media is considered $\eta_e \rightarrow 0$. On the other hand, the perpendicular components for the translational friction matrix was compared with Brenner results Eq. (2.21), showing equivalent predictions:

$$\frac{\xi_{\perp}^{PF}(h)}{\xi_0} = 1 + 0.75\gamma + 0.5625\gamma^2 + 0.296875\gamma^3 + 0.3632813\gamma^4 + 0.3779297\gamma^5 + \dots \quad (2.25)$$

It is worth to notice that, these expressions do not have singularities for any value of $h \geq a$.

Hard wall

The hard wall assumption is reached for a planar boundary without deformation [53], where the friction coefficient of the parallel direction is given by the power

series:

$$\frac{\xi_{\parallel}^{PH}(h)}{\xi_0} = 1 + 0.5625\gamma + 0.3164063\gamma^2 + 0.0529785\gamma^3 + 0.135269\gamma^4 + 0.197915\gamma^5 \dots, \quad (2.26)$$

as a function of the height from the boundary, h ($\gamma = a/h$). The friction coefficient of the perpendicular direction has the similar characteristics than the power series of the free interface case:

$$\frac{\xi_{\perp}^{PH}(h)}{\xi_0} = 1 + 1.125\gamma + 1.265625\gamma^2 + 0.9238281\gamma^3 + 1.00415\gamma^4 + 1.215118\gamma^5 + \dots \quad (2.27)$$

The authors compared this expression with the analytical model of Brenner Eq. (2.20) finding well agreement. In both directions the friction increases as $h \rightarrow a$.

2.3.3 Solutions for a planar fluid-fluid interface

The theoretical approach considered in this work for a fluid-fluid interface is based on the publication of Lee *et al.* [36]. They examined the solution of the Navier-Stokes equations for the disturbance generated for a spherical particle wholly immersed in one fluid (fluid II) approaching to a planar fluid-fluid interface, for a creeping flow approximation. Their work was supported on the application of the reciprocal theorem to determine the general solution for fluid motion in the presence of a flat rigid wall made by Lorentz [54] employing the stokeslet solutions and stream functions, therefore extending their solution to the general case of a fluid-fluid interface.

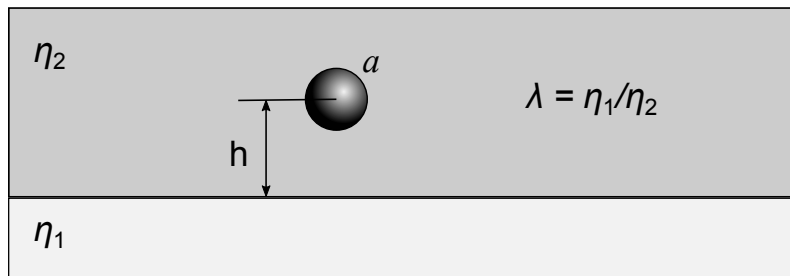


Figure 2.5. Sphere close to a fluid-fluid interface.

The assumption considered a spherical body with no-slip and null normal velocity boundary conditions at the particle surface. For the fluid-fluid interface they considered equal velocity at the contact interface, normal velocity with dependence on the small curvature generated at the interface by the disturbance flow. The viscosity ratio is $\lambda \equiv \eta_1/\eta_2$, and the interfacial tension also depends

2.3. Movement of a sphere approaching to a planar rigid wall or a planar free interface

on the ratio λ . Modifications to the Stokes' law giving by the translational component of the friction matrix in both directions are presented in function of the dimensionless distance $\gamma = a/h$. They obtained:

$$\frac{\xi_{\parallel}^{LL}(h)}{\xi_0} = \frac{D_0}{D_{\parallel}^{LL}(h)} = 1 - \frac{3}{16} \frac{2-3\lambda}{1+\lambda} \gamma + \left(\frac{3}{16} \frac{2-3\lambda}{1+\lambda} \right)^2 \gamma^2 + O(\gamma^3), \quad (2.28)$$

$$\frac{\xi_{\perp}^{LL}(h)}{\xi_0} = \frac{D_0}{D_{\perp}^{LL}(h)} = 1 + \frac{3}{8} \frac{2+3\lambda}{1+\lambda} \gamma + \left(\frac{3}{8} \frac{2+3\lambda}{1+\lambda} \right)^2 \gamma^2 + O(\gamma^3). \quad (2.29)$$

From this approach the typical conditions for a hard wall can be approximated as $\lambda \rightarrow \infty$ increasing the drag force in both directions, while as $\lambda \rightarrow 0$ the free interface conditions would be also approached since the drag force in parallel direction vanishes, both in well agreement with the theoretical expression gave in Sec. (2.3.2) and Sec. (2.3.1). A critical viscosity ratio is found for $\lambda = 1$ where it is understandable in regard of the immiscibility quality of the two fluids in contact, therefore the fluid would not behave as a whole entity of viscosity η .

2.3.4 Proposed model

We propose a model as combination of the results obtained by Perkins and Jones (PJ) for a free interface, and the second order corrections given by Lee *et al.* The well behavior of the numerical results of PJ since they removed the singularities at small distances from the interface, makes such model more attractive than the model presented by Brenner. The normalized friction coefficient obtained in parallel direction depending on the viscosity ratio λ is:

$$\frac{\xi_{\parallel}^{PL}(h)}{\xi_0} = \frac{D_0}{D_{\parallel}^{PL}(h)} = \frac{\xi_{\parallel}^{PF}(h)}{\xi_0} + \frac{15\lambda}{16(1+\lambda)} \left[\left(\frac{a}{h} \right) + \frac{3\lambda-12}{16(1+\lambda)} \left(\frac{a}{h} \right)^2 \right], \quad (2.30)$$

for a spherical particle of radius a , over the interface at a distance h . For the perpendicular direction respect to the interface, we obtained:

$$\frac{\xi_{\perp}^{PL}(h)}{\xi_0} = \frac{D_0}{D_{\perp}^{PL}(h)} = \frac{\xi_{\perp}^{PF}(h)}{\xi_0} + \frac{3\lambda}{8(1+\lambda)} \left[\left(\frac{a}{h} \right) + \frac{15\lambda+12}{8(1+\lambda)} \left(\frac{a}{h} \right)^2 \right]. \quad (2.31)$$

These expressions were tested on the limit conditions, showing the asymptotic behavior expected as $h \rightarrow \infty$, for an arbitrary λ . Moreover, the approach to a free interface is correctly obtained as $\lambda \rightarrow 0$, while for the approach to a hard wall is reproduced when $\lambda \rightarrow \infty$. In such way we propose only one theoretical formula-

tion to determine the normalized friction coefficient as a function of the height, for a planar fluid-fluid interface including the limit of a solid-fluid interface [23].

2.4 Optics in three-dimensional digital video microscopy (DVM-3D)

The DVM-3D takes advantage of the diffraction pattern generated by a defocused light point source. This section introduces the fundamental principles of the diffraction presented in our observations. This special optical aberration is understood through the point spread function of the light distribution at the image plane.

2.4.1 The point spread function

Before to define the point spread function (PSF), let consider a light point source far from a circular aperture of diameter $d \gg \lambda$, where λ is the light wavelength, and assuming that light travels through an arrangement aberration-free. The light is a spherical converging wave that reach the aperture hole. By the nature of the light, it is diffracted by the aperture producing a distribution light pattern at the back plane (Figure 2.6). Following the *Huygens–Fresnel principle* the light distribution is modeled by the *Fraunhofer diffraction* [71], and it is described by the Kirchhoff diffraction integral

$$U(P) = C \int_0^{2\pi} \int_0^a e^{-ik\rho w \cos(\theta-\psi)} \rho d\rho d\theta, \quad (2.32)$$

where $U(P)$ represents the scalar wave amplitude at the points P at the image plane in cylindrical coordinates (w, ψ) , C is the amplitude related to the light source, the back plane location, and the aperture conditions [72]. The intensity distribution at the back plane is given by the integral evaluation, yielding

$$I(P) = \{U(P)\}^2 = I_0 \left[\frac{2J_1(kaw)}{kaw} \right]^2. \quad (2.33)$$

This formula is widely known as the Airy rings description for the diffraction of a circular aperture of radius a , where $k = 2\pi/\lambda$ is the wave number of the light source of wavelength λ and the Bessel function of the first kind J_1 is used (top Figure 2.6).

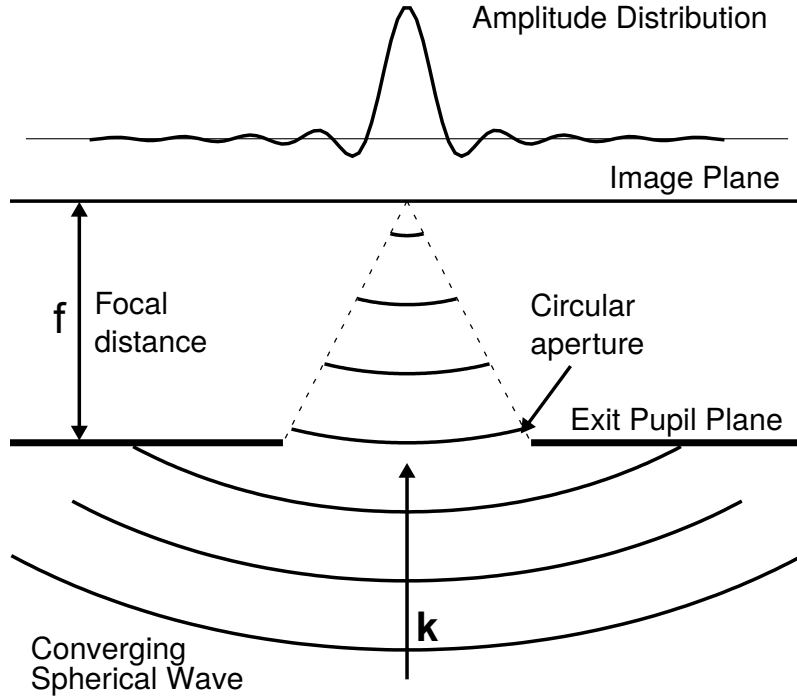


Figure 2.6. Fraunhofer diffraction for a circular aperture, giving the Airy disk intensity profile.

The light distribution in the focal plane of a well understood system is correctly treated by using the main ideas caught in the Fraunhofer diffraction formulation when the light crosses a circular aperture, however as the optical system has more elements the complexity in its study meets more developments. The study of three dimensional light distribution near focus which begun with Eugene Lommel in 1885 [73] studying the properties of the out-of-focus images formation for a monochromatic point light source, which is also detailed in more recent works like the treated gave by Wolf to the aberrations systems in [74] or directly in the applications to the 3D microscopy done by Gibson and Lanni [75].

Now consider a converging spherical wave which reaches the neighborhoods of the axial focal point, as the object is moved out-of-focus the back image plane is shifted by amount of Δz . Thus, the intensity distribution in the back image plane (x, y) becomes:

$$I(P) = \left| C \int_0^1 J_0 \left(\frac{2\pi a}{\lambda f} \rho \sqrt{x^2 + y^2} \right) e^{-i \frac{1}{2} \frac{2\pi}{\lambda} \left(\frac{a}{f} \right)^2 \Delta z \rho^2} \rho d\rho d\theta \right|^2, \quad (2.34)$$

where f is the focal distance. From this integral it is quite easy to see that as the amount off-of-focus distance goes to zero $\Delta z \rightarrow 0$, the intensity falls to the Airy disk case Eq. (2.33). This light distribution is also know as the *point spread*

function (PSF). Moreover, the equation (2.34) gives the amplitude distribution in the image plane produced in response to a point source at the origin of the object plane [76].

2.4.2 Analytical point spread function model for defocusing in oil-immersion microscopy

Gibson and Lanni [77] developed a straightforward way to understand and determine the PSF testing different aberration conditions for microscopy measurements such as [72, 78, 79]: index refraction mismatching between the immersion media, cover glass and the sample media, coverslip thickness variations, off-design location of the point light source, immersion thickness variation, or optical tube length displacement.

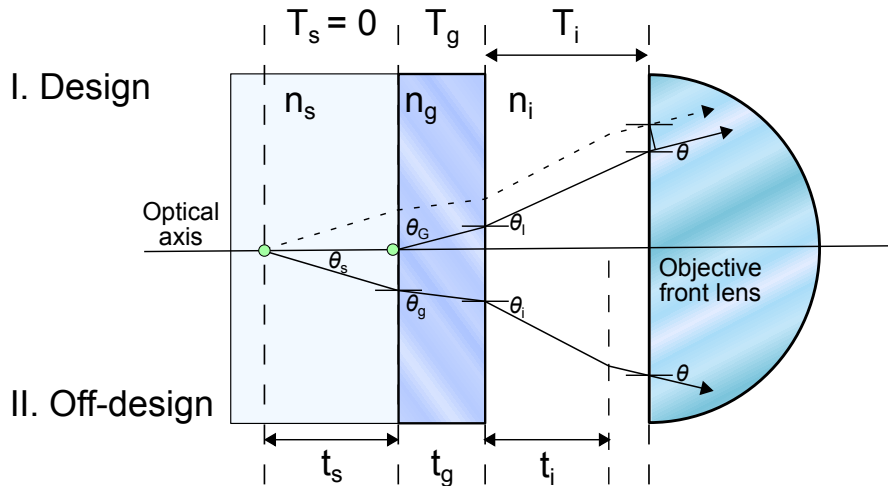


Figure 2.7. I. In design observation where the focal plane is placed at the object level $T_s = 0$, and the immersion media thickness is T_i . II. An off-design observation for an object located at the distance t_s into the sample media, where the thickness of the immersion media is modified at t_i , and the focal plane could stay at the object level. The optical path difference between both observations produces an optical aberration (using as reference the in design conditions).

Microscope objectives are manufactured to capture high quality images under the design conditions, using the common cover glass with standard thickness $T_g \sim 170 \mu\text{m}$ and refractive index $n_g \sim 1.52$, where an observed specimen should lay right down the coverslip where the distance from the cover glass is $T_s = 0$ (I. Design, Figure 2.7). For oil-immersion microscopy the immersion has refractive index match with the coverslip, reducing the light deviation through the medias. It is important to point the main contributions given by Gibson and Lanni:

- I. A correct definition of the optical path difference (OPD) of the light between the in-design and off-design conditions is crucial to establish the PSFs on each situation (Figure 2.7).
- II. The thickness of the cover glass does not contribute to the OPD.
- III. For an objective that satisfies the sine condition and planar front lens, the OPD can be approximated for a second order function of the defocusing and the media thickness Eq. (2.35).
- IV. Aberration is highly affected by the variation of the immersion media thickness. V. The OPD can be obtained from the objective specifications, magnification M , numerical aperture NA , parfocal distance f , and the working distance.

$$\begin{aligned}
 OPD \approx n_i \Delta z \left[1 - \frac{a^2 n_i}{f(f + \Delta z) NA^2} \right] \sqrt{1 - \left(\frac{NA\rho}{n_i} \right)^2} - \frac{a^2 \Delta z \rho^2}{2n_i f(f + \Delta z)} \\
 + n_s t_s \left\{ \sqrt{1 - \left(\frac{NA\rho}{n_s} \right)^2} - \left(\frac{n_i}{n_s} \right)^2 \sqrt{1 - \left(\frac{NA\rho}{n_i} \right)^2} \right\},
 \end{aligned} \tag{2.35}$$

where the off-design conditions t_s and t_i are the probe particle position respect to the inner cover glass wall and the immersion media thickness variation from the movement of the microscope stage Δz , respectively (II. Off-design, Figure 2.7). The OPD defines the phase aberration $W(\rho, \Delta z) = 2\pi * OPD/\lambda$. This function is used as input in the Kirchoff's integral of the PSF Eq. (2.34), then the PSF would get the shape,

$$I(x, y, \Delta z) = \left| C \int_0^1 J_0 \left[k \frac{NA}{\sqrt{M^2 - NA^2}} \rho \sqrt{x^2 + y^2} \right] \exp(iW(\rho, \Delta z)) \rho d\rho d\theta \right|^2. \tag{2.36}$$

Reaching a simplified method to obtain the PSFs to be compared with experimental optical aberrations. A detailed implementation of the Gibson and Lanni model can be found in Ref. [80]. The optical transfer functions are also used to determine the PSFs for defocused observations, that method is described in Ref. [81].

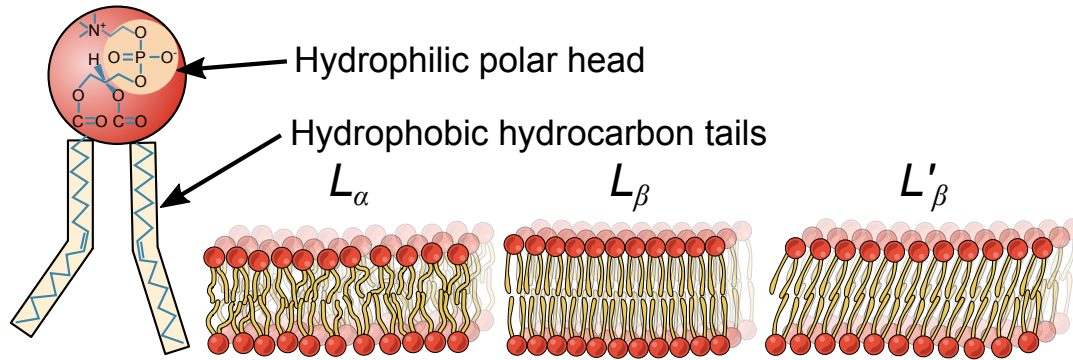


Figure 2.8. A DOPC phospholipid structure showing its polar head and the hydrocarbon chain as tails with a couple of double bounds (left). Three classical phases for a bilayer stack so-called lamellar phase (right).

2.5 Description of phospholipid bilayer membranes

The main constituents of any biological membrane are the phospholipids known as blocks of the cells. They belong to a class of substance called amphiphiles. A phospholipid is characterized by its polar hydrophilic head group and one or two hydrophobic hydrocarbon chains (so-called tails). In the regard of the combined hydrophilic-hydrophobic nature they form self-organized structure in water (Figure 2.8).

A plain membrane formation over a surface may appear as a bilayer stack. Bilayers are the most formed self-assembled structure for such phospholipids. The chemical potential of exchange between aggregates of different size plays an important role in the self-assembling regulation. The assembling process is studied through minimizing the free energy of the phospholipids inside the structures formed and in equilibrium with free lipids [82].

At high temperatures, phospholipids of bilayer membranes act like 2D fluids and solidified at low temperatures (below the main temperature T_m). However, in between these two conditions several possible phases exist (see Figure 2.8), [83]: The liquid lamellar phase called L_α (or liquid smectic crystalline phase), at high temperatures the phospholipid tails are 2D liquid with disorder. The gel phase L_β exists below the main temperature since the tails attempt to crystallize, although the head groups obstruct the process. Tilted phase L'_β is the gel phase where the molecules are tilted respect to the layer normal, a correct perpendicular packing is unreachable due to the heads size.

The structure of the DOPC lipid is shown in Figure 2.8. It has a polar head with a positive quaternary ammonium ion and a negative phosphate, linked by

a glycerol to two esters. The tails are attached to each ester in the middle. Each hydrocarbon chain has one double bound, that brings a lot of flexibility to this particular lipid. On the other hand the DMPC lipid has similar structure but no double bounds and shorter tails, showing a higher T_m and more global hydrophilicity.

2.5.1 Hydrodynamics near a fluid membrane

A fluid membrane (above its T_m) is easily deformed when submitted to external stresses by the solvent in contact, and thermally excited shape fluctuations. Close to a solid flat surface, such thermal fluctuations are hindered over large scales since it has to follow the surface flatness but still fluctuate at small length scales [84]. For a particle far from the bilayer it could be assumed that a thin liquid layer has negligible in-plane shear viscosity. The anisotropic mobility for a sphere approaching to a liquid-like membrane was studied by T. Bickel [85]. The hydrodynamic scattering effect in this system outcomes from the fluid flow produced by the colloid displacement exerting stresses that deform the membrane. Then as the bilayer relaxes to its equilibrium position, perturbing the media via a back flow that in turns affects the particle motion, and so forth.

The membrane Hamiltonian as is explained in Ref. [86], has a part that outcomes from the energy of a bending mode, and the other one from the confining potential μ [87], then for the Fourier representation

$$\mathcal{H}[h] = \frac{1}{2} \int \frac{d^2 \mathbf{q}}{(2\pi)^2} (\kappa q^4 + \mu) |h_q|^2, \quad (2.37)$$

$$h_q(t) = \int d^2 \boldsymbol{\rho} \exp(-i \boldsymbol{\rho} \cdot \mathbf{q}) h(\boldsymbol{\rho}, t), \quad (2.38)$$

expressing the energy for weak tension were the bending energy and the confining potential dominates over the strength of the tension, a suitable description for a liquid-like membrane. Where $h(\boldsymbol{\rho}, t)$ represents the height of the membrane in the real space for the lateral position $(x, y) \equiv \boldsymbol{\rho}$ and h_q its respective Fourier representation. The dispersion relation for an overdamped response from the membrane leads to the longest relaxation time in terms of the length at which the small q fluctuations are cut off,

$$\tau_m = \frac{4\eta}{\kappa} \varepsilon_{\parallel}^3, \quad (2.39)$$

where $\varepsilon_{\parallel} = (\kappa/\mu)^{1/4}$ being the membrane in-plane correlation length, η the media

viscosity, and κ the membrane bending rigidity.

On the other hand the typical time needed for a colloid to diffuse over its own radius,

$$\tau_d = \frac{\eta a^3}{kT}, \quad (2.40)$$

When $\tau_d/\tau_m \gg 1$ (i.e. $a \gg \varepsilon_{\parallel}$ or $\kappa \gg kT$), the membrane appears essentially flat to the colloid and the system is dominated by the relaxation dynamics of the elastic interface. Called the weak fluctuation (WF) regime. Then if $\tau_d/\tau_m \ll 1$ (i.e. $a \ll \varepsilon_{\parallel}$ or $\kappa \ll kT$), the body is strongly advected by random flow caused by thermal undulations of the membrane, and it is called strong fluctuation (SF) regime.

Hydrodynamic treatment is taking over the Navier-Stokes equations for a creeping flow, including an external force density causing the fluid motion, and the restoring force density exerted by the deformed interface. Such restoring force for smooth deformations uses the Hamiltonian Eq. (2.37) variation. Mobility tensor obtained by Bickel as frequency-dependent is written as the sum of the bulk mobility term and a mobility perturbation term.

Such perturbation recovers the limit expressions for a static membrane $\omega = 0$ leading the first approximation to the fluid-fluid interface [36]; on the other hand the high frequency limit $\omega \rightarrow \infty$, yields to the bulk mobility. The intermediate range for finite values of ω and for low frequency limit $\omega\tau_m \ll 1$ the normalized friction matrix can be expanded at lowest order, depending on the height h over the membrane,

$$\frac{\xi_{\parallel,\perp}^{LM}(h, \omega)}{\xi_0} = 1 + \alpha_{\parallel,\perp}^{(l)} \left(\frac{a}{h} \right) - \beta_{\parallel,\perp} i\omega\tau_m, \quad (2.41)$$

where the indexation goes over the direction whether parallel or perpendicular respect to the membrane surface, and the colloid radius a . Here the friction kernel depends on a single relaxation time, that comes from the delay in the response of the membrane to a deformation caused by the fluid flow. Coefficients from liquid-liquid approach [36]: $\alpha_{\parallel}^{(l)} = 3/32$ and $\alpha_{\perp}^{(l)} = 15/16$; the prefactors upon the distance h were obtained for $\varepsilon_{\parallel} \gg h$ written $\beta_{\parallel} = 0$ and $\beta_{\perp} = 3\pi a/16\varepsilon_{\parallel}$; and the other case for $\varepsilon_{\parallel} \ll h$ the expressions $\beta_{\parallel} = 9a\varepsilon_{\parallel}/64h^2$ and $\beta_{\perp} = 27a\varepsilon_{\parallel}/32h^2$.

Depending on the membrane response it could disturb the particle Brownian motion according the Eq. (2.41), which could be used as the relaxing time of the membrane τ_m is grater or comparable with the Brownian time τ_d , otherwise the hydrodynamics for a rigid wall is not affected by the membrane presence.

2.5.2 Damping response of a bilayer stack

For a single membrane with bending rigidity κ (in J), we might expect a surface tension γ (in J/m²) and the Canham-Helfrich Hamiltonian for low deformations linearization within the harmonic development of $\mu(\mathbf{r}_\perp)$ (see Figure 2.9) is [88]:

$$\mathcal{H}[h] = \frac{1}{2} \int_A dA \left\{ \kappa (\nabla^2 \mu(\mathbf{r}_\perp))^2 + \gamma (\nabla \mu(\mathbf{r}_\perp))^2 \right\}, \quad (2.42)$$

The fluctuation spectra at large scales is imposed by γ (or by presence of a surface for us) and by κ at small scales (see Figure 2.9), with a cut-off for both regimes around $q_{cross} = \sqrt{\gamma/\kappa}$.

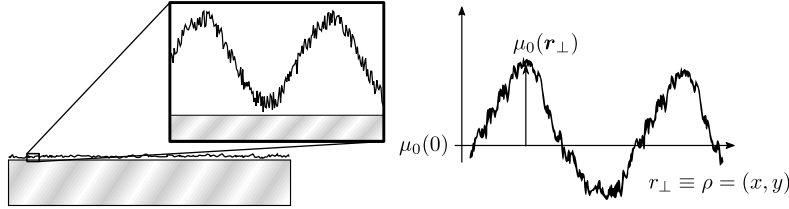


Figure 2.9. A single membrane bilayer on a flat surface at large scales is considered flat. The bilayer roughness is given by $\mu_0(\mathbf{r}_\perp)$.

The membrane roughness is obtained by decoupling the wave vectors in the Fourier space (RMS in Fourier space):

$$\left\langle |\tilde{\mu}(q_\perp)|^2 \right\rangle = \frac{1}{A} \frac{kT}{\gamma q_z^2 + \kappa q_\perp^4}, \quad (2.43)$$

and by integration on all modes in real space [89]:

$$\left\langle |\tilde{\mu}(r_\perp)|^2 \right\rangle \equiv \sigma_{RMS} \sim \int_{q_{min}}^{q_{max}} dq \mathcal{F}(q) \quad (2.44)$$

$$\sigma_{RMS} = \frac{kT}{4\pi^3 \kappa} A. \quad (2.45)$$

In stacks fluctuation the modes are coupled. Based on the previous considerations for a bilayers stack, σ_{RMS} is obtained (Parseval's theorem):

$$\left\langle |\tilde{\mu}(\mathbf{q}_z, \mathbf{q}_\perp)|^2 \right\rangle = \frac{kT}{Bq_z^2 + Kq_\perp^4}, \quad (2.46)$$

and

$$\left\langle |\tilde{\mu}(\mathbf{r}_\perp)|^2 \right\rangle \equiv \sigma_{RMS} \simeq \frac{kT}{8\pi\sqrt{BK}} \ln(N), \quad (2.47)$$

where N is the number of membranes, $B = -d(\partial\Pi/\partial d)$ the bulk compressibility modulus (in J/m^3), and $K = \kappa/d$ the bulk bending modulus of the stack (in J/m). The mentioned values are applied to a stack of bilayers with a thickness of d . From this, Pierre-Gilles de Gennes introduced the smectic penetration length $\lambda = \sqrt{K/B}$ that can be used to evaluate the length of propagation of a deformation in plane (see Figure 2.10) or of a perturbation of the stack d -spacing (z order).

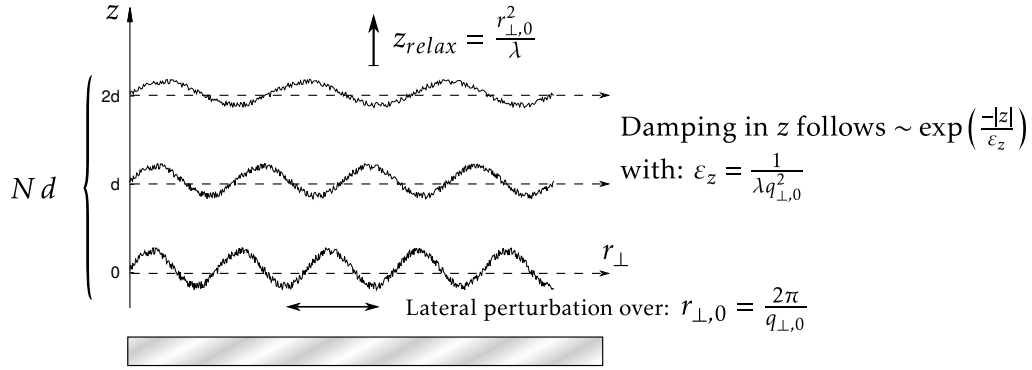


Figure 2.10. Damped fluctuations for a stack of N bilayers over a flat solid surface. The d -spacing bilayers have a damping coefficient ε_z .

The presence of the substrates (flat interface) kills large scale in-plane fluctuations so that if one calculates the “roughness” in the stacks and how fluctuations are damped the picture can be summarized as it is depicted in Figure 2.11.

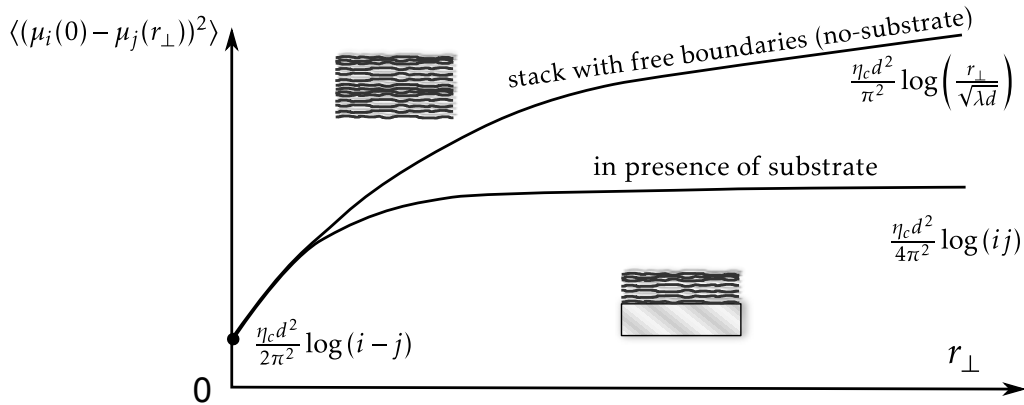


Figure 2.11. Damping response for an embedded membrane in a stack of membranes (solid supported smectic phase, L_α).

Where we introduced the Caille parameter [90], η_c , related to disorder propagation in the stack:

$$\eta_c = \frac{\pi}{2} \frac{kT}{d^2 \sqrt{KB}}. \quad (2.48)$$

A charged membrane stack with extreme space $d = 250 \text{ \AA}$ between layers can have fluctuations of the order of tens angstroms. Tabulated with the roughness of a few bilayers, if we compared this perturbations scale with a colloid diameter of $1 \text{ }\mu\text{m}$, it is straightforward to conclude that the membrane do not produce a fluctuation able to modify the particle movement. The consideration gave by T. Bickel [85] concerning to the scales when $\tau_d/\tau_m \gg 1$ (i.e. $a \gg \varepsilon_{\parallel}$ or $\kappa \gg kT$) reduces the hydrodynamic interaction to the hard wall case.

3 Experimental Procedures

This chapter explains how colloidal suspensions were prepared, how the cells were designed, and how the three dimensional Digital Video Microscopy (3D-DVM) technique works.

3.1 Samples

This first section describes the samples preparation for all experiment that were carried out. It is presented in the form of two experimentations: free surface, and solid supported membranes

3.1.1 Experiments on soft interfaces

The experiment was designed to study how the hydrodynamic interactions affects the dynamics of an isolated colloid close to an interface. In this case the boundary is a flat over large scales an air/water interface (obtained by the modification of the standard sample cell used in our previous experiments). For this, we realized an enclosed environment to observe microscope slides drilled in the center with different hole diameters (we used holes of 7 mm of diameter after optimizing between the system stability and the observation field).

Water purification

Ultrapurified water was used to prepare the samples made in Cinvestav, such water was taken from the main pipe water supplier, then filtrated twice before to get the distiller (Barnstead MP1 Mega-Pure). Water was cleared removing from it nitrates, bacterial presence, sodium, heavy metals, washing away around 99.5 %

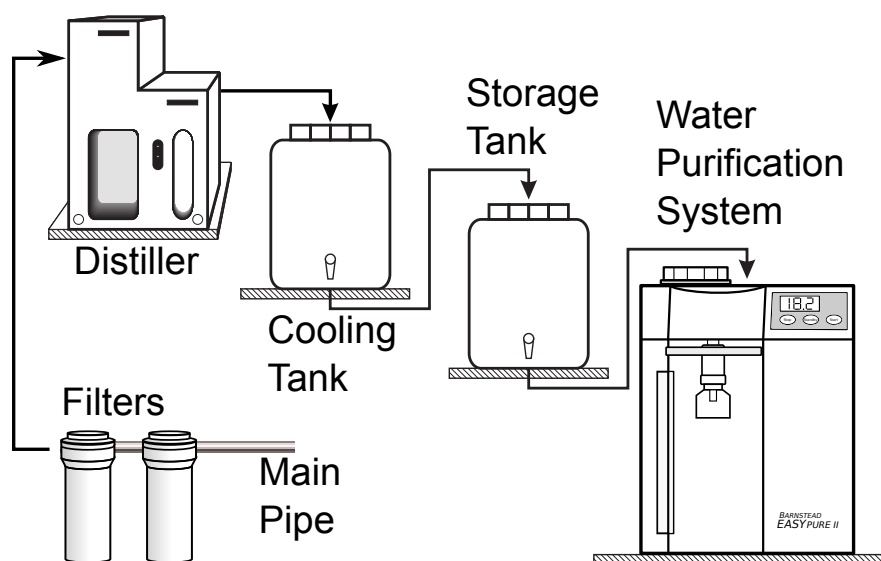


Figure 3.1. Sketch of the water purification process.

of pollution in the water. In the next step, the water is stored while its temperature decreases rather to feed with it directly the purifier, then only if the stored water gets room temperature it is allowed to load the purifier (Barnstead EASY-pure II RF) where the water is deionized getting a resistivity of $18.2 \text{ M}\Omega\cdot\text{cm}$, this process sequence is depicted in Figure 3.1. Is worth to recall that same water is used further to clean the glass supplies.

Colloidal suspensions

The suspensions used in the experiments were prepared using ultrapurified water at $18.2 \text{ M}\Omega\cdot\text{cm}$. We added NaCl at 10 mM, then the dispersion was obtained using fluorescent polystyrene colloids of $1.0 \mu\text{m}$ in diameter, that were purchased from Thermo Scientific™(ref G0100, with polydispersity below 3% in size), its fluorescent dye is excited in blue at 468 nm and emits in green with a peak at 508 nm. Several types of dilutions were made by successive tuning down the concentration, pulling $5 \mu\text{l}$ of the master colloid suspension in 3 ml of ultrapurified water and salt 10 mM, then from that main suspension 1.25 ml was mixed in 2.75 ml of the same salty water, repeating this twice, so that the final particles concentration was set to approximately 400 spheres/ μl .

At this stage, the sample at low concentration contains less hydrodynamical interactions between colloids. It would correspond to an electrostatic screening length of $\sim 3 \text{ nm}$ from the salt (so a neglectable range of electrostatic interaction). Nevertheless, in observations a reduced amount of colloid aggregation showed due to ultra-short range repulsions (electrostatic and hydration force).

Cell preparation

Drilled microscope slides were used for each sample, where each slide was perforated by sand blasting at its center. In this way a slide would provide a suitable cavity where the air will get trapped allowing the formation of an air/water interface (hole of 7 mm in diameter). Then the cell will be assembled joining one drilled microscope slide, one plain microscope slide, and one cover glass (microscope slides and cover glass were supplied by Cole Parmer. See Figure 3.2).

The cell parts were cleaned before silanization of the glassware. The whole glassware was washed in ultrapurified water with a phosphate free detergent (HYCLIN PLUS from Hycel, Mexico) and successive flushes in boiling water, they were cleaned following these steps: first, a pyrex beaker is loaded with ultrapurified water and detergent, then the glasses are put into this solution on a PTFE rack. During the washing, the beaker was heated at 270 °C. Above the boiling point, the vessel was flushed with ultrapurified water, afterwards they are again immersed in water and left until boiling point again. This last step was repeated three times. Afterwards the glassware was left on a warm environment for the complete evaporation of the remaining water drops on the glass surfaces.

Silanized protocol of glass

The surfaces of the drilled slides were silanized to made them hydrophobic. The slides are first immersed one-by-one in a mixture of 13.3 g of bicyclohexil (Sigma-Aldrich) with 30 μ l of octadecyltrichlorosilane (Sigma-Aldrich) for 6 min and then they were dried under a gentle flow of argon. In the next stage, these pieces of glass were sonicated in toluene (Sigma-Aldrich) to facilitate the elimination of water traces and the non-anchored silane molecules. The resulting hydrophobic surfaces impose a contact angle larger than 100 degrees.

Samples Preparation

The parts were sealed. Some plastic strips of about 300 μ m were glued on the drilled slide surrounding the hole with epoxy resin (EPO-TEK 302) as shown in Figure 3.2. The resin is widely used for optic applications due to its refractive index matching with cover glasses and its strong resistance on glass. A hermetical container was obtained to enclose the suspension with a low interaction with the resin once dried.

A cover glass on the square made from the strips, was gently pressed down guaranteeing no direct connection between the inner cell and the exterior (see

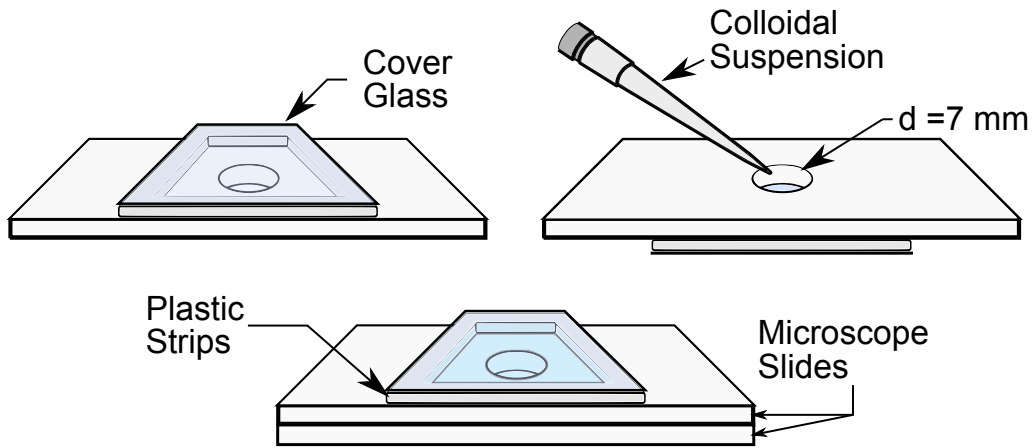


Figure 3.2. Sketch of cell and sample preparation.

Fig. 3.2). Once the resin dried, the cell is turned upside down leaving the hole up. Then the cell was filled with the suspension in two steps: First it was filled with $16 \pm 2 \mu\text{l}$ of suspension. In this way it is possible to have a good depth of observation under the cover glass, reaching about $\sim 300 \mu\text{m}$. Finally, the cell was carefully turned again, taking the hole down. The cell was sealed with a microscope slide using epoxy resin (as shown in Figure 3.2).

Time before observations is at least two hours, so that the suspension reaches equilibrium and the resin dried. Figure 3.3 shows the final side view of the free interface sample (free interface on the top of the cylindrical hole letting enough observation field far from the circular edge where the observations is not recommended). A good depth of observation in the sample is obtained in this way between $300\text{-}360 \mu\text{m}$.

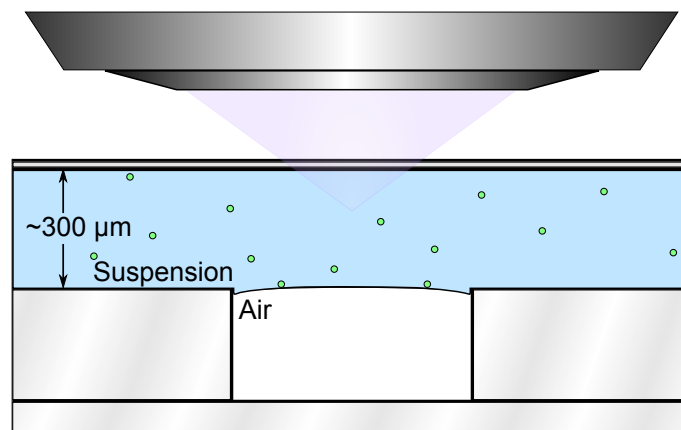


Figure 3.3. Side view of the cell. The observation zone can reach $100 \times 100 \mu\text{m}^2$ then this 7 mm hole is well adequate to an observation.

3.1.2 Experiments on solid supported Membranes

This set of experiments were conducted at the IMMM (institut des molécules et des matériaux du Mans) of the Université du Maine. All procedures are explained in detail highlighting differences with the previous measurements made in Cinvestav.

Suspension

In addition to the same protocol presented previously the polymer poly(ethyleneglycol) (PEG) 20 kD bought from Fluka, was used to control the osmotic pressure with a concentration w/w of 3.6 %. It is worth to note that different PEG concentrations were tested looking for the best match between osmotic pressure and the viscosity of the solvent.

Materials

All the samples were prepared on the usual microscope slides and cover glasses from Cole-Parmer. They were first rinsed in water, then cleaned with ethanol before cleaning by irradiation from ozone-produced under UV lamp in a UVO-Cleaner (model 42). This treatment breaks the organics molecules on the glass surface and extracts the residues by means of air flow. Afterwards 15 min of procedure an hydrophilic glass surface exhibited a water contact angle below 1 degree. As separators in Kapton of 120 μm thickness was used instead of plastic strips. In some cases GENE FRAME II (from Thermo Scientific) square stickers were used providing a sealed regular height of 280 μm .

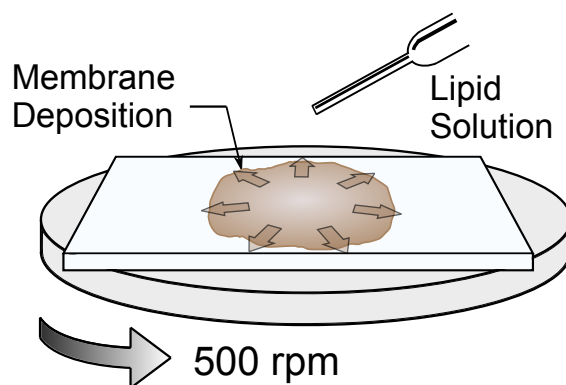


Figure 3.4. A volume of 50 μl is dropped down over a cleaned microscope slide either DMPC or DOPC lipids dissolved in chloroform and TFE, coating the substrate during 1 min at top speed of 500 rpm.

Lipid Solution

Two types of lipids were used 1,2-dimyristoyl-sn-glycero-3-phospho- choline (DMPC) and 1,2-dioleoyl-sn-glycero-3-phosphocholine (DOPC) from Avanti Lipids (dried powder). Both lipids were used without further purification. Each was dissolved in a suitable organic solvent for total solubilization (a mixture of chloroform and trifluoroethanol (TFE), supplied from Sigma-Aldrich), the solvent also gives a good wettability of the substrate (mixture 1:1 of chloroform and TFE). Simultaneously, chloroform has hydrophobic properties inducing drop spreading and TFE is more hydrophilic and favor membrane attachment to the substrate [91]. Lipid solution concentration was 10 mg of lipid in 1 ml of the organic solvent mixture. Prior to use this preparation was kept in fridge.

Membrane deposition on substrates by spincoating

Both lipid samples were prepared on a substrate by the spin-coating technique [91], the lipid solution was pipetted centrally on the surface in an amount of 50 μl , then the spin coater started of a top speed of 500 rpm with an acceleration of 500 rpm/s, during 60 seconds. Thus, the solution spreaded over the surface wetted the whole substrate. Low rotation speed gives a membrane stacks with several bilayers. The fast evaporation of the solvent is fundamental to have a well-defined multilayer number over the substrate then at the same time the membrane collects some water from the air around once part of the organic solvent evaporated. These samples were stored under high vacuum pumping during 24 hours, to take out the organic solvent traces from the multilayer. Figure 3.4 shows how the lipid solution was dropped on the substrate.

Sample cell preparation

So far, the multilayer membrane was deposited on the substrate surface, thus the cell should be designed to keep it stable in air. Some parts of the membrane were then carefully cleaned from the substrate, leaving a multilayer square of $1 \times 1 \text{ cm}^2$ in the center. After the resin dried we loaded the suspension with a volume of 60 μl . As the cell is full these two entrance are closed without contact between the suspension and the resin, then the sample was stored for 1 hour and a half while it reaches convection equilibrium.

Figure 3.5 shows the way that a typical sample cell is loaded. Figure 3.6 shows a sketch of the side view for a sample cell with the membrane multilayer in the

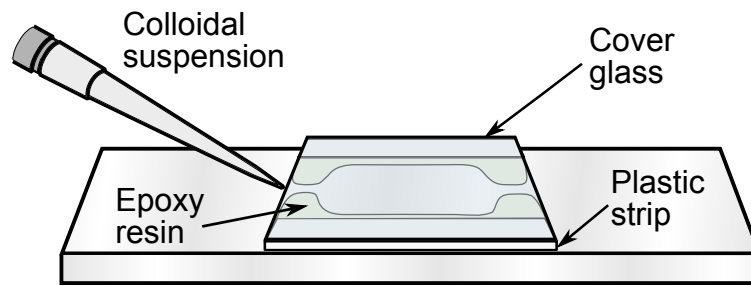


Figure 3.5. A typical sample cell design where the separations between the glasses interfaces is controlled by the plastic strips thickness. Suspensions are pipetted into the cell from one side with the other opened and then both are sealed using epoxy resin.

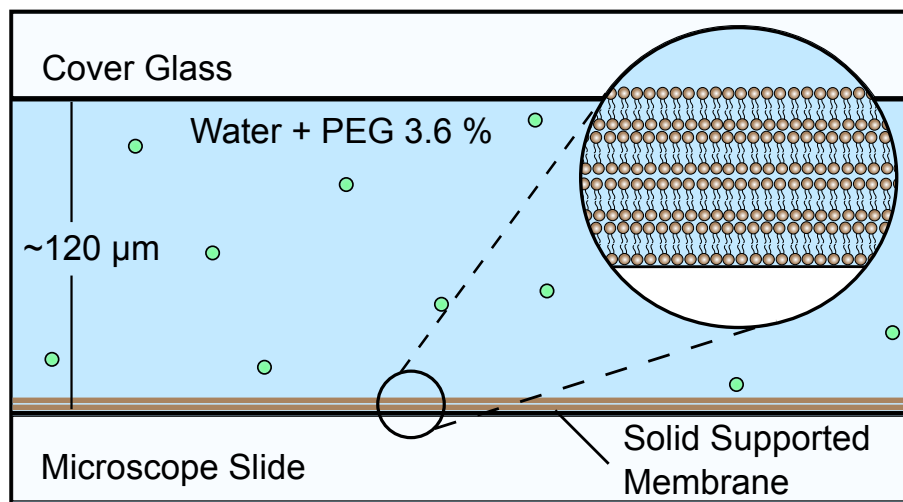


Figure 3.6. The cell height is $120 \mu\text{m}$, hereby the membrane was deposited on the cell bottom glass interface by means spincoating, resulting in a multilayer stacks of membranes with few bilayers.

bottom, here the distance between the glasses interfaces in $\sim 120 \mu\text{m}$, given by the Kapton thickness.

3.2 Three Dimensional Digital Video Microscopy (3D-DVM)

This work was carried out in two different experimental places, one settled in Cinvestav (Mexico) and other one at Université du Maine (France), at the end, they showed equivalent results under the test observations allowing us to validate membrane experiments in France. This section presents the main aspects of the technique. Since the microscopes, cameras, and objectives are completely

different in both places it is necessary to describe each one apart, including its calibrations.

Digital video microscopy is a powerful technique of particle tracking from sequences of digitized images able to determine the particle's dynamics. Matlab was used to strip the images by a brightness profile recognizing the brightest zone of connected pixels as a particle in each image. Then via $z(r)$ relates the position on z direction over its characteristic diffraction pattern. The characteristic diffraction of each fluorescent particle arises due to the deviation of the optical path of the light through three media from the light source to the detector [21]. Those diffracted rings appear since the particle position is defocused below the focal plane, on the other hand if the particle is located over the plane it will look as a blurry spot (this optical aberration behavior was explained by Frisken and Lanni [77] through the point spread function analysis). We used a suitable dichroic cube allowing us to send the emitted light in a wavelength capable of exciting the fluorescent dye in the particle core, hence the light emitted was measured in the form of digital images via a CCD camera.

We recall here some generalities about the 3D-DVM microscope. Among the objectives available in the market it is relevant to choose 100× objective. In biological observations, those objectives were designed for observations right below the cover slip using optical oil whereby the optical match between the thin oil layer and the cover glass refractive index leaves apart optical aberration only at the focal plane level, otherwise everything out of the focal plane is out of sight. On the other hand there are the 100× air objectives family, with less numerical aperture. Although these objectives allow one to reach observations few microns below the focal plane, in addition the long working distance empowers to reach deeper longitudes inside the suspension. Here is also important to recall that is the numerical aperture (N.A.) which is a key factor to the performance of objective lens (resolving power, focal depth, and brightness). The N.A. is determined as the refraction rate of the medium between the observed specimen and objective lenses against the sine of the angle $NA = n \sin \theta$ [92]. This value later can determine the visual field brightness of the microscope which is related to the magnification.

A microscope capable to work on fluorescence microscopy should have for instance, a mercury arc lamp aside the traditional transmitted light below the movable stage. Mercury vapor at high pressure gives a luminosity of the arc that can reach 10 to 100 times more intensity than an ordinary tungsten filament incandescent lamp, with a wide spectrum in the white light allowing to use dif-

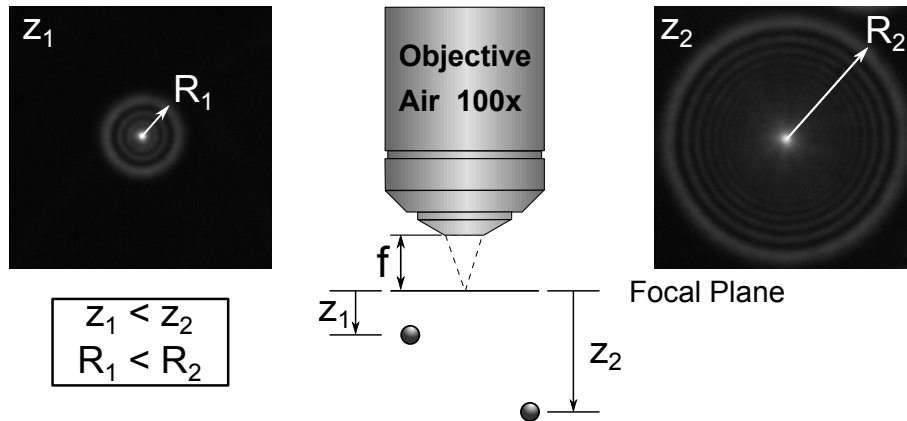


Figure 3.7. Two different fluorescent spheres of $1 \mu\text{m}$ visualized at two different depths under the focal plane, showing two diffraction patterns characterized by the radius of their outer ring.

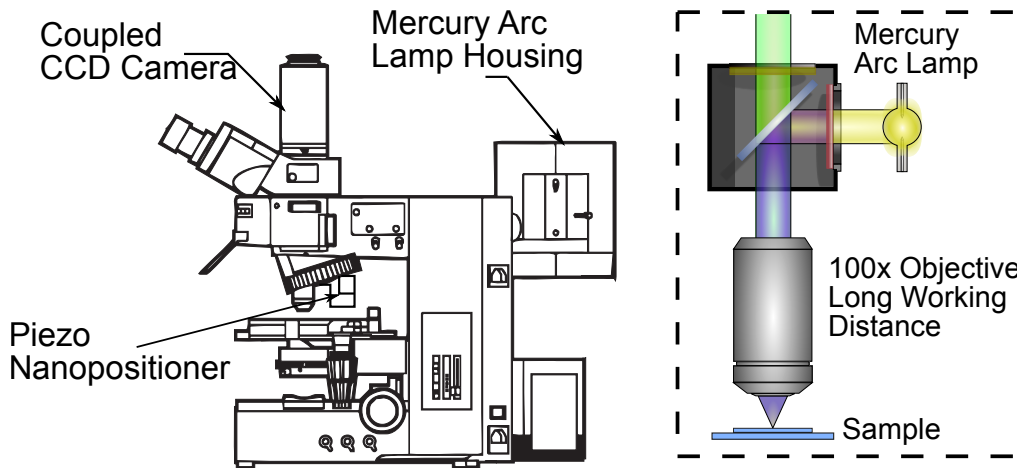


Figure 3.8. Microscope design is shown at the left CCD camera is coupled at the top, at the back it is found the mercury arc lamp, attached at objectives gear is the nanopositioner which electronically focus the objective. At the right the dichroic mirror splitting the light keeping blue in reflection and letting pass through green light wave length to the CCD camera.

ferent kinds of fluorescent compounds (it is easier to tune the light by the use of an appropriate filter, providing an intense illumination for a specific wavelength band along the visible spectral). The Figure 3.8b outlined the way that the light from the mercury lamp reaches a filter and a particular wavelength is deviated by the dichroic mirror sending the light through the objective over the fluorescent suspension. Their emitted fluorescence goes back through the objective passing along the dichroic cube to the exit filter in the upper part to the CCD camera. Depending on the experiments to do and the fluorescence of the samples then different dichroic cube were chosen.

In respect to the camera we see a clear difference between the interlaced one and the progressive one used in this work. The interlaced camera sends an image with a very small delay in time within the pixel lines in the image making difficult to realize with enough precision the images, for this reason it is recommendable to use progressive cameras where the image is taken at once.

3.3 Measurements at Cinvestav (Mexico)

This section describes set up used at Cinvestav, including the used calibration procedure.

3.3.1 Microscope

Samples were observed in a microscope Olympus BX60 with a mercury arc lamp (OSRAM HBO 100 W/2), an objective LMPLFLN 100 \times . This particular objective has a long working distance (WD) of 3.4 mm, also its reference belongs to the plan semi apochromatic type which gives a high-level correction for chromatic aberrations, regarding in its WD is able to work without colliding the sample cell while the observations. Its numerical aperture 0.8 [92], which is plenty enough for this kind of experiments.

In our observations the microscope is equipped with an Olympus dichroic cube ref: U-MNBV2 (band-pass filter between 420-480 nm and cut-off filter at 475 nm), dichroic mirror 455 nm, then the light over the fluorescent beads is in blue ultraviolet and emitted in green according to the fluorescence particles specifications. The image sequences are taken using a monochromatic progressive CCD Camera Link COHU 7712-200 with a pixel size in the optical geometry arrangement given by 1 pixel = 0.147 μm , this size is obtained in the traditional way using a micrometer slide (provided by Olympus) which was put on the stage using the 100 \times objective then a high contrast snapshot was taken to finally count

the pixels between the marks in the image (that measure was done using the ImageJ tools). This camera is set at the speed of 30 fps (frames per second), and under computer limitations which is able to store series of 1500 frames in the temporary RAM memory before to write them in the HDD where a sequence of high quality images is given in TIFF format of 16 bits of depth (~ 1.2 MB each).

Figure 3.8A shows the usual microscope parts in Olympus BX60 model, in the back side is the mercury arc lamp housing, in the top the CCD camera is shown with a video camera adapter Olympus U-TV0.5XC C-mount video port with additional magnification of $0.5\times$ lens, which is a low-magnification camera adapter with C-mount which allows a digital imaging device to capture wide-angle images. By using a thread adapter the objective is mounted in the piezo nanopositioner, besides is the conventional transmitted lamp housing which illuminates the stage from the bottom. This second light is useful to find particles that are stick on the cover glass inside the cell.

3.3.2 Calibration measurements

This section describes the calibration set up, that means the correct relation between the particle position below the focal plane using their diffraction pattern. This task was accomplished collecting the rings changing profile doing several scans upward using a programmable piezo controller E-662 LVPZT to operate the objective nanofocusing Z-drives PIFOC P-721 unit attached at the revolving nosepieces. In this way, the objective movement can be accurately controlled without introducing any inertial response generated by the stage movement.

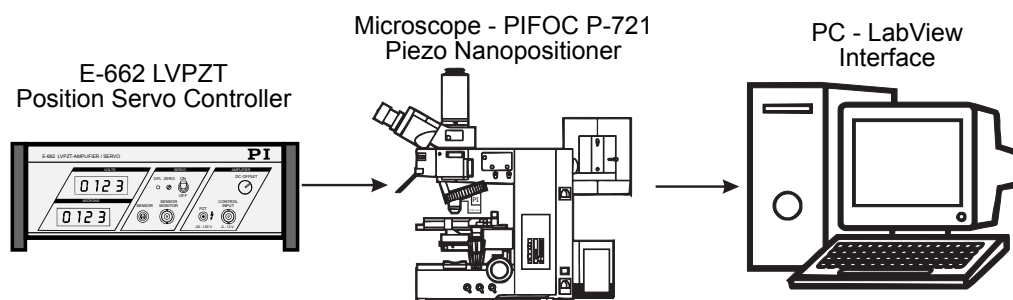


Figure 3.9. Sketch of the interfase used to operate the piezo controller fram a computer, and finally recording the images.

The samples used were prepared with ultrapurified water, and two types of fluorescent particles of $1.0\ \mu\text{m}$ and $0.3\ \mu\text{m}$ in diameter. This mixture in a proportion of 1:30 respectively is useful to find the bottom of the cell. Here the designed cell has a vertical thickness of $300\ \mu\text{m}$ where it was loaded with the suspension

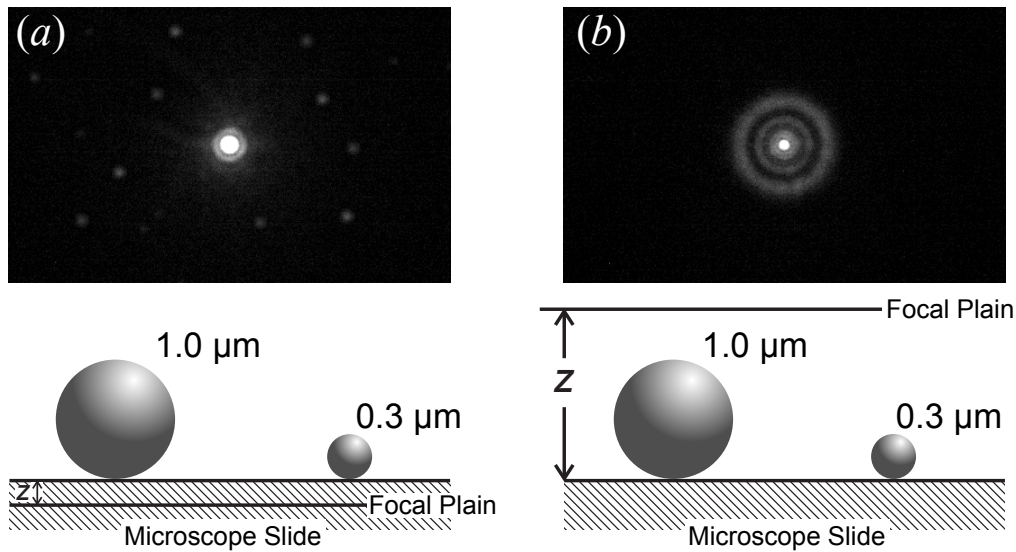


Figure 3.10. During the calibration the focal plane crosses the spheres at the bottom. Fig. (a) small spots are visible and the biggest spot for $0.3\ \mu\text{m}$ and $1\ \mu\text{m}$ spheres respectively (the focal plane could be at bottom level). Fig. (b) just a $1\ \mu\text{m}$ sphere is seen and its diffraction pattern is visible (hereby the focal plane could be more than $10\ \mu\text{m}$ ground over).

and stored until all the beads got sedimented to the bottom. Then the focal plane was located few microns around the glass interface getting into the microscope slide, so the $1\ \mu\text{m}$ particle would look like a big blurry spot. Hence the piezo controller was programmed to do a scan upwards in steps of $0.1\ \mu\text{m}$, this was managed by a computer using a LabView interface which sends the instructions to move the focal plane by the electro-mechanical nanofocusing device while the camera takes shots on each step. Along the sequence, it is also clear that the change from a blurry spot to a well defined circle then to a brightness point surrounding by few discrete concentric rings, making doubtlessly such monotonic transition in the ring sizes.

It is important to mention that the main purpose of the calibration is to locate the polystyrene spheres, however for an $1\ \mu\text{m}$ sphere it is difficult to identify when the focal plane is located at its center because its brightness is so much intense over 4-6 steps in the z -drive scale. Thus, we take advantage of the $0.3\ \mu\text{m}$ spheres due to their less brightness intensity under this specific optics ($100\times$ objective). Furthermore, it would be easier to follow the brightness profile along $\sim 5\ \mu\text{m}$ up to the cell bottom over the small particles (see Fig. 3.10), for them as the focal plane is further away of $\sim 6\ \mu\text{m}$ of these small spheres, they would not be longer visible.

The information gathered was analyzed to know where is the center of the

small particles. Four or five small spots are picked then over the images and where the spot is visible, a weighted brightness profile was made for each chosen particle, giving a curve with a local maximum. These curves are superposed and fitted to get analytical expressions which correspond to the exact frame where the maximum happened. This was done using the tools from ImageJ, hence from this value it is possible to figure out where is the center of the bigger particle by a mere subtraction.

So far, the system performed a scan over $100 \mu\text{m}$ collecting at the end 1000 images which have been analyzed using a Matlab script, giving an exponential relation between the outer ring radius that changes respect to the z depth controlled from the nanofocusing device. Therefore, this trial was repeated 8 times so the data were overlapped employing as a reference, the small particle's center reaching at the end just one exponential curve $R(z)$ [1], later it was fitted by Origin 8.0 tools to the model function

$$R(z) = A \exp(z/B) + C, \quad (3.1)$$

where A , B , and C are fit parameters used to complete the detection script in Matlab with the inverted function $z(R) = B \ln((R - C)/A)$. Data and fit used to achieve the relation $R(z)$ are shown in the left side of Figure 3.11, whereby some examples diffraction patterns are also shown in the insets.

For this calculation about the calibration, the optical path deviation of the light rays trough the whole lenses and medias should be taken into account, therefore it is important to verify the quality of the calibration, hence this would be tested using a sample cell of $\sim 600 \mu\text{m}$ in the same way like that was shown in Figure 3.5. The highly diluted suspensions with 10 mM of NaCl were used to measure bulk self-diffusion in all direction. Since the calibration data was taken in a cell of $\sim 300 \mu\text{m}$ then the focal plane must be set in similar conditions, thus the focal plane was located at the cover glass level into the suspension (this was done finding particles sticked on the cover glass). Afterwards, the focal plane was moved at $280 \mu\text{m}$ in depth into the suspension, as consequence the observed particles were far from the boundaries to get bulk conditions.

More than 300 trajectories were collected with 1500 steps each, from them the bulk self-diffusion at $25 \pm 1^\circ\text{C}$ was compared with the theoretical diffusion $D_0 = 0.481 \mu\text{m}^2/\text{s}$ as shown with a solid line in Figure 3.11b. The shaded zone represents the theoretical boundaries for the temperature uncertainty. Diffusion values in z direction were treated by an auxiliary script which iterates the diffusion calculation using as the first input the fitted parameters obtained from the

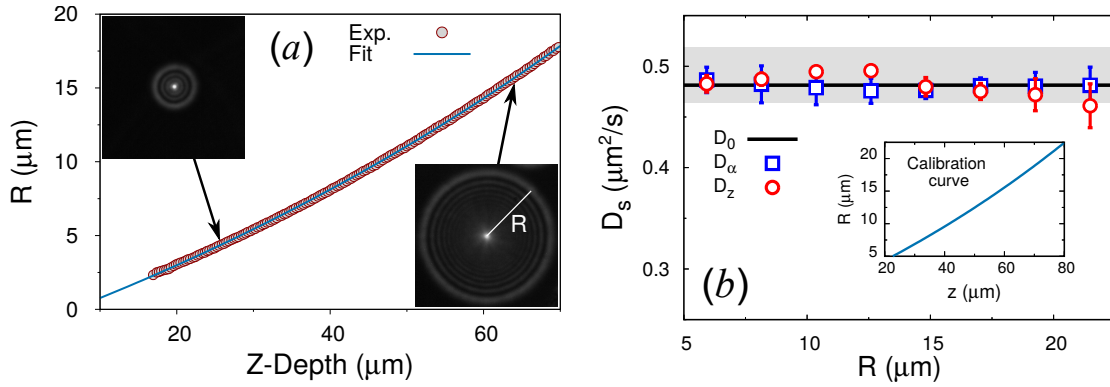


Figure 3.11. (a) Shows the calibration fitting over the data collected from the calibration procedure along 4 repetitions. In the inset the images that belong to the indicated points. (b) bulk self-diffusion coefficient obtained. The continuous line is the Stokes-Einstein diffusion coefficient D_0 with its corresponding uncertainty band (gray region). The squares (circles) are experimental measurements of the self-diffusion coefficient D_α in the x - y plane (D_z in the z -direction) as a function of the radius R of the external ring. The equivalence between the diffusion coefficients in both directions was obtained through the calibration curve shown in the inset.

experimental calibration data. This scripts would iterate the three parameters in the exponential function until it minimizes the difference between the self diffusion coefficients keeping as reference the diffusion in x - y which were obtained in a direct way, the final values reached by the iterative method are plotted in the inset of Figure 3.11b,;

$$R(z) = 30.8437 \exp(z/145.2783) - 31.0573. \quad (3.2)$$

These results which confirmed the accuracy of the measurements presented in Figure 3.12, where whole data shows well defined Brownian motion. The insets show histograms at two diffusive times with a correct Gaussian distributions, which are compared with the theoretical distributions for the diffusion coefficient D_0 .

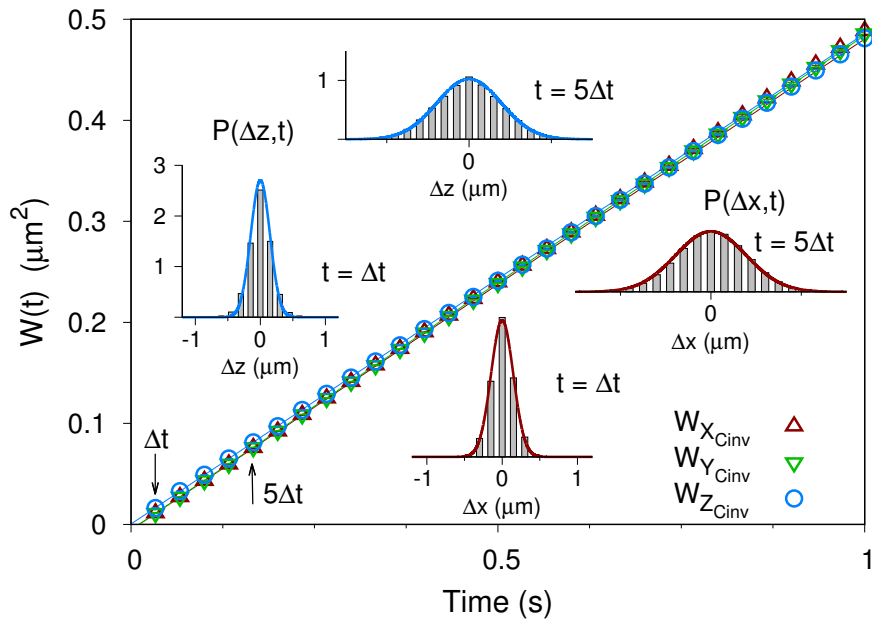


Figure 3.12. Mean square displacement (MSD) determined by means of 3D-DVM in the directions x,y,z respect to the focal plane showing linear behavior at diffusive times and a good correspondance between them. Some probability distribution histograms are drawn in the insets for two diffusive times $t = \Delta t$ and $t = 5\Delta t$ with their respective theoretical function that outcomes from D_0 .

3.4 Measurements at the Université du Maine (France)

3.4.1 Microscope

In the experiments at Université du Maine the 3D-DVM was performed using an Axio Scope A1 Carl Zeiss microscope. This microscope with an EC Epiplan-Neofluar 100 \times objective of 0.9 N.A with a working distance of 310 μm which limited the observations to a low depth range into the suspension, to recall that this objective family from Zeiss are the Enhanced Contrast Plan Neofluar. They minimized straylight with a visible increase in contrast methods also feature full chromatic correction for the focal plane and completely flat images for observation. In this case the focal plane was set at 70 μm under the cover glass, having around 70 μm of optical observation downward the focal plane location. Here the fluorescence is obtained with same mercury arc lamp and Carl Zeiss' filter set 16, that would accept light excitation wavelengths in the range of 485/20 nm, with a beam splitter FT 510 nm and emission LP 515 nm.

A monochromatic CCD Carl Zeiss camera AxioCam mRM set on the microscope.

This progressive camera is managed by the Axio Vision interface, which is a software provided by Carl Zeiss with fully functionalities for basic microscopy. A specialized module Time Lapse from Carl Zeiss is required to take sequence of images, therefore it was set to take images of high quality in TIFF format at 16 bits in depth (~ 3 MB eachs), however its speed would only reach 8 fps, it means time lapses of $\Delta t = 0.125$ s. The camera can reach higher speeds, however to increase the speed one should acquire the Fast Acquisition module from Carl Zeiss with a supplementary card to install and this was not possible. Nevertheless, it did not finally affect our determinations. In this set up the pixel size measured was 1 pixel = $0.0999 \mu\text{m}$.

3.4.2 Calibration set up

For this system another way to calibrate the set up was explored due to the absence of a piezo control. Therefore, the ring scanning was made manually using the microscope z-drive. Hence, in this microscope, the scale in the z-drive has a step of $4.2 \mu\text{m}$ which makes hard to collect property the data due to the particles size is barely $1 \mu\text{m}$, despite this, we performed the calibration with a usual

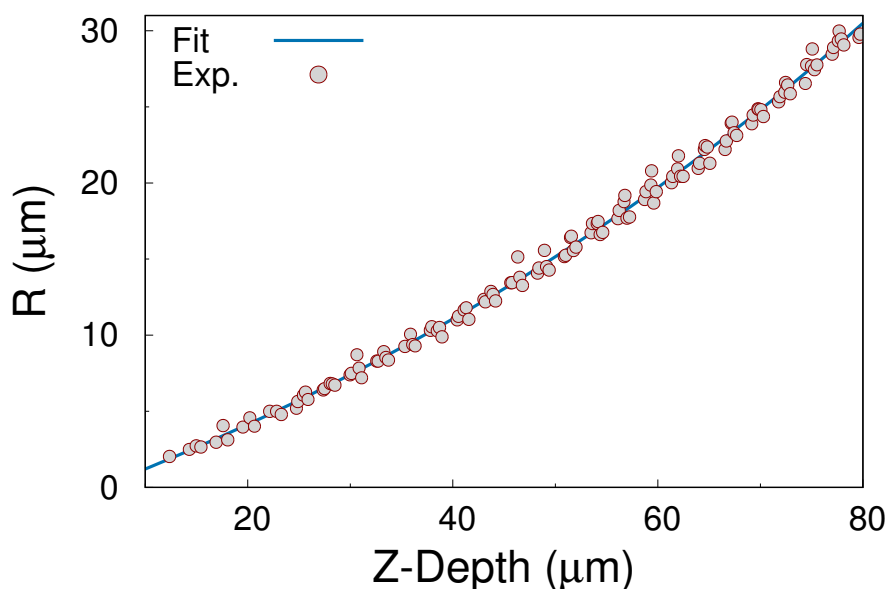


Figure 3.13. Scattered circles are the data collected along 8 manually repetitions, solid curve is the calibration fit to an exponential function $R(z) = -37.50509 + 36.38746 \exp(132.65274/z)$

mixture of particles of 1 and 0.3 microns in a ratio of 1/30 respectively. So far as the WD of the objective is clearly less than in the first calibration the sample

cell used was reduced in height at $\sim 120 \mu\text{m}$ taking into account the cover glass thickness of $\sim 170 \mu\text{m}$ and keeping the design showed in Figure 3.5. The method used to collect the snapshots was started with the focal plane placed inside the microscope slide. Then pictures were taken followed for the stage movement of one step in the z-drive scale, and so on until a well solved image was lost. Each run of collected data could take about 30 frames, then to improve the resolution in the calibration this procedure was repeated at least 8 times more and the data curves were overlapped following the same procedure explained in Section 3.3.2 (collected data was fitted as is shown in Figure 3.13).

In the same way than presented in Section 3.3.2 a script was used to refine the fitted parameters of the bulk diffusion coefficient, in order to test the bulk diffusion in the cell to reach the exponential function with formula here:

$$R(z) = 32.45127516 \exp(z/130.19573008) - 33.71986812. \quad (3.3)$$

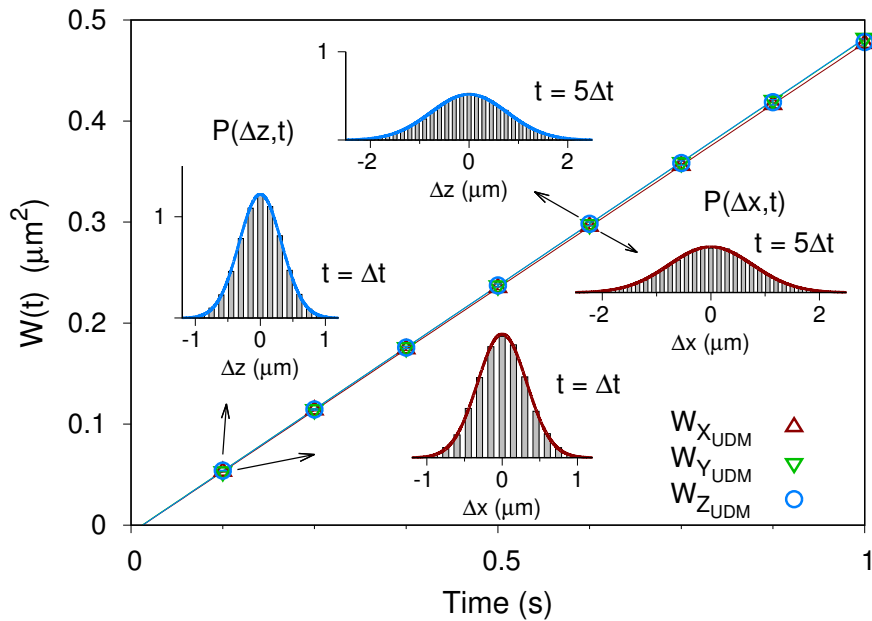


Figure 3.14. MSD of $1 \mu\text{m}$ spheres, which exhibits a linear behavior and consistency of all directions (x,y,z). Some probability distributions are also plotted at two diffusive times $t = \Delta t$ and $t = 5\Delta t$.

We used as before the MSD shown in Figure 3.14 to test the protocol. The plot shows that it is pretty clear that all directions get a good correspondence and that the Gaussian distributions of the linear displacements in both directions, parallel and perpendicular respect to the focal plane as well. The diffusion for each component of the MSD which is proportional to the slope was estimated

showing consistence between them giving a self-diffusion coefficient in average of $D_s = 0.488 \pm 0.001 \mu\text{m}^2/\text{s}$, measured at temperature of 24 ± 1 °C. It is worth to notice that the data was collected from 37 paths of 1500 steps each with temporal steps of $\Delta t = 0.125$ s.

3.5 Particle detection method

In contrast, with previous works in our laboratory [1] or with the experiments carried out by B. Arenas [22], we used here a new homemade Matlab script based on the work given by J. Crocker and D. Grier [17]. In this section we present how to use this software, describing briefly its graphical user interface.

3.5.1 Brief Matlab Graphical User Interface (GUI) Description

Our aim was to go one step further in the digital detection analysis input, with initial location of a particle in the very first image just picking it, following we can select the ring of the diffraction pattern (a considerable reduction in the calculation time for a new position of the tracked particle for the next frame). One important improvement is the patterns bank, which supports the detection of the particle's center. This back up is filled before to start the whole detection process. In this way particle brightness profiles are stored to enhance the detection on each frame looking just particles that corresponds at those patterns in a minimum threshold set by the user.

The OSSM main window

This software (keeping the meaning given by Park *et al.* [21] of Optical Serial Sectioning Microscopy (OSSM)) calls the images sorted, and each name gets counter filled with zeros. The main window runs using the GUIDE tool in Matlab (file called "OSSM.fig"). Figure 3.15 shows the main steps after loading a sequence of images: step 1 is to open the first image in the main directory of the sequence, then it recognizes the sequence with the counter and its default 'tif' extension.

In the highlighted circle 2, we find the main directory name where the sequence was taken, circle 3 is the button to activate the free selection on the image. After pressed, it is possible to pick the particle's center and then its ring, giving this green highlighted stroke on the image. If a particle is recognized and its ring is well defined, a pop up window shows up (Figure 3.16 presents a successful fit upon the brightness profile and the information is showed in pixels).

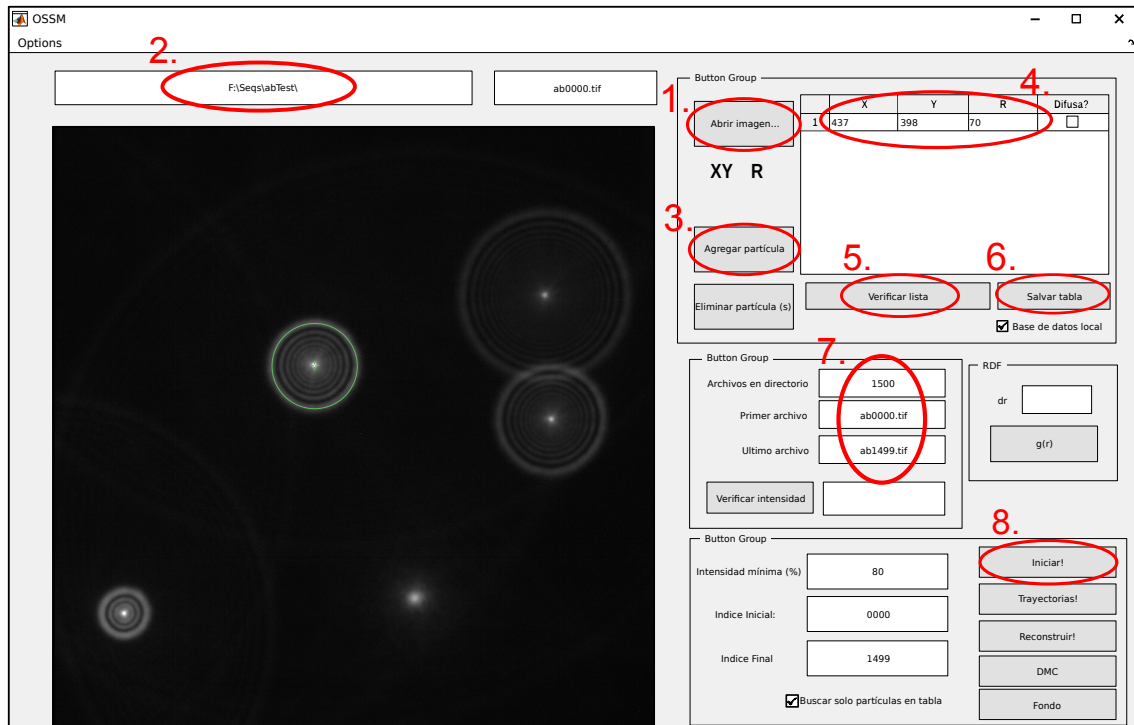


Figure 3.15. The main window for the OSSM interface. Some functionalities are highlighted and explained in the text.

In the table shown in circle 4, coordinates of the particles will be listed. For now the radius is given in pixels as the third coordinate, as well as the xy coordinates in pixels. After the particles of the first image were listed, then the button in circle 5 should be pressed to look for particles patterns not stored yet in the patterns back up. If there is just one particle in frame, a new pop up window will ask if the user wants to add the pattern of this single particle, then it is enough to start processing the sequence. Then as the button in circle 6 is pressed the list of the all particles' coordinates would be saved in an auxiliary file which will subsequently load. In circle 7 some information about the sequence, like frames amount and name of the first file, are found. Finally, circle 8 shows the start button which runs in sequence 4 scripts: the first one will scan the images and identifies the brightness spots by correlation with the patterns in the bank; a second script sorts the data generated by the first script; a third script will make refinements in the data looking for some issues in detection, and finally the forth script will take the data in pixels and converts it in microns, giving also preliminary calculations about the MSD for each trajectory.

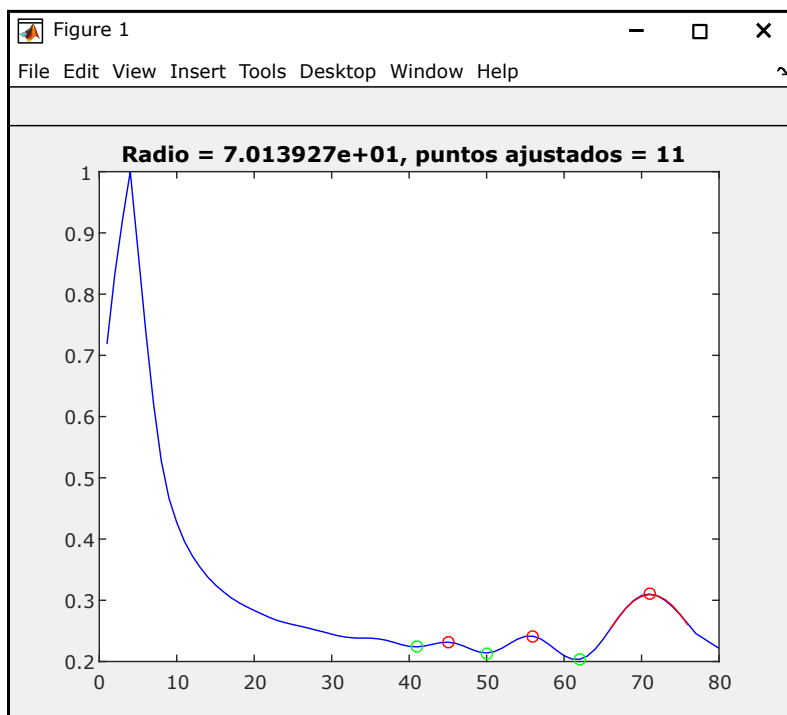


Figure 3.16. While a particle and its outer most ring is picked, this window emerges. Solid line shows the angular mean of the diffraction pattern smoothing the profile. Circles are local minima and maxima found by the fit. The outer ring is taken as the highest fitted maximum. In this plot the intensity over y axis was normalized and the radius over the x axis is provided in pixels (for this fit, the ring radius is 70.139 pixels).

Diffraction pattern tools

Another improvement in the software is that the user can feed a pattern bank loaded along the process. Once the particles were listed the user can run the pattern tools from the main window in the 'Options' at the OSSM window (Figure 3.15). Through this window (Figure 3.17) called "Patterns tool" the user can import two reference patterns (the lowest and highest in brightness) automatically (circle 1) or select them (circle 2). The reference patterns are used as the extremes of the interpolation with the steps set by the user (circle 3). Finally, the reference patterns and the interpolated ones are saved with the button in circle 4 into a folder called "Patterns" located at the image sequence directory.

Advanced settings

Into the 'options' menu, one can find 'settings' alternative which shows up some text zones where the user can change conditions in the limits of the detection. This advanced options (Figure 3.18) are: option 1 will set the cluster radius size,

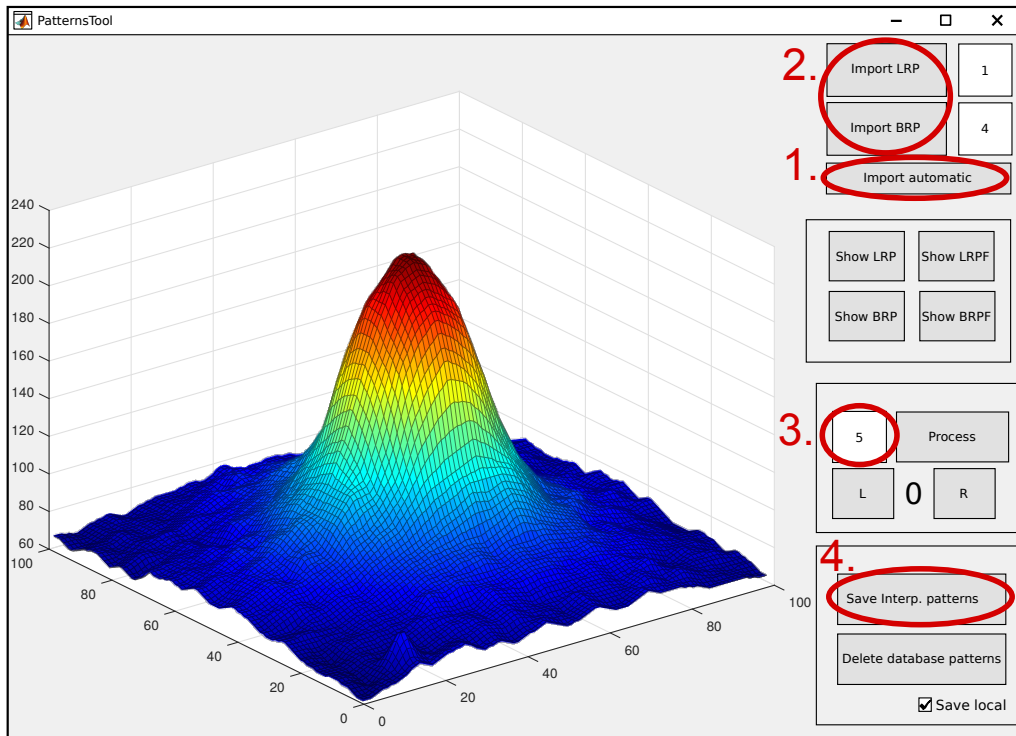


Figure 3.17. The pattern tools window.

it means the lowest square used to contain the particle image (in multiple tests, the best choice was set to 12 pixels getting a square of 25x25 pixels). This number should not be changed. Option 2 will set how high at least would be the bright

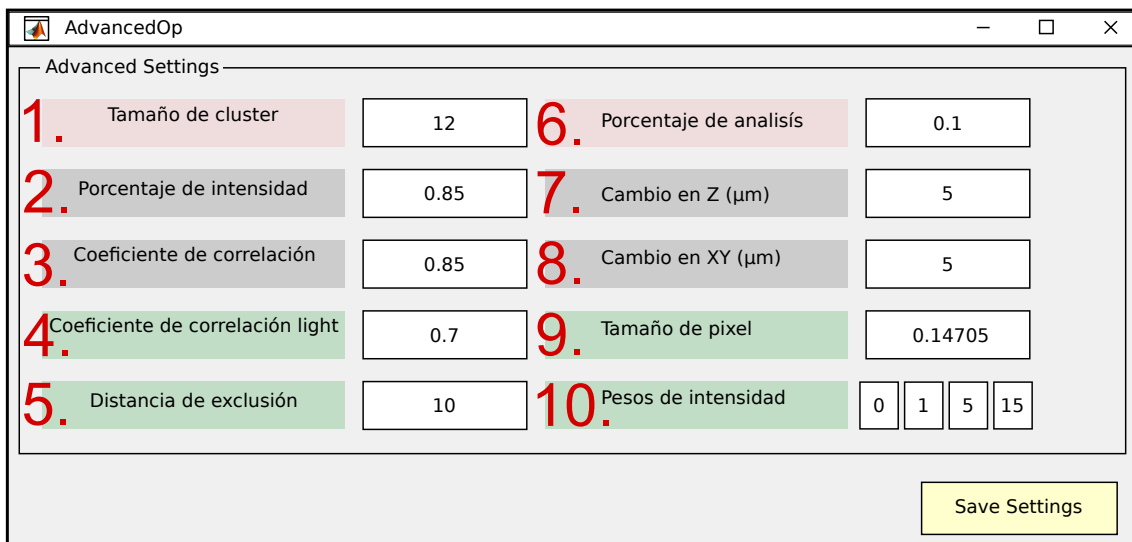


Figure 3.18. Tool what would help the user to tune up the parameters involved in particles tracking (see text).

peak of a particle candidate to be selected. In number 3 there is a correlation

coefficient between a pattern in the bank against the candidate particle and this parameter would be taken into account in the 'Cluster.m' subroutine that will be explained later. The parameter number 4 is the same parameter than 3, however this parameter is slightly set lower for a new process in routine 'rePaths.m'. The option 5 is changed depending on the camera speed. This number says how far should go the tracking gone between frames to look for the new particle location. If the camera speed is slow then this number should be large, also if the viscosity of the media is large, then this number will be short. Number 6 is used in 'Paths.m' subroutine and this is a number that can go from 0 to 1 giving a minimum percentage of steps solved for a particle on the total amount of images (upper values make the process to retry racking the particle in the whole sequence). In 7 and 8, it is possible to set the minimum value that a particle can accede in each direction in microns. If there is a step in the process between the frames that goes far, the tracking would lose the particle for the next step.

In cases the set up is changed, either microscope or objective, then the pixel size under the geometry of observation would change. Here 9 set the pixel size. In the number 10, an array is set to provide weights at the brightness peak that represents a particle, from the background to the peak. It means that zero is given to the base of the bright cone, and the top will have the highest number, as it will be explained in the 'Clusters.m' routine, these numbers are used to define the particle's center of mass.

3.5.2 Image processing

This section introduces the image processing software. Its subroutines are called in order of execution: 'Clusters.m', 'Paths.m', 'rePaths.m', and 'Result.m'.

The routine: Clusters.m

This is the biggest part of the particle detection routine. After the button in circle 8 (Figure 3.15) is pressed this part will run first looking for the particles listed in the table. Thus, it identifies the xy coordinates as particle candidates, extracting a square of 25 pixels side here, it goes over the pixels making clusters with the pixels that represent the particle's image. For example a spot which appears like two hemispherical pieces. Afterward, the image will be enhanced to an image of 100 pixels side improving the location of the center in a quarter of a pixel. Figure 3.19 shows the extracted raw image of 25 pixels side and its respective enhanced image of 100 pixels side.

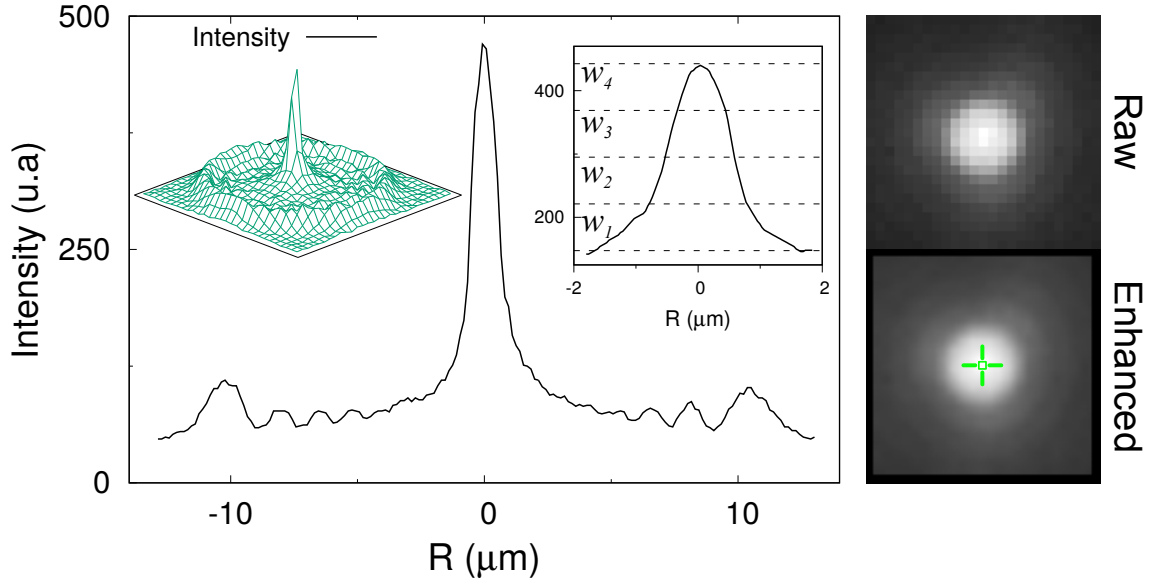


Figure 3.19. From the image a full rings pattern is extracted as in the left inset, its raw profile is drawn in the main plot where is clear the particle peak and the rings profile as a peak sequence ending in the latest ring which is the brightest. At the right side the raw image extracting of 25×25 pixels in the particle location, this image is enhanced as image below where the center is located by using the weighted segmentation showed in the right inset.

The weights assigned are taken from the values given in the array set in the advanced settings showed in Figure 3.18 (number 10). So far as the brightness spot is extracted from the image where the profile gives information about the lowest and the highest intensity in the area, then it is segmented in four parts. The right inset of Figure 3.19 shows the particle profile and the segmentation, weights and segmentation are used in the center of mass determination. The formulation of the center of mass as given in reference [93]:

$$x_{cm} = \frac{\sum_i \sum_j w_j x_i}{\sum_j w_j n_j}, \quad y_{cm} = \frac{\sum_i \sum_j w_j y_i}{\sum_j w_j n_j}, \quad (3.4)$$

where x and y represent the pixel coordinates indexed by i which scan all pixels of the image, and w_j is the assigned value of the weight, j scans each segmented step. After several tests, the zero value was taken for the background intensity so they do not participate to the sum. Later these coordinates would be refined by the correlation of the patterns from the bank with the particle tested. In this way, the location achieves a resolution of $1/8$ pixel for the center of mass location.

On the other hand the ring size estimation comes from the angular mean of the profile in the same shown in Figure 3.16. This brightness profile would show

an iterated fitting on each ring taking the outer maximum of the diffraction pattern as the brightest ring. It is worth to note that if in any case, the outer ring has a maximum which is lower than the ring before this fit would be discarded losing the particle localization. This routine finishes saving in the 'Particles' folder, the files for the images of the sequence, the data of the xy coordinates and radius (columns) is saved in pixels for the each particle in frame (rows) without any specific order.

The routine: Paths.m

This short script will assemble the coordinates giving separated files for each particle. These coordinates are sorted minimizing the distance between steps, and coordinates in pixels. This routine can be called individually from the button



Figure 3.20. Main window of the user interface can be individually executed, numbered: (1) for 'Paths.m', (2) for 'rePaths.m', and (3) for 'Result.m'.

number 1 in Figure 3.20.

The routine: rePaths.m

This script concerns particle tracking. It works with parameters given in the advanced options. With a lower correlation coefficient, there are some brightness losses then it can retrieve the path of the colloid. Finally, this script can receive extra information to fix incomplete paths, once the whole process finished then by manual inspection of the frame where the issue appeared. The user can input the information picking on the image again via GUI. Figure 3.20 number 2, calls just this routine to fix issues and it adds the new information at the reprocessing step.

The routine: Result.m

The last part is the 'Result.m' script which calculates taking the 'reParticula-xx.dat' files into the '[INT-END] reParticula-xx.dat' files where they finally would find the coordinates xyz in microns and the indexation INT that concerns the first frame solved along the sequence. The indexation END is the last frame solved along the sequence. This script could be run independently by using of the button number 3 in Figure 3.20. In addition, this script determines the MSD for each path in the sequence.

4 Data Analysis

4.1 Brownian motion near a water-air interface

We confined colloidal suspension keeping the water-air interface as was described at section (3.1.1). The observations were carried out for around 3 hours. The focal plane was located at $280 \mu\text{m}$ below the cover glass wall into the suspension, over the free interface formed by the hole of 7 mm (Figure 3.3). The distance from the interface to the coverslip was of $\sim 320 \mu\text{m}$. The distance from the focal plane to the interface is at least $30 \mu\text{m}$ of space for the particles' movement observation. The diluted suspension allowed us to find scenarios with around 4 particles at the interface and particles around with enough separation to be considered without interactions.

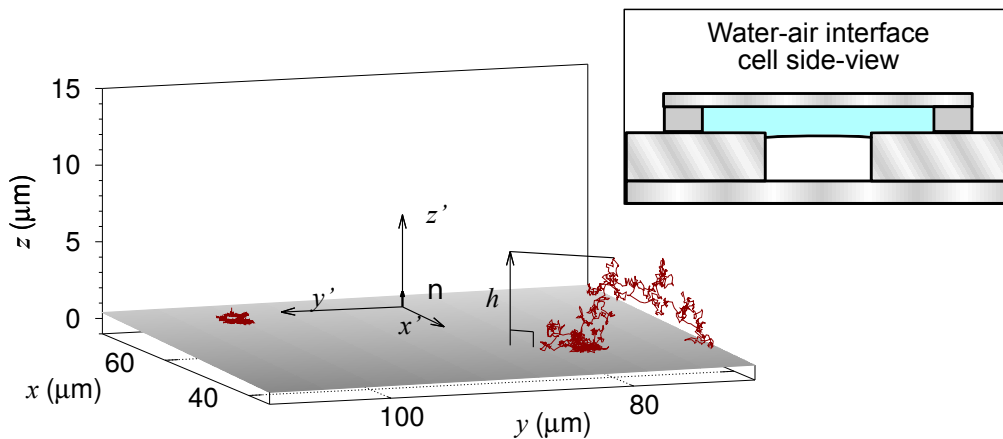


Figure 4.1. Reconstructed paths for two particles close to the water-air interface. One of the particle is on the interface, while the other one is going around over the interface. The top sketch reminds the free interface location in the sample cell.

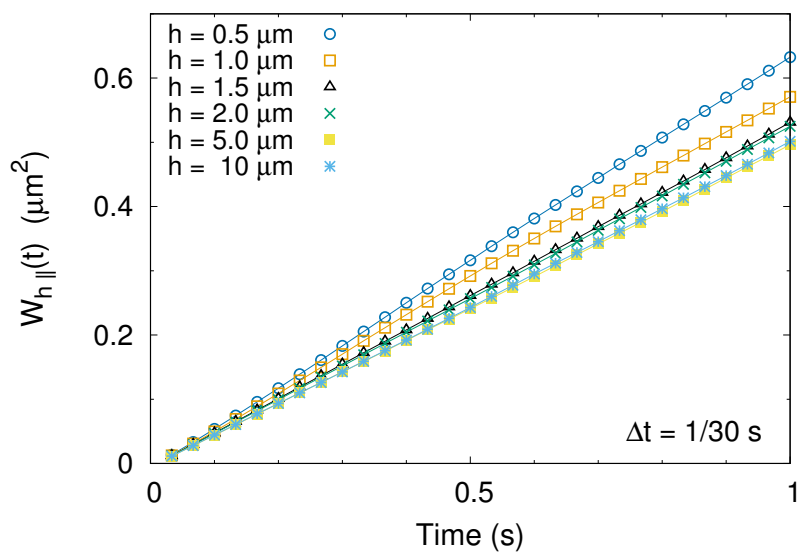


Figure 4.2. Parallel MSD for a particle near a water-air interface at different heights.

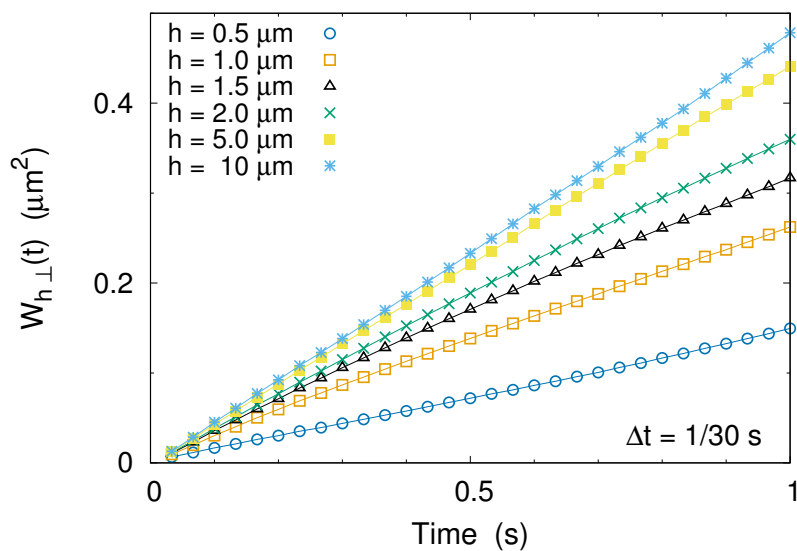


Figure 4.3. Perpendicular MSD for a particle near a water-air interface at different heights.

We took advantage of the particles that reached the interface to solve the interface location using an analytic representation of the interface from a fit plane. From this plane we set a frame to locate the rest of the particles in frame. The plane defined shows a very small inclination close to the hole center, afterward we fit a geometric plane of the form $b_1x + b_2y + b_3z + b_4 = 0$, where the coefficients b_j ($j = 1, \dots, 4$) come from the least square regression. Before to systematically apply the fit, we tested the approximation showing consistence with the measurements. The coordinates of the particles over the plane were projected according to a plane rotation defined by the Euler's angles [94], in this way we used the reference respect to the rotated plane (see Figure 4.1).

The experimental data from more than 800 paths of 1500 steps each, measured over more than 10 samples, were analyzed from the particles positions which were accumulated along bins representing the height on z direction. On each bin the data was added every time that the colloid passes in the bin interval. From the data collected in each bin we performed a sum of squared displacement over the events number in the bin. Simultaneously variations were accumulated to determine the standard deviation of the data distribution, determining in this way the MSD for each distance h from the interface, and its respective statistical error. The MSD at different values of h were plotted in Figure 4.2 for the parallel direction along the interface and in Figure 4.3 for perpendicular direction.

The linear behavior exhibited by the MSD with time indicates that particles satisfy Brownian motion and the diffusion is only modified by the hydrodynamics depending on the distance to the interface. Concluding that, the particle movement produces a perturbation which is transferred by the fluid toward the interface, and then reflected back to the particle, such perturbation comes from thermal excitation. For parallel direction, it is pretty clear that diffusion increases as the particle gets close to the interface. In contrast, diffusion for perpendicular direction decreases as the particle goes to the plane.

Moreover, diffusion splits along each direction in respect to the interface orientation. They are compared with several theoretical models provide by the equations for a free interface following the Perkins and Jones' model Eq. (2.24) and Eq. (2.25) represented in Figures 4.5 and 4.4 with dashed lines for each diffusive direction (T-PJS). The model from Lee *et al.* for a liquid-liquid interface was applied to compute the theoretical curves, using the experimental settings $\eta_2 = 0.8324$ mPa·s the water viscosity, and $\eta_1 = 0.02$ mPa·s for air viscosity, both at 28°C. Leading a viscosity ratio $\lambda = 0.024027$ plotted with light-gray solid lines (T-LL) for Eq. (2.28) and Eq. (2.29). We also plotted the proposed model (Eq.

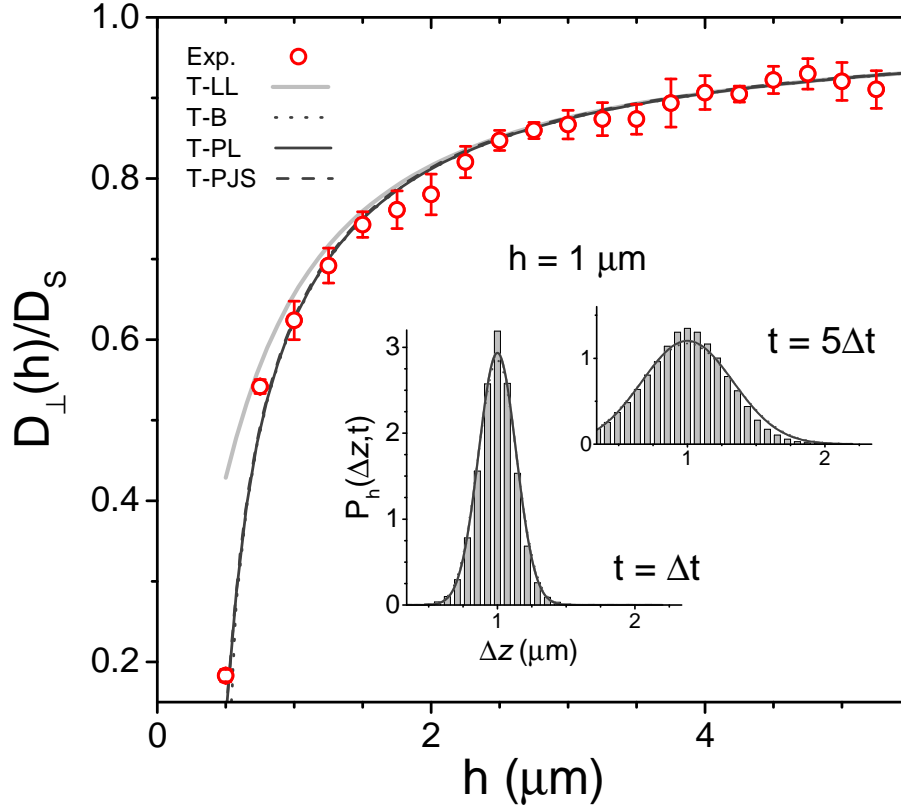


Figure 4.4. Spherical colloids' diffusion close to a water-air interface in perpendicular direction.

(2.30 and Eq. (2.31)) with solid dark-gray lines (T-PL). In addition, we drew the Bart's model for liquid-liquid interface in perpendicular direction with spaced dots (T-B) [57], using the same ratio λ and also the hard wall normalized diffusion in parallel direction from Perkins and Jones (T-PJH), Eq. (2.26).

The perpendicular normalized diffusion data plotted in Figure 4.4 using circles, show the expected hindered diffusion as predicted by the models close to the interface. We notice that Lee's second order model is in good agreement with the observed data. Also, the probability distributions functions (PDFs), included in the inset for two times $t = \Delta t$ and $t = 5\Delta t$, confirm that Brownian motion conditions are satisfied at small distances of the interface. Otherwise, for a spherical probe close to a hard wall as was explained in Sec. (1.1), where the PDF became asymmetric due to the wall presence limiting the accessible space to explore, for a soft interface the PDFs show that the particles can softly deform the interface. Solid lines for the distributions where correctly fitted to theoretical Gaussian distributions (Eq. (2.8)) and are evaluated for the current height h and the diffusion coefficient depend of h .

To clarify which of the models have a better agreement with the experimen-

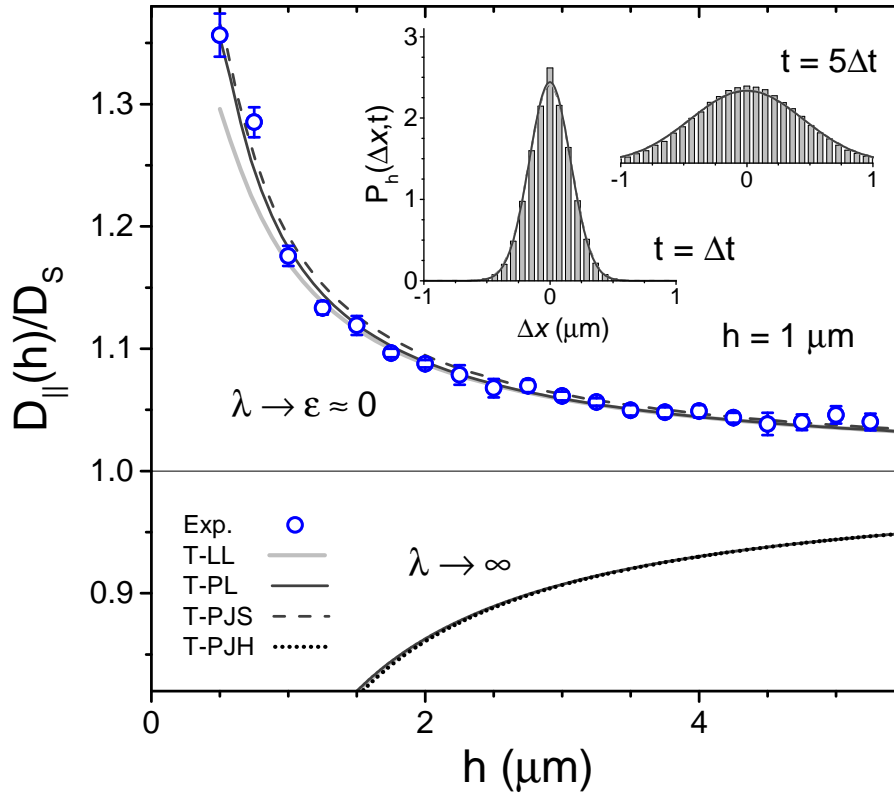


Figure 4.5. Spherical colloids' diffusion close to a water-air interface in parallel direction.

tal data, we used the coefficient of determination (COD) regularly applied to quantify the goodness of a fit for the least regression method [95]. Defined as $R^2 = 1 - (\sum_i w_i (y_i - f(x_i))^2) / (\sum_i w_i (y_i - \bar{y})^2)$ where y_i are the experimental data, the direct weights w_i are the uncertainties, $\bar{y} = \sum_i y_i$, and the theoretical function to test is $f(x_i)$. The value of R^2 transit from 0 to 1, indicating how close are dispersed data to a known function (assigning 1 for a perfect match). The values calculated of R^2 for each model of the perpendicular diffusion data are: 0.913 (T-LL), 0.983 (T-PJS), 0.983 (T-B), and 0.984 (T-PL). These values show a better agreement with the models (T-PJS), (T-B), and (T-PL).

In the case of the parallel diffusion to the soft interface, it is clear that as the colloid reaches the interface its diffusion has an opposite behavior than for perpendicular direction (Figure 4.5). Since, the perpendicular movement is hindered by the interface as it goes there finding front mechanical waves coming back. The liquid along the interface can enhance the particles parallel diffusion by the nearly absence of a drag force at the interface. Theoretical predictions tested also with the COD finding: the R^2 0.990 (T-PJS), 0.936 (T-LL), and 0.990 (T-PL) for each model. Indicating that the theoretical models are in good agree-

ment with a better accordance for (T-PJS) and (T-PL). We can notice that exists a small difference between the free interface model and the fluid-fluid model for water-air, which indicates a negligible drag force at the interface.

We included below the hard wall theoretical parallel diffusion prediction (T-PJH) (Figure 4.5) that can be compared in the limit $\lambda \rightarrow \infty$ which leads to the models (T-LL) and (T-PL) for hard wall case, in such good agreement. Here it is important to emphasize that models (T-LL) and (T-PL) can be used for different systems depending on the parameter λ and run continuously. However, the (T-LL) model lacks in accuracy to reproduce the data for low values of λ . The inset in Figure 4.5 shows PDF functions for the data collected in the bin corresponding at a distance $h = 1 \mu\text{m}$ for two times $t = \Delta t$ and $t = 5\Delta t$, exhibiting nothing unusual along the interface where the probe particle can move freely, keeping a Brownian like motion.

4.2 Brownian motion near a hydrophobic hard wall

The hydrophobic monolayer interface was studied from 95 paths of 1500 steps obtained in a cell of $\sim 320 \mu\text{m}$ of height keeping the design showed in Figure 3.5. Therefore, the focal plane was placed $280 \mu\text{m}$ into the suspension ($\Delta t = 33.33$ ms). A glass slide with a micrometric roughness on the surface was silanized, following the protocol explained in Sec. (3.1.1) (looking to reach a superhydrophobic surface, we also tried n-hexatriacontane layer on the surface finding short-time stability for the monolayer [96–99]).

Samples silanized showed no effective particle sticking on the cell bottom, instead they kept movement at neighborhoods of the hydrophobic interface. Inset in Figure 4.6 shows a particle path close to the bottom while the colloid moves around in quasi 2D. Normalized diffusion are plotted (Figure 4.6) showing that the hydrodynamic interactions are preserved over the interaction between the particle and the hydrophobic monolayer. Solid line is the theoretical Eq. (2.26) and the dashed line theoretical Eq. (2.20), symbols the experimental data.

4.3 Particle movement near solid supported membranes

This section presents results for the systems: sphere going to a planar solid supported membranes deposited by spincoating for two different phospholipids,

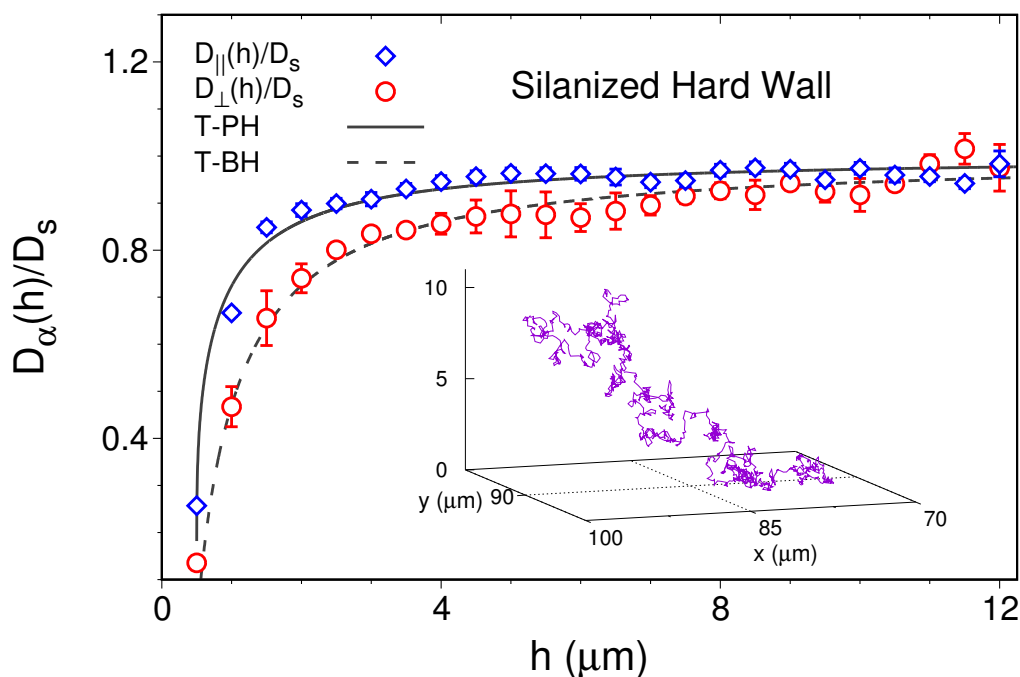


Figure 4.6. Normalized diffusion as a function of the height for colloids of $1 \mu\text{m}$ dispersed in ultrapurified water with NaCl at 10 mM. Particle's trajectory at the ground level; the hydrophobic monolayer avoids that the particle sticks on the surface.

DMPC and DOPC. The third study is about a particle going to a planar hydrophobic interface. It is important to emphasize that the osmotic stressor polymer used to increase the osmotic pressure in the solvent, giving stability to the membrane so it does not detach to the volume, PEG 20 kD was tested in different concentrations 0.2%, 0.5%, 1.5%, 3.6%, 5.8%, and 9.0% [100]. Finding that the concentration of 3.6% allows a clear Brownian motion for micrometric polystyrene beads and stability to the membrane that stay on the solid interface.

Bulk measurements for particles immersed in water-PEG 3.6% were conducted using sample cells of $600 \mu\text{m}$ of thickness (see Figure 3.5), and the focal plane was placed at $70 \mu\text{m}$ below the cover glass wall, having an observation field that can track particles at least $60 \mu\text{m}$ below the focal plane and far from the cell walls. In such conditions colloids were quite diluted ($400 \text{ colloids}/\mu\text{l}$). Figure 4.7 shows the MSD for 97 paths of 1500 frames with time intervals of $\Delta t = 125 \text{ ms}$. Here the self-diffusion obtained was $D_s^{3.6} = 0.143 \pm 0.001 \mu\text{m}^2/\text{s}$ at $25 \pm 1^\circ\text{C}$.

The inset (bottom) shows MSD until $t = 1.0 \text{ s}$. MSD for all directions is presented with symbols ($W_x(t)$ (Δ), $W_y(t)$ (∇), and $W_z(t)$ (\circ)) in logarithmic scale of both axis showing that the polymer does not change the linear viscous proper-

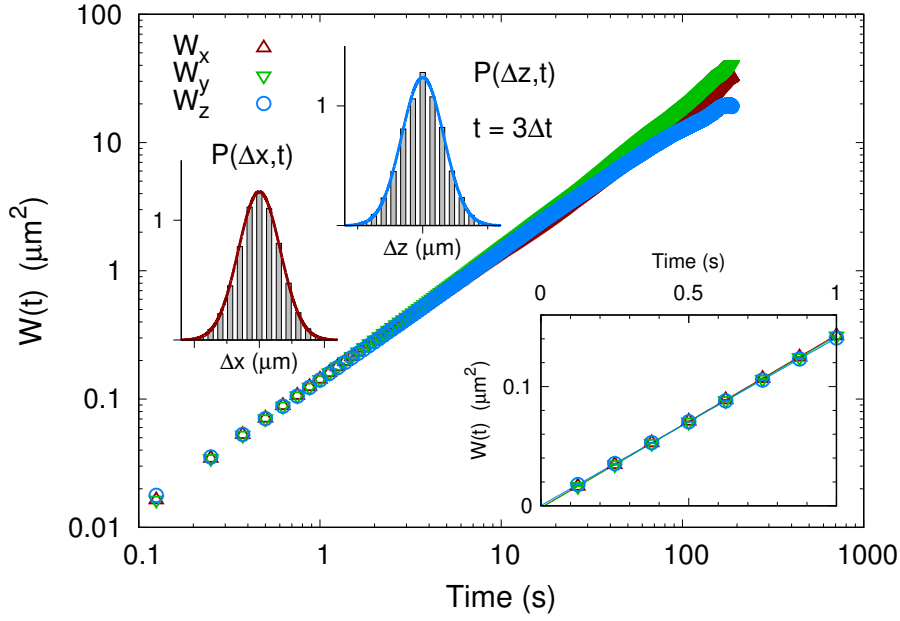


Figure 4.7. Mean square displacement for a diluted colloidal suspension of $1 \mu\text{m}$ in bulk conditions. The aqueous solvent has PEG 20k at 3.6% w/w concentration.

ties of the fluid. Displacement distribution for xy and z directions are shown in Figure 4.7, according to a Gaussian distribution (top), solid lines represents the theoretical probability distribution function for $t = 3\Delta t = 375 \text{ ms}$ (Eq. 2.8).

We performed experiments concerning to probe that the rigid wall conditions are correctly reproduced for the microscopy in UDM finding well agreement for a rigid wall. Then we prepared the set up to conduct experiment with a hard wall for a dispersion in water-PEG 3.6%, obtaining no extra effects to the hydrodynamics out coming from the polymer presence. We also verified the scales for suspension with PEG 3.6% considering the relative density $\rho_{peg}^{3.6}/\rho_w = 1.005$, and viscosity $\eta_{peg}^{3.6} = 3.235 \text{ mPa}\cdot\text{s}$, at 20°C [101], finding an inertia-relaxation time $\tau_v = 1.80 \times 10^{-8} \text{ s}$, terminal velocity $v_T = 7.50 \times 10^{-9} \text{ m/s}$ leading a Reynolds number $Re = 2.33 \times 10^{-9}$, a Péclet number $Pe = 0.056$ and Debye length $\kappa^{-1} = 3.00 \text{ nm}$ (dielectric constant $\epsilon \approx 78$ [102]), confirming good conditions for diffusive conditions. In this way, allowing us to proceed with the measurements of the interaction of colloids with phospholipids membranes.

We used sample cells with DMPC membrane prepared following the same protocol (described in Sec.(3.1.2)). The cell height set at $\sim 120 \mu\text{m}$ and the focal plane location at $70 \mu\text{m}$ into the suspension. We found that during the observations particles on the membrane do not stick to the surface at $20 \pm 1^\circ\text{C}$, conserving movement from the collision with the solvent molecules. Figure 4.8 shows

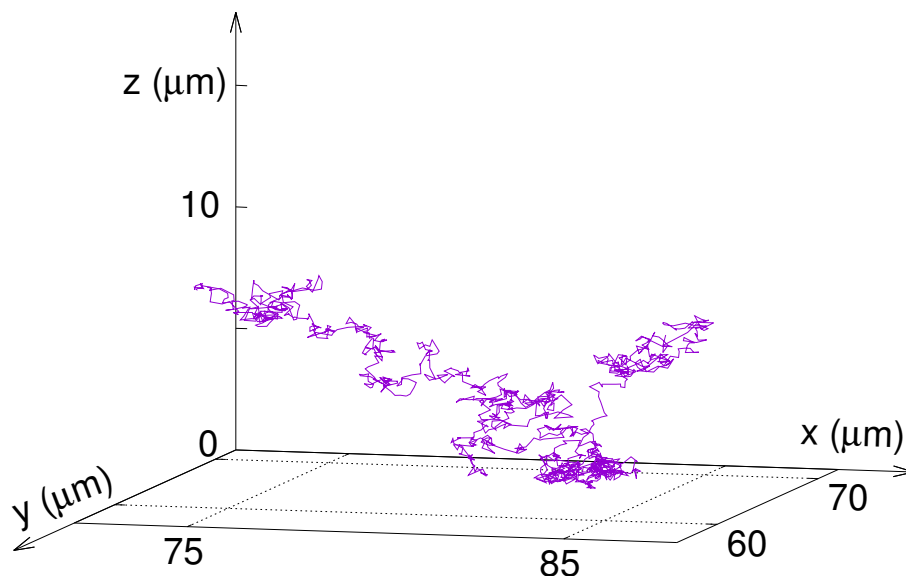


Figure 4.8. Trajectory of a sphere of diameter $1 \mu\text{m}$ going toward a DMPC bilayer stack. The flat membrane rests along the plane $z = 0$ in phase L_β at $20 \pm 1^\circ\text{C}$. The aqueous solvent has PEG 20k at 3.6%.

a colloid path close to a surface covered with a stack of DMPC bilayers where the particle reaches the bottom and then goes back to the solvent. Opening the possibility of very low van der Waals interaction between the colloid and the membrane that acts as an “anti-fouling” barrier.

Diffusion depending upon the height are plotted in Figure 4.9 for 111 paths of 1500 steps each of time-steps of $\Delta t = 125 \text{ ms}$, showing qualitative consistence with hard wall hydrodynamic interactions. Solid line correspond to the model presented by Brenner for perpendicular diffusion Eq. (2.20) and dashed line for Perkins and Jones model for parallel diffusion Eq. (2.26). Triangles (Δ) are the experimental computation of the normalized perpendicular diffusion, on the other hand circles (\circ) are the experimental data of the normalized parallel diffusion. The corresponding displacement distribution along each direction (insets) are compared with the theoretical Gaussian distribution Eq. (2.8) at $h = 1 \mu\text{m}$ for the time $t = 3\Delta t$ showing a classical Brownian motion behavior. Moreover, histogram bars are more spread for the distribution $P_h(\Delta z, t)$, matching with the situation of particles that do not stick to the top membrane surface.

The samples with DOPC membranes were measured collecting 119 paths of 1500 time-steps each at temperature $21 \pm 1^\circ\text{C}$. Diffusion as a function of the height is shown in Figure 4.10 and compared with the theoretical models perpendicular Eq. (2.20) (solid line) and parallel with Eq. (2.26) (dashed line). Showing consistency with the experimental data in perpendicular (\diamond) and parallel (\circ) diffusion.

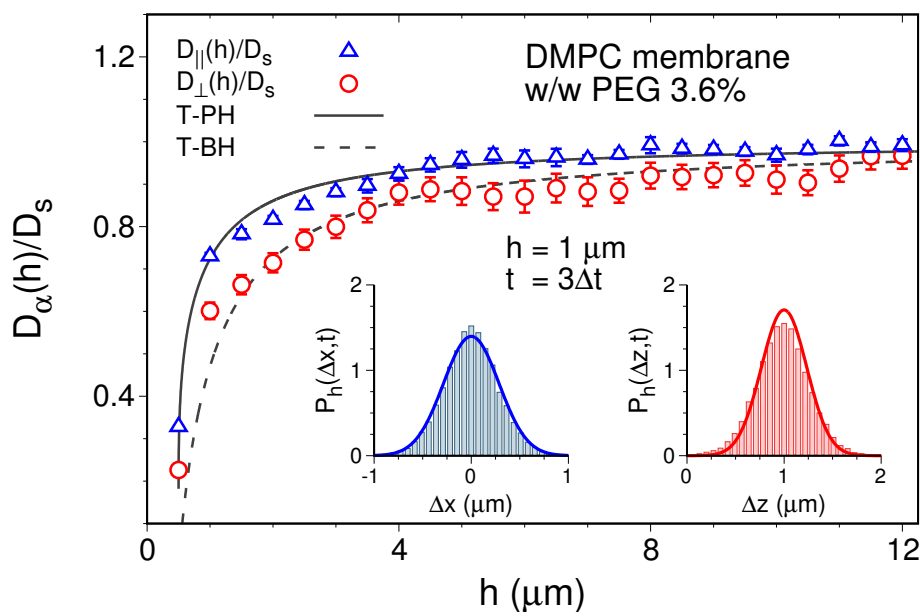


Figure 4.9. Diffusion of spherical colloids of $1 \mu\text{m}$ close to a thin solid supported stack of DMPC membrane at $20 \pm 1^\circ\text{C}$. The histograms have the information of the displacements at the bin $h = 1 \mu\text{m}$, for $t = 3\Delta t$.

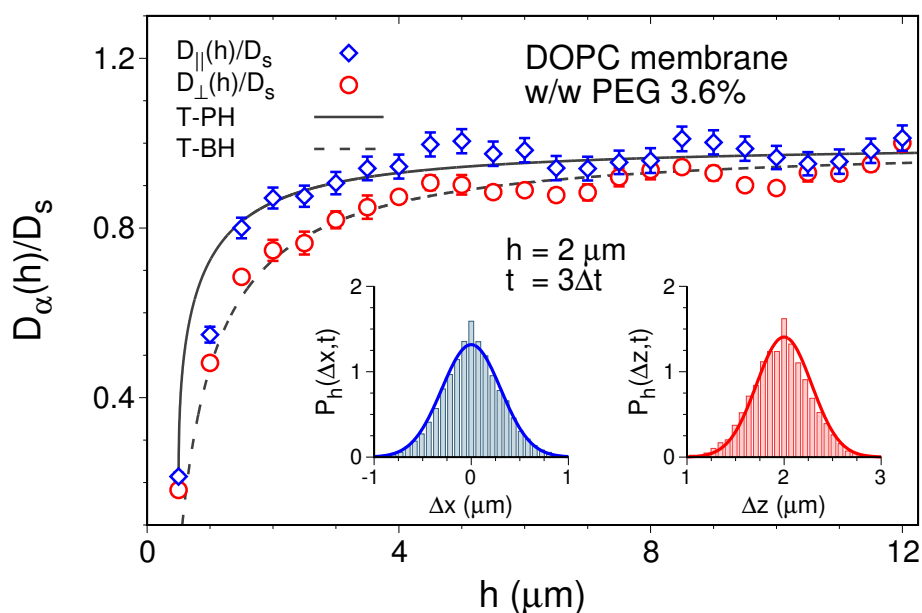


Figure 4.10. Diffusion of spherical colloids of $1 \mu\text{m}$ close to a thin solid supported stack of DOPC membrane at $21 \pm 1^\circ\text{C}$. The histograms have the information of the displacements at the bin $h = 2 \mu\text{m}$, for $t = 3\Delta t$.

In this case the histograms show Brownian motion at $h = 2 \mu\text{m}$, although distributions are affected for an additional condition, which could be a non-regular membrane deposition changing the movement behavior in both directions.

Here is important to notice that for both cases the membrane fluctuations are on the order of tens angstroms. Whereby, the membrane fluctuations are damped because of the substrate presence, giving a scale quite small compared with the colloid diameter. According to Ref. [85], if the particle size is much longer than the membrane fluctuation, then we should expect that the membrane stack do not produce a perturbation large enough to over pass the hydrodynamic interaction of a hard wall.

According with Mannicke and Salditt [91] the spin coating method can produce a stack of a few bilayers, whether if the phospholipids are DMPC or DOPC. Fluctuations for a DMPC stack was studied for Constantine *et al.* [103], where the authors found for similar conditions to our experiments a correlation length of $\varepsilon \sim 20 - 40 \text{ \AA}$, for a spacing of $d \sim 30 - 60 \text{ \AA}$. Such values corresponded for stacks of 16 to 21 bilayers, in this case is clear that the particle radius is much greater than the correlation length, ensuring that the hard wall hydrodynamics over pass the membrane fluctuations. Concerning to the DOPC bilayer stack, some measurements were reported by H.I. Petrache *et al.* [104] where the d -spaced bilayer stacks ($d \sim 50 - 65 \text{ \AA}$) can reach an interlamellar fluctuation of $\sigma \sim 2 - 7 \text{ \AA}$, giving a sense of the small order of the fluctuations.

Conclusions

In this work we studied the diffusion of spherical colloidal particles of $1\ \mu\text{m}$ in diameter approaching different interfaces using three dimensional digital video microscopy (3D-DVM). Among main conclusions:

- The hydrodynamic interaction measured through the translational friction component for a water-air interface shows good agreement with the theoretical models presented along the work. Comparison of the theoretical predictions with the experimental data that we measured, shows low effects of the viscosity ratio λ , which is the relation between the media in contact through the viscosities $\lambda = \eta_1/\eta_2$ (the extreme values; $\lambda \rightarrow 0$ corresponds to a free interface, and $\lambda \rightarrow \infty$ to a hard wall).
- We proposed also a theoretical model based on a free interface model and a liquid-liquid interface approximated model, finding a good agreement with the experimental data. Such model can be tuned by the variation of the parameter λ passing continuously from the rigid wall (water-solid interface) case to the free interface (water-air).
- Parallel diffusion for a spherical colloid close to a water-air interface is enhanced, because of the absence of drag force along the interface. The liquid in contact with the air flows faster than the liquid in bulk, then a colloid is transported longer along the boundary. The drag force arises from the fluid layers in contact dissipating the energy of the flow, in the case of a free boundary the air do not dissipate the energy as the continuous media does.
- Perpendicular diffusion is hindered by the acting hydrodynamic waves generated by the colloids Brownian motion that come back from the interface to the particles, affecting the colloid diffusion.

- A hydrophobic wall also exhibit a close-to-wall repulsion, then the colloid showed movement close to the wall, although so far to effective enhanced diffusion.
- For the solid supported membrane of DMPC we found that colloids at the bottom still moving, although their movement is far enough to consider an enhanced diffusion close to the membrane.
- DOPC solid supported membranes affect the particle Brownian motion up to 2 μm distances over the membrane, suggesting that the membrane does not have a uniformly flat shape.
- The three last cases cited (hydrophobic monolayer, DMPC and DOPC membranes) gave a good agreement with the hard wall model for diffusion of colloids.
- For the particular cases of a membrane deposition, the fluctuations of the bilayer stack have a short length, which is not able to produce a perturbation that can modify the colloid motion. The membrane fluctuations are damped by the presence of the substrate.

Bibliography

- [1] M. D. Carbajal-Tinoco, R. Lopez-Fernandez, and J. L. Arauz-Lara, "Asymmetry in colloidal diffusion near a rigid wall," *Phys. Rev. Lett.*, vol. 99, p. 138303, 2007.
- [2] G. MacKay, M. Suzuki, and S. Mason, "Approach of a solid sphere to a rigid plane interface. part 2," *Journal of Colloid Science*, vol. 18, no. 1, pp. 103 – 104, 1963.
- [3] M. I. M. Feitosa and O. N. Mesquita, "Wall-drag effect on diffusion of colloidal particles near surfaces: A photon correlation study," *Physical Review A*, vol. 44, no. 10, pp. 6677–6685, 1991.
- [4] L. Lobry and N. Ostrowsky, "Diffusion of Brownian particles trapped between two walls: Theory and dynamic-light-scattering measurements," *Physical Review B*, vol. 53, no. 18, pp. 12050–12056, 1996.
- [5] P. Holmqvist, J. K. G. Dhont, and P. R. Lang, "Anisotropy of Brownian motion caused only by hydrodynamic interaction with a wall," *Physical Review E - Statistical, Nonlinear, and Soft Matter Physics*, vol. 74, no. 2, 2006.
- [6] J.-B. Fournier, D. Lacoste, and E. Raphaël, "Fluctuation spectrum of fluid membranes coupled to an elastic meshwork: jump of the effective surface tension at the mesh size.," *Physical review letters*, vol. 92, no. 1, p. 018102, 2004.
- [7] F. Jünger, F. Kohler, A. Meinel, T. Meyer, R. Nitschke, B. Erhard, and A. Rohrbach, "Measuring local viscosities near plasma membranes of living cells with photonic force microscopy," *Biophysical Journal*, vol. 109, no. 5, pp. 869–882, 2015.

-
- [8] C. Peetla, S. Jin, J. Weimer, A. Elegbede, and V. Labhasetwar, “Biomechanics and thermodynamics of nanoparticle interactions with plasma and endosomal membrane lipids in cellular uptake and endosomal escape,” *Langmuir*, vol. 30, no. 25, pp. 7522–7532, 2014.
- [9] M. Daoud, S. Lyle, and C. Williams, *Soft Matter Physics*. Springer Berlin Heidelberg, 2013.
- [10] M. Doi, *Soft Matter Physics*. OUP Oxford, 2013.
- [11] E. Locatelli, M. Pierno, F. Baldovin, E. Orlandini, Y. Tan, and S. Pagliara, “Single-file escape of colloidal particles from microfluidic channels,” *Physical Review Letters*, vol. 117, no. 3, 2016.
- [12] A. Papagiannopoulos, K. Sotiropoulos, and S. Pispas, “Particle tracking microrheology of the power-law viscoelasticity of xanthan solutions,” *Food Hydrocolloids*, vol. 61, pp. 201 – 210, 2016.
- [13] E. Sarmiento-Gómez, J. R. Villanueva-Valencia, S. Herrera-Velarde, J. A. Ruiz-Santoyo, J. Santana-Solano, J. L. Arauz-Lara, and R. Castañeda Priego, “Short-time dynamics of monomers and dimers in quasi-two-dimensional colloidal mixtures,” *Phys. Rev. E*, vol. 94, p. 012608, 2016.
- [14] S. L. Dettmer, S. Pagliara, K. Misiunas, and U. F. Keyser, “Anisotropic diffusion of spherical particles in closely confining microchannels,” *Phys. Rev. E*, vol. 89, p. 062305, 2014.
- [15] K. A. Bailey and Z. D. Schultz, “Tracking bulk and interfacial diffusion using multiplex coherent anti-stokes raman scattering correlation spectroscopy,” *The Journal of Physical Chemistry B*, vol. 120, no. 27, pp. 6819–6828, 2016.
- [16] R. Sarfati and E. R. Dufresne, “Long-range attraction of particles adhered to lipid vesicles,” *Phys. Rev. E*, vol. 94, p. 012604, 2016.
- [17] J. C. Crocker and D. G. Grier, “Methods of digital video microscopy for colloidal studies,” *Journal of Colloid and Interface Science*, vol. 179, no. 1, pp. 298 – 310, 1996.
- [18] J. C. Crocker and D. G. Grier, “When like charges attract: The effects of geometrical confinement on long-range colloidal interactions,” *Phys. Rev. Lett.*, vol. 77, pp. 1897–1900, 1996.

- [19] P. Nakroshis, M. Amoroso, J. Legere, and C. Smith, "Measuring boltzmann's constant using video microscopy of brownian motion," *American Journal of Physics*, vol. 71, no. 6, 2003.
- [20] R. Salmon, C. Robbins, and K. Forinash, "Brownian motion using video capture," *European Journal of Physics*, vol. 23, no. 3, p. 249, 2002.
- [21] J. S. Park, C. K. Choi, and K. D. Kihm, "Temperature measurement for a nanoparticle suspension by detecting the brownian motion using optical serial sectioning microscopy (ossm)," *Measurement Science and Technology*, vol. 16, no. 7, p. 1418, 2005.
- [22] B. L. Arenas-Gómez and M. D. Carbajal-Tinoco, "Brownian motion of a colloidal particle immersed in a polymeric solution near a rigid wall," *Rev. Mex. Fis.*, vol. 60, no. 3, 2014.
- [23] J. C. Benavides-Parra, D. Jacinto-Méndez, G. Brotons, and M. D. Carbajal-Tinoco, "Brownian motion near a liquid-gas interface," *The Journal of Chemical Physics*, vol. 145, no. 11, 2016.
- [24] D. L. J. Vossen, A. van der Horst, M. Dogterom, and A. van Blaaderen, "Optical tweezers and confocal microscopy for simultaneous three-dimensional manipulation and imaging in concentrated colloidal dispersions," *Review of Scientific Instruments*, vol. 75, no. 9, 2004.
- [25] A. Ashkin, "Acceleration and trapping of particles by radiation pressure," *Phys. Rev. Lett.*, vol. 24, pp. 156–159, 1970.
- [26] B. Bouma, *Handbook of Optical Coherence Tomography*. CRC Press, 1st ed., 2001.
- [27] T. Watarai and T. Iwai, "Experimental study on air-liquid interface effect of brownian dynamics using spectral-domain low-coherence dynamic light scattering," *Optical Review*, vol. 21, no. 3, pp. 378–381, 2014.
- [28] D. Li, *Encyclopedia of Microfluidics and Nanofluidics*, vol. 1. Springer, 2008.
- [29] A. Rohrbach, "Observing secretory granules with a multiangle evanescent wave microscope," *Biophysical Journal*, vol. 78, no. 5, pp. 2641 – 2654, 2000.
- [30] K. D. Kihm, A. Banerjee, C. K. Choi, and T. Takagi, "Near-wall hindered brownian diffusion of nanoparticles examined by three-dimensional ratiometric total internal reflection fluorescence microscopy (3-d r-tirfm)," *Experiments in Fluids*, vol. 37, no. 6, pp. 811–824, 2004.

-
- [31] A. Banerjee and K. D. Kihm, “Experimental verification of near-wall hindered diffusion for the brownian motion of nanoparticles using evanescent wave microscopy,” *Phys. Rev. E*, vol. 72, p. 042101, 2005.
- [32] G. M. Wang, R. Prabhakar, and E. M. Sevick, “Hydrodynamic mobility of an optically trapped colloidal particle near fluid-fluid interfaces,” *Phys. Rev. Lett.*, vol. 103, p. 248303, 2009.
- [33] T. Boatwright, M. Dennin, R. Shlomovitz, A. A. Evans, and A. J. Levine, “Probing interfacial dynamics and mechanics using submerged particle microrheology. ii. experiment,” *Physics of Fluids*, vol. 26, no. 7, 2014.
- [34] T. Watarai and T. Iwai, “One-shot measurement of the air-liquid interface effect by a spectral-domain low-coherence dynamic light scattering technique,” vol. 8839, 2013. Conference on Dimensional Optical Metrology and Inspection for Practical Applications II, San Diego, CA, AUG 25-26, 2013.
- [35] H. Faxen, “The movement of a rigid sphere along the axis of a tube filled with viscous liquid,” *Ark. Mat., Astron. Fys.*, vol. 17, no. 27, 1923.
- [36] S. H. Lee, R. S. Chadwick, and L. G. Leal, “Motion of a sphere in the presence of a plane interface. Part 1. An approximate solution by generalization of the method of Lorentz,” *Journal of Fluid Mechanics*, vol. 93, no. 04, p. 705, 1979.
- [37] H. Brenner, “The slow motion of a sphere through a viscous fluid towards a plane surface,” *Chemical Engineering Science*, vol. 16, no. 3–4, pp. 242 – 251, 1961.
- [38] K. Bizheva, A. Siegel, and D. Boas, “Path-length-resolved dynamic light scattering in highly scattering random media: The transition to diffusing wave spectroscopy,” *Physical Review E*, vol. 58, no. 6, pp. 7664–7667, 1998.
- [39] K. Ishii, T. Iwai, and S. Nakamura, “Spectrum of Time-Varying Scattered Light Field,” *America*, vol. 25, no. 3, pp. 718–724, 2008.
- [40] J. Happel and H. Brenner, *Low Reynolds number hydrodynamics with special applications to particulate media; 2nd ed.* Mono. textbooks on mechanics of solids and fluids, Liège: Noordhoff, 1973.
- [41] P. R. Lang, Y. Liu, *et al.*, “Soft matter at aqueous interfaces,” in *Lecture Notes in Physics, Berlin Springer Verlag*, vol. 917, Springer, 2016.

- [42] F. Kreith, *Fluid Mechanics*. Mechanical/Chemical engineering, Taylor & Francis, 1999.
- [43] J. S. L.D. Landau, *Fluid mechanics*, vol. Volume 6 of *Course of theoretical physics* 6. Pergamon Press, 2nd ed., 2nd english ed., rev ed., 1987.
- [44] G. K. Batchelor, *An Introduction to Fluid Dynamics*. Cambridge University Press, 1967.
- [45] W. B. Russel, D. A. Saville, and W. R. Schowalter, *Colloidal Dispersions*. Cambridge: Cambridge University Press, 1989.
- [46] I. W. Hamley, *Introduction to Soft Matter: Synthetic and Biological Self Assembling Materials*. Wiley, 2007.
- [47] A. Einstein, "On the movement of small particles suspended in a stationary liquid demanded by the molecular-kinetic theory of heat," *Annalen der Physik (Leipzig)*, vol. 17, pp. 549–560, 1905.
- [48] E. Guazzelli and L. Oger, *Mobile Particulate Systems*. Springer, 2010.
- [49] D. A. McQuarrie, *Statistical Mechanics*. University Science Books, 2000.
- [50] R. A. L. Jones, *Soft Condensed Matter*. OUP Oxford, 2002.
- [51] L. S. Hirst, *Fundamentals of Soft Matter Science*. CRC Press, 2012.
- [52] G. Perkins and R. Jones, "Hydrodynamic interaction of a spherical particle with a planar boundary I. free surface," *Physica A: Statistical Mechanics and its Applications*, vol. 171, no. 3, pp. 575 – 604, 1991.
- [53] G. Perkins and R. Jones, "Hydrodynamic interaction of a spherical particle with a planar boundary II. hard wall," *Physica A: Statistical Mechanics and its Applications*, vol. 189, no. 3-4, pp. 447 – 477, 1992.
- [54] H. A. Lorentz *Abh. theoret. Phys.*, vol. 1, 1907.
- [55] A. Goldman, R. Cox, and H. Brenner, "Slow viscous motion of a sphere parallel to a plane wall - II Couette flow," *Chemical Engineering Science*, vol. 22, no. 4, pp. 653–660, 1967.
- [56] M. O'Neill, "A sphere in contact with a plane wall in a slow linear shear flow," *Chemical Engineering Science*, vol. 23, no. 11, pp. 1293–1298, 1968.

-
- [57] E. Bart, "The slow unsteady settling of a fluid sphere toward a flat fluid interface," *Chemical Engineering Science*, vol. 23, no. 3, pp. 193–210, 1968.
- [58] G. B. Jeffery *Proceedings of the Royal Society of London. Series A*.
- [59] M. Stimson and G. B. Jeffery, "The motion of two spheres in a viscous fluid," *Proceedings of the Royal Society of London A: Mathematical, Physical and Engineering Sciences*, vol. 111, no. 757, pp. 110–116, 1926.
- [60] L. M. Milne-Thomson, *Theoretical Hydrodynamics*. London: The Macmillan Press Ltd., 5th ed., 1968.
- [61] R. Schmitz and B. Felderhof, "Creeping flow about a spherical particle," *Physica A: Statistical Mechanics and its Applications*, vol. 113, no. 1-2, pp. 90–102, 1982.
- [62] R. Jones and R. Schmitz, "Mobility matrix for arbitrary spherical particles in solution," *Physica A: Statistical Mechanics and its Applications*, vol. 149, no. 3, pp. 373 – 394, 1988.
- [63] D. Bedeaux and P. Mazur, "A generalization of Faxén's theorem to non-steady motion of a sphere through a compressible fluid in arbitrary flow," vol. 78, pp. 505–515, 1974.
- [64] R. G. Cox and H. Brenner, "Effect of finite boundaries on the Stokes resistance of an arbitrary particle Part 3. Translation and rotation," *Journal of Fluid Mechanics*, vol. 28, no. 02, p. 391, 1967.
- [65] R. Cox and H. Brenner, "The rheology of a suspension of particles in a Newtonian fluid," *Chemical Engineering Science*, vol. 26, no. 1, pp. 65–93, 1971.
- [66] B. Felderhof, "Force density induced on a sphere in linear hydrodynamics: I. fixed sphere, stick boundary conditions," *Physica A: Statistical Mechanics and its Applications*, vol. 84, no. 3, pp. 557 – 568, 1976.
- [67] M. Lisicki, "Four approaches to hydrodynamic Green's functions – the Oseen tensors."
- [68] R. Schmitz and B. Felderhof, "Friction matrix for two spherical particles with hydrodynamic interaction," *Physica A: Statistical Mechanics and its Applications*, vol. 113, no. 1-2, pp. 103–116, 1982.

-
- [69] R. Schmitz and B. Felderhof, "Mobility matrix for two spherical particles with hydrodynamic interaction," *Physica A: Statistical Mechanics and its Applications*, vol. 116, no. 1-2, pp. 163–177, 1982.
- [70] B. Cichocki, B. Felderhof, and R. Schmitz, "Hydrodynamic interactions between two spherical particles," *PhysicoChem. Hyd*, vol. 10, no. JANUARY, pp. 383–403, 1988.
- [71] K. K. Sharma, *Optics: Principles and Applications*. Academic Press, 2006.
- [72] M. Born and E. Wolf, *Principles of Optics*. Cambridge University Press, 7th ed., 1999.
- [73] E. Lommel, "Die beugungserscheinungen einer kreisrunden oeffnung und eines kreisrunden schirmchens theoretisch und experimentell," *Abhandlungen der math.-phys. Kl. d. Königl. Bayer. Akad. d. Wiss*, vol. 15, p. 233, 1885.
- [74] E. Wolf, "The diffraction theory of aberrations," *Reports on Progress in Physics*, vol. 14, no. 1, p. 95, 1951.
- [75] S. F. Gibson and F. Lanni, "Diffraction by a circular aperture as a model for three-dimensional optical microscopy," *J. Opt. Soc. Am. A*, vol. 6, no. 9, pp. 1357–1367.
- [76] K. R. Castleman, *Digital Image Processing*. Prentice Hall Professional Technical Reference, 1st ed., 1979.
- [77] S. F. Gibson and F. Lanni, "Experimental test of an analytical model of aberration in an oil-immersion objective lens used in three-dimensional light microscopy," *J. Opt. Soc. Am. A*, vol. 8, no. 10, pp. 1601–1613.
- [78] H. H. Hopkins, "The frequency response of a defocused optical system," *Proceedings of the Royal Society of London A: Mathematical, Physical and Engineering Sciences*, vol. 231, no. 1184, pp. 91–103, 1955.
- [79] P. A. Stokseth, "Properties of a defocused optical system*," *J. Opt. Soc. Am.*, vol. 59, no. 10, pp. 1314–1321.
- [80] H. Kirshner, F. Aguet, D. Sage, and M. Unser, "3-d psf fitting for fluorescence microscopy: implementation and localization application," *Journal of Microscopy*, vol. 249, no. 1, pp. 13–25, 2013.

-
- [81] J. Li, P. Agathoklis, F. Peet, G. Jensen, and T. Sahota, "Measurement and analysis of defocused point spread functions and optical transfer functions of a microscope," in *Communications, Computers, and Signal Processing, 1995. Proceedings., IEEE Pacific Rim Conference on*, pp. 407–410, 1995.
- [82] W. C. K. Poon and D. Andelman, *Soft Condensed Matter Physics in Molecular and Cell Biology*. CRC Press, 2006.
- [83] J. N. Israelachvili, *Intermolecular and Surface Forces*. Academic Press, 2011.
- [84] G. Brotons, T. Salditt, M. Dubois, and T. Zemb, "Highly oriented, charged multilamellar membranes osmotically stressed by a polyelectrolyte of the same sign," *Langmuir*, vol. 19, no. 20, pp. 8235–8244, 2003.
- [85] T. Bickel, "Brownian motion near a liquid-like membrane," *The European Physical Journal E*, vol. 20, no. 4, pp. 379–385, 2006.
- [86] U. Seifert, "Configurations of fluid membranes and vesicles," *Advances in Physics*, vol. 46, no. 1, pp. 13–137, 1997.
- [87] S. Safran, *Statistical thermodynamics on surfaces and interfaces*. Frontiers in Physics, Vol 90, Westview Press, 2003.
- [88] P. Canham, "The minimum energy of bending as a possible explanation of the biconcave shape of the human red blood cell," *Journal of Theoretical Biology*, vol. 26, no. 1, pp. 61 – 81, 1970.
- [89] F. Brochard and J.F. Lennon, "Frequency spectrum of the flicker phenomenon in erythrocytes," *J. Phys. France*, vol. 36, no. 11, pp. 1035–1047, 1975.
- [90] A. Caille, "Remarks on the scattering of x-rays by a-type smectics," *C.R. Seances Acad. Sci., Ser. B*, vol. 274, pp. 891–893, 1972.
- [91] U. Mennicke and T. Salditt, "Preparation of solid-supported lipid bilayers by spin-coating," *Langmuir*, vol. 18, no. 21, pp. 8172–8177, 2002.
- [92] www.olympus.com, *MICROSCOPE COMPONENTS GUIDE: Choosing The Ideal UIS2 Optics Components For Your Equipment*. Olympus Corporation.
- [93] E. Cuevas, D. Zaldívar, and M. Pérez-Cisneros, *Procesamiento digital de imágenes usando MatLAB & Simulink*. Alfaomega, 2010.
- [94] C. Lehmann, *Analytic geometry*. J. Wiley & Sons, inc., 1942.

- [95] N. R. Draper and H. Smith, *Applied Regression Analysis*. John Wiley & Sons, 2014.
- [96] B. Bhushan, K. Koch, and Y. C. Jung, "Fabrication and characterization of the hierarchical structure for superhydrophobicity and self-cleaning," *Ultramicroscopy*, vol. 109, no. 8, pp. 1029 – 1034, 2009. Proceedings of the 10th International Scanning Probe Microscopy Conference.
- [97] B. Haimov, S. Pechook, O. Ternyak, and B. Pokroy, "Shape of water-air interface beneath a drop on a superhydrophobic surface revealed: Constant curvature that approaches zero," *The Journal of Physical Chemistry C*, vol. 117, no. 13, pp. 6658–6663, 2013.
- [98] G. McHale, M. I. Newton, and N. J. Shirtcliffe, "Immersed superhydrophobic surfaces: Gas exchange, slip and drag reduction properties," *Soft Matter*, vol. 6, pp. 714–719, 2010.
- [99] H. Tavana, A. Amirfazli, and A. W. Neumann, "Fabrication of superhydrophobic surfaces of n-hexatriacontane," *Langmuir*, vol. 22, no. 13, pp. 5556–5559, 2006.
- [100] U. Mennicke, D. Constantin, and T. Salditt, "Structure and interaction potentials in solid-supported lipid membranes studied by x-ray reflectivity at varied osmotic pressure," *The European Physical Journal E*, vol. 20, no. 2, pp. 221–230, 2006.
- [101] L.-h. Mei, D.-Q. Lin, Z.-Q. Zhu, and Z.-X. Han, "Densities and Viscosities of Polyethylene Glycol + Salt + Water Systems at 20 °C," *J. Chem. Eng. Data*, vol. 40, no. 6, pp. 1168–1171, 1995.
- [102] K. Arnold, A. Herrmann, L. Pratsch, and K. Gawrisch, "The dielectric properties of aqueous solutions of poly (ethylene glycol) and their influence on membrane structure," *Biochimica et Biophysica Acta*, vol. 815, pp. 515–518, 1985.
- [103] D. Constantin, U. Mennicke, C. Li, and T. Salditt, "Solid-supported lipid multilayers: Structure factor and fluctuations," *The European Physical Journal E*, vol. 12, no. 2, pp. 283–290, 2003.
- [104] H. I. Petrache, S. Tristram-Nagle, K. Gawrisch, D. Harries, V. A. Parsegian, and J. F. Nagle, "Structure and fluctuations of charged phosphatidylserine

bilayers in the absence of salt," *Biophysical Journal*, vol. 86, pp. 1574–1586, 2004.

Thèse de Doctorat

Juan Carlos BENAVIDES PARRA

Mouvement brownien de particules colloïdales situées à proximité de différents types d'interfaces

Brownian motion of colloidal particles located near different types of interfaces

Resumé:

Le mouvement Brownien dans l'eau de colloïdes proches d'interfaces de différente nature (eau/air, eau/verre, ...) est étudié en utilisant une technique de microscopie numérique permettant de reconstruire les trajectoires individuelles en trois dimensions. Des accords satisfaisants entre les trajectoires et les modèles théoriques publiés ont été trouvés pour les cas les plus simples. En outre, nous proposons une approche théorique capable de passer de la configuration d'interface libre (type eau-air) à l'état lié (type liquide-solide). Nous avons également considéré dans ce cadre la situation dans laquelle une interface solide a été fonctionnalisée et rendue hydrophobe pour comparer le mouvement Brownien près de l'interface avec la même interface solide rendue très hydrophile par un traitement au plasma UV-ozone qui crée des groupes hydroxyle (Si-OH). Nous avons également étudié l'interaction colloïdale et hydrodynamique avec des interfaces recouvertes d'une membrane bio-mimétique phospholipidique molle (DOPC en phase fluide) ou gelée (DMPC en phase gel), toutes deux recouvrant le verre (SiO₂).

Mots clés:

Mouvement Brownien; Suivi de particules; Interaction hydrodynamique; Microscopie numérique; Physique statistique; Membrane bio-mimétique.

Abstract:

We explore the Brownian motion of colloids near different types of interfaces (water-air, water-glass,...) using three dimensional digital video microscopy and reconstruction of single colloids trajectories in 3D over time. Satisfying agreements between data and published theoretical models were found for the simplest cases. In addition, we propose a theoretical approach able to transit from the free interface configuration (water-air) to the bound condition (water-glass). We also considered within this frame the situation where a solid interface was functionalized with a grafted short alkyl chain (flat and hydrophobic fixed wall) to compare with the same solid interface made hydrophilic from a UV-ozone plasma treatment that creates hydroxyl groups (Si-OH). From the stabilization of a phospholipid bilayer, we also studied the colloidal and hydrodynamic interactions with a soft (DOPC in L_α phase) or freezed (DMPC at L_β) biomimetic membrane covering the solid interface (SiO₂ glass).

Key words:

Brownian motion; Particle tracking; Hydrodynamic interactions; Digital video microscopy; Statistical physics; Solid supported membranes.